



IntechOpen

Emerging Electric Machines

Advances, Perspectives and Applications

*Edited by Ahmed F. Zobaa
and Shady H.E. Abdel Aleem*



Emerging Electric Machines - Advances, Perspectives and Applications

*Edited by Ahmed F. Zobaa
and Shady H.E. Abdel Aleem*

Published in London, United Kingdom



IntechOpen





Supporting open minds since 2005



Emerging Electric Machines – Advances, Perspectives and Applications

<http://dx.doi.org/10.5772/intechopen.77462>

Edited by Ahmed F. Zobaa and Shady H. E. Abdel Aleem

Assistant to the Editors: Ahmed M. Zobaa

Contributors

Shahin Hedayati Kia, Sergey Gandzha, Dmitriy Gandzha, Vladimir Kodkin, Aleksandr Baldenkov, Aleksandr Anikin, Daniel Matt, Nadhem Boubaker, Susitra Dhanarajalu, Ahmed M. Zobaa, Ahmed F. Zobaa, Shady H. E. Abdel Aleem

© The Editor(s) and the Author(s) 2021

The rights of the editor(s) and the author(s) have been asserted in accordance with the Copyright, Designs and Patents Act 1988. All rights to the book as a whole are reserved by INTECHOPEN LIMITED. The book as a whole (compilation) cannot be reproduced, distributed or used for commercial or non-commercial purposes without INTECHOPEN LIMITED's written permission. Enquiries concerning the use of the book should be directed to INTECHOPEN LIMITED rights and permissions department (permissions@intechopen.com).

Violations are liable to prosecution under the governing Copyright Law.



Individual chapters of this publication are distributed under the terms of the Creative Commons Attribution 3.0 Unported License which permits commercial use, distribution and reproduction of the individual chapters, provided the original author(s) and source publication are appropriately acknowledged. If so indicated, certain images may not be included under the Creative Commons license. In such cases users will need to obtain permission from the license holder to reproduce the material. More details and guidelines concerning content reuse and adaptation can be found at <http://www.intechopen.com/copyright-policy.html>.

Notice

Statements and opinions expressed in the chapters are these of the individual contributors and not necessarily those of the editors or publisher. No responsibility is accepted for the accuracy of information contained in the published chapters. The publisher assumes no responsibility for any damage or injury to persons or property arising out of the use of any materials, instructions, methods or ideas contained in the book.

First published in London, United Kingdom, 2021 by IntechOpen

IntechOpen is the global imprint of INTECHOPEN LIMITED, registered in England and Wales, registration number: 11086078, 5 Princes Gate Court, London, SW7 2QJ, United Kingdom

Printed in Croatia

British Library Cataloguing-in-Publication Data

A catalogue record for this book is available from the British Library

Additional hard and PDF copies can be obtained from orders@intechopen.com

Emerging Electric Machines – Advances, Perspectives and Applications

Edited by Ahmed F. Zobaa and Shady H. E. Abdel Aleem

p. cm.

Print ISBN 978-1-83968-732-7

Online ISBN 978-1-83968-733-4

eBook (PDF) ISBN 978-1-83968-734-1

We are IntechOpen, the world's leading publisher of Open Access books Built by scientists, for scientists

5,300+

Open access books available

130,000+

International authors and editors

155M+

Downloads

156

Countries delivered to

Our authors are among the
Top 1%

most cited scientists

12.2%

Contributors from top 500 universities



WEB OF SCIENCE™

Selection of our books indexed in the Book Citation Index
in Web of Science™ Core Collection (BKCI)

Interested in publishing with us?
Contact book.department@intechopen.com

Numbers displayed above are based on latest data collected.
For more information visit www.intechopen.com



Meet the editors



Ahmed Faheem Zobaa received his BSc (Hons), MSc, and Ph.D. in Electrical Power and Machines from Cairo University, Egypt, in 1992, 1997, and 2002, respectively. He received his Post-graduate Certificate in Academic Practice from the University of Exeter, UK, in 2010, and his DSc from Brunel University London, UK, in 2017. He was an instructor from 1992 to 1997, a teaching assistant from 1997 to 2002, and an assistant Professor from 2002–2007 at Cairo University, Egypt. From 2007 to 2010, he was a senior lecturer in renewable energy at the University of Exeter. From 2010 to 2019, he was a senior lecturer in power systems at Brunel University London, where he is currently a reader in electrical and power engineering. His main areas of expertise include power quality, (marine) renewable energy, smart grids, energy efficiency, and lighting applications. Dr. Zobaa is an executive editor for the International Journal of Renewable Energy Technology, an executive editor-in-chief for Technology and Economics of Smart Grids and Sustainable Energy, and editor-in-chief for the International Journal of Electrical Engineering Education. He is also an editorial board member, editor, associate editor, and editorial advisory board member for many international journals. He is a registered Chartered Engineer, Chartered Energy Engineer, European Engineer, and International Professional Engineer. He is also a registered member of the Engineering Council, UK; the Egypt Syndicate of Engineers; and the Egyptian Society of Engineers. He is a senior fellow of the Higher Education Academy and a fellow of the Institution of Engineering and Technology, Energy Institute, Chartered Institution of Building Services Engineers, Institution of Mechanical Engineers, the Royal Society of Arts, the African Academy of Sciences, and Chartered Institute of Educational Assessors, all in the United Kingdom. He is a senior member of the IEEE, and a member of the International Solar Energy Society, the European Power Electronics and Drives Association, and IEEE Standards Association.



Shady H. E. Abdel Aleem (M'12, SM'21) received a BSc, MSc, and Ph.D. in Electrical Power and Machines from the Faculty of Engineering, Helwan University, Egypt, in 2002, and the Faculty of Engineering, Cairo University, Egypt, in 2010 and 2013, respectively. From September 2018 to September 2019 was an associate professor at the 15th May Higher Institute of Engineering and the quality assurance unit director. Since September 2019, he has been an adjunct associate professor in the Arab Academy for Science, Technology & Maritime Transport, College of Engineering and Technology, Smart Village Campus, where he teaches power quality energy efficiency, wind energy, and energy conversion courses. In addition, he is a consultant in power quality studies at ETA Electric Company, Egypt. His research interests include harmonic problems in power systems, power quality, renewable energy, smart grids, energy efficiency, optimization, green energy, and economics. Dr. Shady is the author or co-author of many refereed journals and conference papers. He has published more than 120 journal and conference papers, eighteen book chapters, and seven edited books with various publishers. He was awarded the State Encouragement Award in Engineering

Sciences in 2017 from Egypt. He was also awarded the medal of distinction from the first class of the Egyptian State Award in 2020. Dr. Shady is a senior member of the Institute of Electrical and Electronics Engineers (IEEE) and the Institution of Engineering and Technology (IET). He is an editor/associate editor for the International Journal of Renewable Energy Technology, Vehicle Dynamics, IET Journal of Engineering, Technology and Economics of Smart Grids and Sustainable Energy, and International Journal of Electrical Engineering Education.

Contents

Preface	XIII
Chapter 1 Introductory Chapter: Emerging Electric Machines - Advances, Perspectives and Applications <i>by Ahmed F. Zobaa, Shady H.E. Abdel Aleem and Ahmed M. Zobaa</i>	1
Chapter 2 Brushless Electric Machines with Axial Magnetic Flux: Analysis and Synthesis <i>by Sergey Gandzha and Dmitry Gandzha</i>	7
Chapter 3 Detection of Stator and Rotor Asymmetries Faults in Wound Rotor Induction Machines: Modeling, Test and Real-Time Implementation <i>by Shahin Hedayati Kia</i>	35
Chapter 4 Prospects for Increasing the Dynamic Efficiency of Asynchronous Double-Feed Machines and Wind Power Generators Using Structural Methods and Solutions <i>by Vladimir L. Kodkin, Alexandr S. Anikin and Alexandr A. Baldenkov</i>	47
Chapter 5 Very Low Voltage and High Efficiency Motorisation for Electric Vehicles <i>by Daniel Matt and Nadhem Boubaker</i>	69
Chapter 6 MNLN and ANFIS Based Inductance Profile Estimation for Switched Reluctance Motor <i>by Susitra Dhanarajalu</i>	89

Preface

Currently, electrical machinery is attracting more attention for the development of competitive energy conversion systems with advanced topologies and innovative drives to realize the increasing advantages of current industrial needs. Modern competitive electrical machines must cope with a broad range of applications such as industrial applications, power generation, renewable energy generation, conversion, and domestic home appliance usage, in addition to the new high-performance embedded applications (electric vehicles, aerospace, aircraft machines, robotics, and others). Performance metrics and key differentiators such as small volume, low-high speed operation, high efficiency and torque, good voltage and flux regulations, robustness, flexibility, long lifetime, controllability, good fault-tolerant operating capability are a need for higher competitive electrical machines in the modern renewable energy era. This book is planned to be essentially an introduction to the concepts and developments of emerging electric machines - advances, perspectives, and applications. The book is organized into six chapters as follows:

Chapter 1 presents an introduction to the book.

Chapter 2 analyzes electric machines with axial magnetic flux and the effect of commutation on the electromagnetic moment and electromagnetic power. The chapter considers two types of discrete switching are considered. The analysis is performed for an arbitrary number of phases. The first type of switching involves disabling one phase for the duration of switching. The second type of switching consists of the operation of all phases in the switching interval. Also investigated is the influence of the pole arc and the number of phases on the electromagnetic moment and electromagnetic power. Finally, a conclusion is made about the advantages of the second type of switching.

Chapter 3 examines the detection of faults in stator and rotor asymmetries in wound-rotor induction machines using rotor and stator currents signatures analysis. This method was proposed for experiments in fault diagnosis in engineering courses on electrical machines. The aim is to demonstrate the main steps of developing real-time condition monitoring for wound-rotor induction machines.

Chapter 4 presents the problems of control of asynchronous machines with dual power supply; as a nonlinear structure, the transfer functions depend on the frequency of the stator voltage and the relative slip. This is especially important for wind turbines that need to remain efficient at different speeds. The chapter presents experiments, modeling, and industrial application of control algorithms with positive torque coupling to justify the theoretical findings.

Chapter 5 presents a new, innovative solid bar winding design for electrical machines (either motors or generators) dedicated to electric propulsion. This new winding technique aims to enhance the performance by utilizing the stator slot, increasing the copper fill factor to greater than 75 percent, and reducing the inactive copper at the end-windings. The suggested winding technique hopes to address these challenges.

Chapter 6 presents computationally efficient modeling techniques for a switched reluctance generator to obtain the nonlinear inductance model through the adaptive neuro-fuzzy inference system (ANFIS) and multivariate nonlinear regression technique (MVNLRT). The chapter also gives a comparative analysis of both models along with inferential remarks.

Ahmed F. Zobaa

College of Engineering,
Design and Physical Sciences,
Brunel University London,
Uxbridge, United Kingdom

Shady H.E. Abdel Aleem

College of Engineering and Technology,
Arab Academy for Science,
Technology and Maritime Transport,
Giza, Egypt

Assistant to the Editors

Ahmed M. Zobaa

Faculty of Engineering,
Cairo University,
Giza, Egypt

Introductory Chapter: Emerging Electric Machines - Advances, Perspectives and Applications

*Ahmed F. Zobaa, Shady H.E. Abdel Aleem
and Ahmed M. Zobaa*

1. Introduction

With increasing attention on modern energy conversion (EC) systems, electrical machinery (EM) has been given more and more attention to developing new topologies and innovative drives to realize the increasing advantages of current industrial needs. Direct current (DC) machines, induction machines (IMs), and synchronous machines (SMs) were conventional most commonly used EMs in the industry in the past. Still, IMs, mainly the squirrel-cage IM (SCIM) types, are the most widely used EMs because they provide many advantages like effortless simple control, easy but efficient repair, high efficiency, and low cost and sizes [1].

EMs' energy consumption in the industry is 40% plus of the total generated energy worldwide [2]; thus, improving the machines' design and efficiency, even the conventional types, can considerably save energy. However, new EMs and their drives are industrialized with many extra features to meet the recent application areas, for example, electric vehicles (EVs), electric ships (ESs), aircraft machines, robotics, wind power generation, automated propulsion systems, and others [3].

These machines have to cope with numerous new applications under uncertain operating conditions, e.g. fixed or variable speed, uncertain loads (fixed or variable loads), and alteration of the supply voltage (whether constant or variable supply) [1].

2. Emerging Electric Machines

Several factors affect EC systems' efficiency, motor-system efficiency, and the system's performance (from the perspective of power quality (PQ), energy efficiency, or reliability). For instance, all stakeholders should pay much attention to harmonic distortion problems associated with the variable frequency drives (VFDs), power electronic-based equipment, and nonlinear loads [4], oversizing of equipment distribution losses and power factor of the motors [5], variation of the loading conditions and load management practice (matching between motors and loads at any loading level), maintenance practices (for electrical, electronic and mechanical parts alike, and transmission system issues [6].

Despite the importance of these critical factors, they are often disregarded in practice. Considering these factors can significantly improve efficiency and enhance the motor systems' power quality and reliability performance.

In [3], the conventional brushed-type EMs is categorized as:

- i. Series or shunt self-excited DC machines,
- ii. Separately-excited DC (field or permanent-magnet (PM)), and
- iii. Synchronous or induction (wound-rotor and double-fed types).

Also, the brushless EMs can be categorized as:

- i. Synchronous (wound-rotor type),
- ii. Induction (squirrel-cage type),
- iii. Brushless PM, and
- iv. Advanced magnetless machines.

The traditional brushless PM can have more than one machine – surface (SPM), inserted, and double-salient, so-called IPM, and DCPM, respectively. However, there are a lot of new PM machines, which have different flux distribution than the traditional brushless PM machines [3], such as hybrid-excited, memory, vernier, double-stator, double-rotor, magnetic-gear, linear, axial, and transverse PM machines.

The advanced magnetless machines can also have many types associated with the DC field excitation, such as the switched reluctance (SR), vernier reluctance (VR), and flux switching and reversal machines.

Figure 1 illustrates the various control strategies for EMs [7]. The control strategies can be applied with both types of machines (traditional and emerging machines). Besides, they can be adopted to be suitable for both types. The control strategies include:

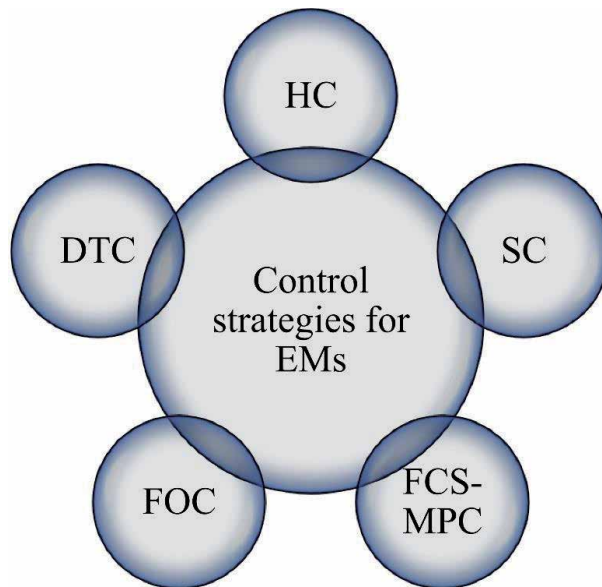


Figure 1.
Control strategies for EMs.

- i. Model predictive control associated with the finite-control set (FCS-MPC),
- ii. Control using field-orientation (FOC),
- iii. Direct torque-based control (DTC),
- iv. Sensorless-based control (SC), and
- v. Hybrid control techniques (HC).

The corresponding merits that these emerging EMs can fulfill with these various control strategies are shown in **Figure 2** [3, 8]. These merits allow them to efficiently and effectively operate with different emerging applications such as robotics and EVs.

From the application point of view, conventional EMs are usually dedicated to industrial applications, power generation, renewable energy generation, conversion, and domestic home appliances usage. However, emerging EMs are by default dedicated to new high-performance, innovative applications and intelligent devices besides their potential to be used in conventional applications. This is because of the weakness issues of traditional EMs, such as their need for regularly scheduled maintenance, complicated control and narrow speed range (particularly in alternating current (AC) machines), the complexity of operation and management in high-speed operation, low efficiency, and low capability to be overloaded.

On the other side, the emerging EMs also have some weakness issues because of their exceptional design and necessary control. The difficulty of manufacture and the high cost are examples of these demerits.

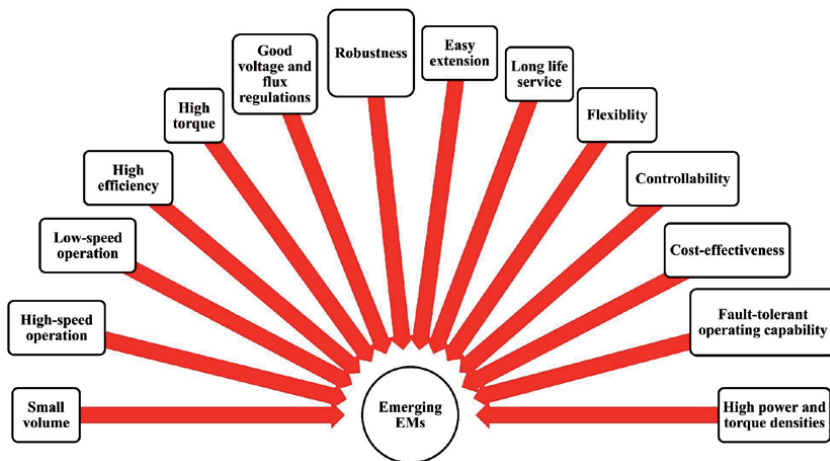


Figure 2.
Features and merits of emerging EMs.

Abbreviations

AC	Alternating current
DC	Direct current
DCPM	Double-salient PM

DTC	Direct torque-based control
EC	Energy conversion
EM	Electrical machinery
ESs	Electric ships
EVs	Electric vehicles
FCS-MPC	Finite-control set model predictive control
FOC	Field-orientation-based control
IMs	Induction machines
IPM	Inserted PM
HC	Hybrid control
PM	Permanent-magnet
PQ	Power quality
SC	Sensorless-based control
SCIM	Squirrel-cage IM
SG	Synchronous generator
SMs	Synchronous machines
SPM	Surface PM
SR	Switched reluctance
VFDs	Variable frequency drives
VR	Vernier reluctance

Author details

Ahmed F. Zobaa^{1*}, Shady H.E. Abdel Aleem^{2,3} and Ahmed M. Zobaa⁴

1 College of Engineering, Design and Physical Sciences, Brunel University London, Uxbridge, United Kingdom


2 Technology and Maritime Transport, Electrical Energy Department, College of Engineering and Technology, Arab Academy for Science, Smart Village Campus, Giza, Egypt

3 Power Quality Solutions Department, ETA Electric Company, El Omraniya, Giza, Egypt

4 Electrical Power Department, Cairo University, Giza, Egypt

*Address all correspondence to: azobaa@ieee.org

IntechOpen

© 2021 The Author(s). Licensee IntechOpen. This chapter is distributed under the terms of the Creative Commons Attribution License (<http://creativecommons.org/licenses/by/3.0>), which permits unrestricted use, distribution, and reproduction in any medium, provided the original work is properly cited. 

References

- [1] M. Ćalasan, M. Micev, Z. M. Ali, A. F. Zobaa, and S. H. E. A. Aleem, "Parameter estimation of induction machine single-cage and double-cage models using a hybrid simulated annealing-evaporation rate water cycle algorithm," in *Mathematics*, vol. 8, no. 6, Elsevier, 2020, pp. 185-217.
- [2] R. D. Cepoi, F. F. Jaşcău, and L. Szabó, "Current trends in energy efficient electrical machines," *J. Electr. Electron. Eng.*, vol. 10, no. 2, pp. 13-18, 2017.
- [3] C. Liu, "Emerging electric machines and drives - An overview," *IEEE Trans. Energy Convers.*, vol. 33, no. 4, pp. 2270-2280, 2018, doi: 10.1109/TEC.2018.2852732.
- [4] S. H. E. A. Aleem, A. F. Zobaa, M. E. Balci, and S. M. Ismael, "Harmonic overloading minimization of frequency-dependent components in harmonics polluted distribution systems using harris hawks optimization algorithm," *IEEE Access*, vol. 9, pp. 100824-100837, 2019, doi: 10.1109/ACCESS.2019.2930831.
- [5] M. Khodapanah, A. F. Zobaa, and M. Abbod, "Estimating power factor of induction motors at any loading conditions using support vector regression (SVR)," *Electr. Eng.*, vol. 100, no. 4, pp. 2579-2588, 2018.
- [6] A. De Almeida, P. Bertoldi, and W. Leonhard, *Energy efficiency improvements in electric motors and drives*. Springer Science & Business Media, 2012.
- [7] A. H. Abosh, Z. Q. Zhu, and Y. Ren, "Reduction of torque and flux ripples in space vector modulation-based direct torque control of asymmetric permanent magnet synchronous machine," *IEEE Trans. Power Electron.*, vol. 32, no. 4, pp. 2976-2986, 2017, doi: 10.1109/TPEL.2016.2581026.
- [8] K. T. Chau, C. C. Chan, and C. Liu, "Overview of permanent-magnet brushless drives for electric and hybrid electric vehicles," *IEEE Trans. Ind. Electron.*, vol. 55, no. 6, pp. 2246-2257, 2008, doi: 10.1109/TIE.2008.918403.

Brushless Electric Machines with Axial Magnetic Flux: Analysis and Synthesis

Sergey Gandzha and Dmitry Gandzha

Abstract

An analysis of electric machines with axial magnetic flux is given. First, the effect of commutation on the electromagnetic moment and electromagnetic power is analyzed. Two types of discrete switching are considered. The analysis is performed for an arbitrary number of phases. The first type of switching involves disabling one phase for the duration of switching. The second type of switching involves the operation of all phases in the switching interval. The influence of the pole arc and the number of phases on the electromagnetic moment and electromagnetic power is investigated. The conclusion is made about the advantage of the second type of switching. It is recommended to increase the number of phases. Next, the classification of the main structures of the axial machine is carried out. Four main versions are defined. For each variant, the equation of the electromagnetic moment and electromagnetic power is derived. This takes into account the type of commutation. The efficiency of the selected structures is analyzed. The comparative analysis is tabulated for choosing the best option. The table is convenient for engineering practice. This chapter forms the basis for computer-aided design of this class of machines.

Keywords: brushless electric machine, axial gap electric machine, discrete commutation, multiphase electric machine, electromagnetic moment, electromagnetic power, permanent magnet, cylindrical magnet, segment magnet, diamagnetic anchor

1. Introduction

Low- and medium-power electric drives based on brushless electric machines are widely used both in industrial applications and in special-purpose products (space, medicine, robotics). Traditionally, brushless electric machines with a radial magnetic flux are used for this purpose. This is due to the good specific energy indicators of these electric machines, well-established technology of their production [1–7].

Recently, brushless electric machines with axial magnetic flux (BMAMF) have been increasingly used for these purposes. These electric machines are actively developing, and we can talk about the formation of a new class of brushless electric drives that are competitive with traditional brushless electric drives. There is a process of transition from the design of individual products to the development of an industrial range of electric machines of this type. International and domestic practice confirms this trend [8–12].

The following reasons can explain the active introduction of electric machines of this class into production:

- at present, the industrial production of powerful magnets with high values of residual induction and coercive force has been intensively developed, which allowed to concentrate the energy of the magnetic field in small volumes and reduce the size of electric machines;
- modern development of computing tools and special software allows you to optimize the geometry of BMAMF for efficient use of the volume occupied by them. At the same time, optimally designed BMAMF under conditions of limited size can have better specific weight size and energy indicators compared to radial electric machines;
- modern technologies allow to create BMAMF more economical to manufacture and reliable in operation.

It should be noted that, despite the urgent need for practical implementation, theoretical research on the analysis and synthesis of electric machines of this class is episodic and scattered. As a rule, developers analyze one design for a special drive. The results of these studies are quite difficult to transform into another constructive type. The influence of the electronic switch on the engine characteristics has not been fully studied.

Recently, there has been a tendency to increase the number of phases to improve reliability [13]. At the same time, the switching theory for multiphase BMAMF execution is not sufficiently covered in scientific publications and requires further improvement and development.

There is no unified theory for calculating electric machines of this class that would link electromagnetic power with electromagnetic loads and basic dimensions, taking into account design features.

Thus, the existing contradiction between the practical need for implementation and the insufficiently developed theory of analysis and synthesis is the main source of further development of electric machines of this class, which determines the relevance of scientific research in this area.

2. Analysis of the effect of commutation on the electromagnetic moment for any number of phases of the anchor winding for BMAMF

The winding of the brushless electric machine is connected to the power source via a commutator. Its principle of operation is as follows: when the rotor is turned, those sections of the armature winding are connected to the source, which are most profitable to pass current through from the point of view of creating an electromagnetic moment.

Switching the valve machine should be understood as connecting and disconnecting the phases of the armature winding with electronic keys to the power source. The main characteristics of the electric machine depend on the choice of switching method: moment, power consumption and useful power, efficiency, current.

The classification of the main types of switching of brushless machines is shown in **Figure 1**. Analog switching implements vector control of the brushless machine. Vector control is a control method that generates harmonic phase currents and controls the magnetic flux of the rotor. Currently, vector control systems are well developed in theory and implemented in practice. They have a wide range of applications, due to the development of power electronics, which allows you to create reliable and relatively cheap converters, as well as the development of high-speed

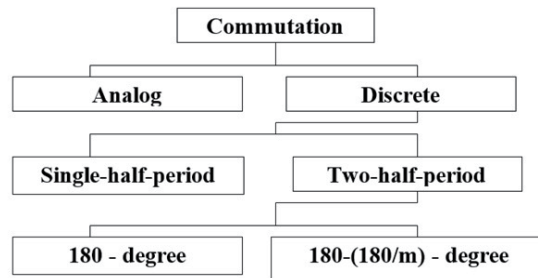


Figure 1.
The classification of the main types of switching of BMAMF.

microelectronics that can implement control algorithms of almost any complexity. However, it is necessary to recognize the great complexity of implementing this type of switching. For this reason, it is not considered in the work.

In contrast to analog switching, in discrete switching, electronic keys on the inter-switching interval have only two States: on and off. Discrete switching by the nature of the current is divided into one-half-period switching, when the current in the phase sections flows in only one direction, and two-half-period switching, when the current flows in both directions.

Single-half-period switching is simple enough to implement, since it requires only one key per switched phase. However, the armature phase is connected to the source only in the zone of polarizing which creates a positive electromagnetic moment. After that, the phase is in the disconnected state without generating electromagnetic torque. To maintain the required torque, it is necessary to increase the linear load on the connected phases, which leads to increased losses and reduced efficiency. Due to the worst energy performance, Single-half-period switching is also excluded from further analysis.

Types of two-half-period switching are distinguished by the time the phase is connected in the inter-switching interval. A distinction should be made between 180-degree switching and 180-(180/m) degree switching.

In the future, we will consider 180-degree switching and 180-(180/m)-degree switching.

At present, there is a steady trend towards an increase in the number of phases of the anchor winding. This is due to the following factors:

- improved energy performance, in particular efficiency;
- indicators that characterize the quality of output parameters are improved, in particular, the pulsation of the electromagnetic moment is reduced;
- increased reliability in case of failures of one or more phases.

Increased reliability is a determining factor when the number of phases increases.

According to the method of connecting multiphase windings to each other, three options are possible: in the “star”, in the “ring”, with independent connection (galvanically isolated phases).

If the number of phases is more than three, when connected to a “star”, the current flows only through the phases that have the highest and lowest potential on the switched keys. This reduces the power of the multiphase BMAMF.

The connection of the winding to the ring is rarely used due to the increased current through the keys. When connecting in a “star” and “ring”, it is difficult to ensure high reliability in case of phase failures.

Galvanically isolated phases require a large number of power keys (four keys per phase), but they provide the greatest reliability in case of open and short circuit

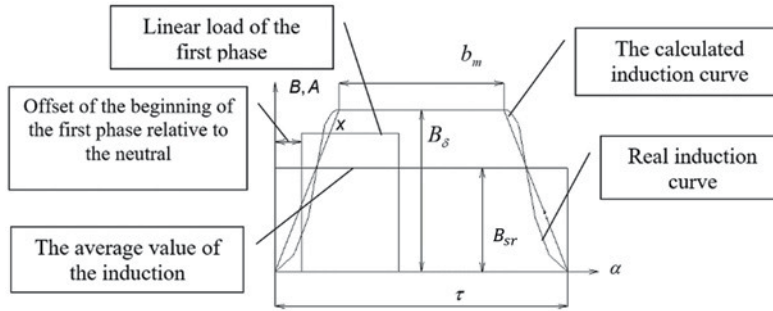


Figure 2.
Representation of air gap induction and linear load.

failures. Taking into account the development trends of power electronics for the production of hybrid assemblies, we choose to focus on the study of this type of connection of multiphase BMAMF windings.

Thus, two-half-period (180-(180/m)-degree switching and two-half-period 180-degree switching with galvanically isolated phases are selected for further analysis.

For the selected switching types, we will carry out the further analysis.

2.1 Analysis of 180-(180/m) - degree commutation for BMAMF with any phases

To analyze the commutation, we determine the interaction of amperes-turns with the magnetic field of permanent magnets at different positions of the armature and inductor relative to each other. In this case, a trapezoidal one with an equivalent amplitude replaces the actual distribution of induction in the air gap [13].

By the pole overlap coefficient, we mean the ratio:

$$\alpha = \frac{b_m}{\tau}, \quad (1)$$

where b_m - width of the pole;

τ - distance between of the neutrals.

The linear load of the phase conductors is represented as rectangles, equal in width to the phase zone, and equal in amplitude to the average linear load of the phase (Figure. 2). The analysis is carried out for relative values, taking the base value of the induction amplitude and the average linear load on the average diameter of the axial machine. This representation of an electric machine for analysis should be recognized as traditional.

Figure 3 shows a diagram of the positions of the amperes of the turns in the inter-switching interval for the two pole divisions and the moments of connection and disconnection of the corresponding phases.

We derive the equation of the electromagnetic moment for a generalized axial machine, which is a disk with a distributed current layer that is permeated by a magnetic flux (Figure 4).

The equation of an elementary electromagnetic force acting on an infinitesimal section of a generalized axial machine can be written in the following form based on Ampere's law.

$$dF = B d i d r \quad (2)$$

where B – elementary section induction;

di – elementary section current;
 dr – length of an elementary section.

For an elementary moment, we can write the equation

$$dM = r dF = Br di dr, \quad (3)$$

where r – radius of the elementary section location.

Imagine the induction as the product of a base value equal to the amplitude of the induction in the air gap and the relative function of the change in the induction within the pole division.

$$B = B_\delta B(\alpha_{el}), \quad (4)$$

where α_{el} – angular coordinate in electrical degrees.

By analogy with induction, we express the linear load function on the average radius of the disk of a generalized axial machine depending on the pole division

$$A(x) = A_{sr} A_i(\alpha_{el}, x), \quad (5)$$

where A_{sr} – the amplitude of the linear load on the average radius of the disk.

$A_i(\alpha_{el}, x)$ – relative function of the linear load change for the i -th phase within the pole division in electrical degrees;

x – offset of the beginning of the first phase relative to the neutral.

Given that there is a relationship between geometric and electrical degrees

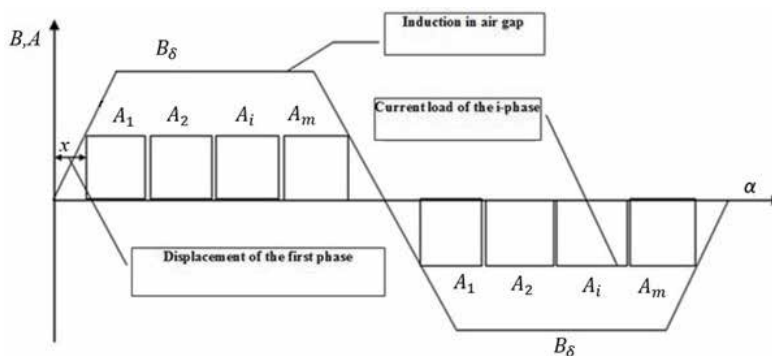


Figure 3.
 The diagram for the $(180-180/m)$ -degree commutation.

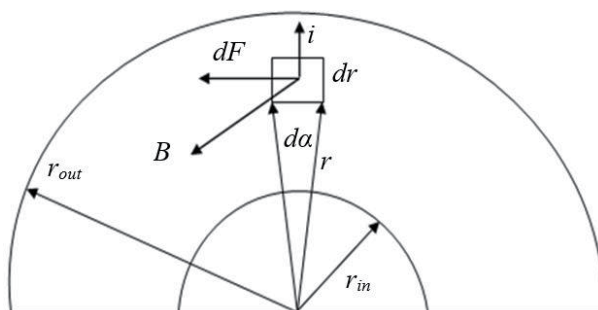


Figure 4.
 Model for axial gap machine.

$$\alpha = 2p\alpha_{el}, \quad (6)$$

where $2p$ – the number of poles of a generalized axial machine.

The expression for the current of an elementary section can be written as follows

$$di(x) = \frac{2\pi r_{sr} A_{sr} A_i(\alpha_{el}, x)}{2\pi r} r 2pd\alpha_{el} = 2pr_{sr} A_{sr} A_i(\alpha_{el}, x) d\alpha_{el}, \quad (7)$$

Substituting (Eq.4) and (Eq.4) in (Eq.3), we obtain an expression for the electromagnetic moment of the elementary section that creates the i-th phase

$$dM_{fi}(x) = 2pr_{sr} A_{sr} B_{\delta} B(\alpha_{el}) A_i(\alpha_{el}, x) r dr d\alpha_{el}. \quad (8)$$

To determine the moment of the i-th phase, we take the integral over the disk surface of a generalized axial machine

$$\begin{aligned} M_{fi}(x) &= \int_{r_{in}}^{r_{out}} \int_0^{2\pi} dM_{fi}(x) = 2pr_{sr} A_{sr} B_{\delta} \int_{r_{in}}^{r_{out}} \int_0^{2\pi} B(\alpha_{el}) A_i(\alpha_{el}) r dr d\alpha_{el} \\ &= \frac{p}{2} A_{sr} B_{\delta} D_{sr}^2 L_{ring} \int_0^{\pi_{el}} B(\alpha_{el}) A_i(\alpha_{el}) d\alpha_{el}, \end{aligned} \quad (9)$$

where D_{sr} – average ring diameter of a generalized axial machine, L_{ring} – ring thickness of the generalized axial machine (**Figure 4**).

For the basic moment value, we take the expression

$$M_b = \frac{p}{2} A_{sr} B_{\delta} D_{sr}^2 L_{ring}. \quad (10)$$

Then the dependence of the relative moment on the displacement of the armature relative to the inductor for the i-th phase will have the form.

$$M_{fi}^* = \int_0^{\pi_{el}} B(\alpha_{el}) A_i(\alpha_{el}, x) d\alpha_{el} \quad (11)$$

Decompose the function of induction and linear load into a harmonic series. We take into account the symmetry of the curves relative to the coordinate axes.

Relative value of induction in the air gap

$$B(\alpha_{el}) = \sum_{n=1}^k a_n \sin(n\alpha_{el}); \quad (12)$$

$$a_n = \frac{2}{\pi_{el}} \left(\int_0^{\frac{\pi_{el}(1-\alpha)}{2}} \frac{2\alpha}{\pi_{el}(1-\alpha)} \sin(n\alpha_{el}) d\alpha_{el} + \int_{\frac{\pi_{el}(1-\alpha)}{2}}^{\frac{\pi_{el}(1-\alpha)}{2} + \pi\alpha} \sin(n\alpha_{el}) d\alpha_{el} + \int_0^{\frac{\pi_{el}(1-\alpha)}{2} + \pi\alpha} \frac{2(1-\alpha)}{\pi_{el}(1-\alpha)} \sin(n\alpha_{el}) d\alpha_{el}, \right) \quad (13)$$

where k – number of terms in the harmonic series.

Relative value of the linear load of the i-th phase:

$$A_i(\alpha_{el}, x) = \sum_{n1}^{k1} a_{1n1}(i, x) \sin(n1\alpha_{el}) + b_{1n1}(i, x) \cos(n1\alpha_{el}); \quad (14)$$

$$a_{1n_1}(i, x) = \frac{1}{\pi_{el}} \left(\int_{-\pi_{el} + (i-1)\frac{\pi_{el}}{m} + x}^{-\pi_{el} + i\frac{\pi_{el}}{m} + x} (-1) \sin(n_1 \alpha_{el}) d\alpha_{el} + \int_{(i-1)\frac{\pi_{el}}{m} + x}^{i\frac{\pi_{el}}{m} + x} \sin(n_1 \alpha_{el}) d\alpha_{el} \right); \quad (15)$$

$$b_{1n_1}(i, x) = \frac{1}{\pi_{el}} \left(\int_{-\pi_{el} + (i-1)\frac{\pi_{el}}{m} + x}^{-\pi_{el} + i\frac{\pi_{el}}{m} + x} (-1) \cos(n_1 \alpha_{el}) d\alpha_{el} + \int_{(i-1)\frac{\pi_{el}}{m} + x}^{i\frac{\pi_{el}}{m} + x} \cos(n_1 \alpha_{el}) d\alpha_{el} \right), \quad (16)$$

where k_1 – number of terms in the harmonic series;

i – the number of the phase; m – number of phases.

The total torque of the anchor winding will be created as a sum of the phases torques (one phase is switched of)

$$M_{180-\frac{180}{m}}^*(x) = \sum_{i=1}^{m-1} M_{f_i}^*(x). \quad (17)$$

The medium torque for this type of commutation may be described by the following formula

$$M_{sr(180-180/m)}^* = \frac{\int_0^{\frac{\pi_{el}}{m}} M_{180-180/m}^*(x) dx}{\frac{\pi_{el}}{m}}. \quad (18)$$

It is possible to see from diagram 3 that different wires conductors create different torque because they take place in different magnet field conditions. The factor below can estimate the efficiency of anchor wire:

$$K_{ef(180-\frac{180}{m})}(\alpha, m) = \frac{M_{sr(180-180/m)}^*}{\pi_{el}}. \quad (19)$$

Let us name this factor as the efficiency factor of the anchor for $(180-180/m)$ -degree commutation, This factor depends from pole factor and number of the phases. The curves for $(180-180/m)$ -degree commutation (Eq. 19)) are presented in **Figure 5**. The curves analysis shows that it is necessary to increase pole factor and number of the phases for increasing the electromagnetic torque.

The absolute moment may be defined by the following formula

$$M_{sr(180-180/m)} = \frac{\pi}{2} A_{sr} B_{\delta} D_{sr}^2 L_{ring} K_{ef(180-\frac{180}{m})}. \quad (20)$$

The curves analysis shows that it is necessary to increase pole factor and number of the phases for increasing the electromagnetic torque.

2.2 Analysis of 180-degree commutation for BMAMF with any phases

We will use the same harmonic analysis method for 180-degree commutation.

The diagram of the 180-degree commutation is presented in **Figure 6**.

We may use the same formulas (Eq. (9), Eq. (12), Eq. (14)) for induction in the air gap, current load, and torque for the one phase.

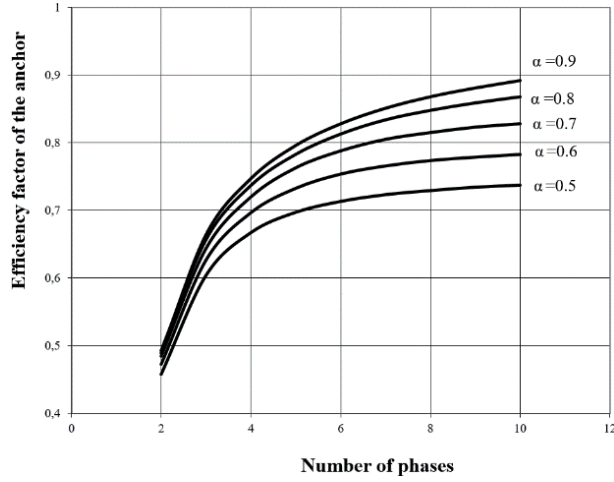


Figure 5. The dependences of the efficiency factor of the anchor wire for $(180-180/m)$ -degree commutation from pole factor and number of phases.

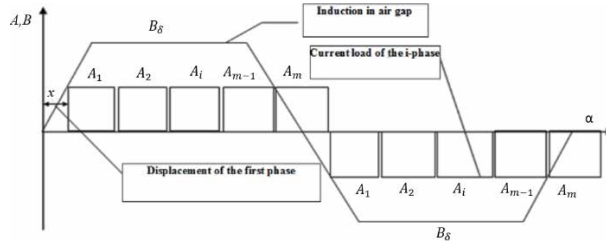


Figure 6. The diagram for the 180-degree commutation.

For the total relative torque, we may write the following formula (all phases are switched on).

$$M_{180}^*(x) = \sum_{i=1}^m M_{fi}^*(x). \quad (21)$$

The medium torque

$$M_{sr180}^* = \frac{\int_{-\frac{\pi_{el}}{2m}}^{\frac{\pi_{el}}{2m}} M_{180}^*(x) dx}{\frac{\pi_{el}}{m}}. \quad (22)$$

The efficiency factor of the anchor for 180-degree commutation

$$K_{ef180}(\alpha, m) = \frac{M_{sr180}^*}{\pi_{el}}. \quad (23)$$

The curves for this factor (Eq.(23)) are presented in the **Figure 7**. The absolute moment may be defined by the following formula

$$M_{sr180} = \frac{\pi}{2} A_{sr} B_{\delta} D_{sr}^2 L_{ring} K_{ef180}. \quad (24)$$

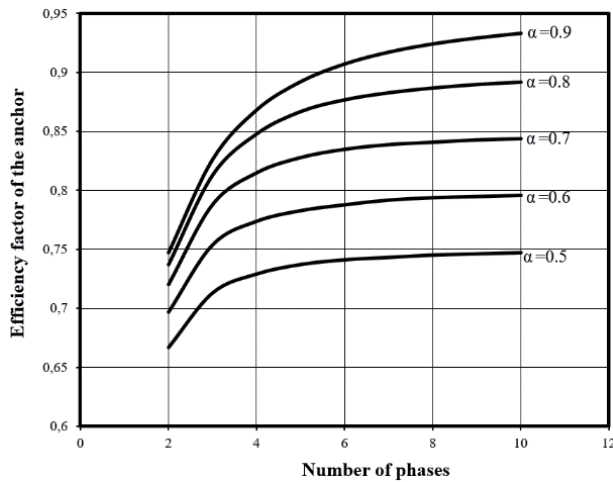


Figure 7.
 The dependences of the efficiency factor of the anchor for 180-degree commutation from pole factor and number of phases.

We can create the same conclusion for this type of the commutation. It is necessary to increase the pole factor and number of the phases for increasing the electromagnetic torque.

Let us compare the efficiency of this type commutation. The electromagnetic torque will be the criteria for this analysis.

2.3 The compare of the (180–180/m)-degree commutation and 180- degree commutation for BMAMF with any phases

We will use the same sizes and the same current load for both types of commutation.

The ratio of the total electromagnetic torques is

$$\frac{M_{sr180}}{M_{sr(180-180/m)}} = \frac{K_{ef180}}{K_{ef(180-\frac{180}{m})}}. \quad (25)$$

Let us compare both commutations for pole factor 0.8. It is typical pole factor for brushless machine. The curve of this analysis is shown in the **Figure 8**.

The curve shows that 180-degree commutation has the advantage but for big numbers of phases this advantage is decreasing. It is possible to do this compare for another type of the pole factors and we will have the same conclusion.

We show the advantage of the 180-degree commutation with using the electromagnetic torque.

The studies have shown that to increase the efficiency of the system it is necessary to increase the number of phases and use the 180-degree commutation but it is necessary to say that the cost of electronic control system will be increasing with increasing the number of phases. Therefore, the researcher has to take a mind this information when he will create the real equipment.

It should be noted that as the number of phases increase, the difference in efficiency of these type of commutation decreases too. Since the (180–180/m)-degree commutation is simpler to implement, so it can be chosen for practice.

The study can define the following results:

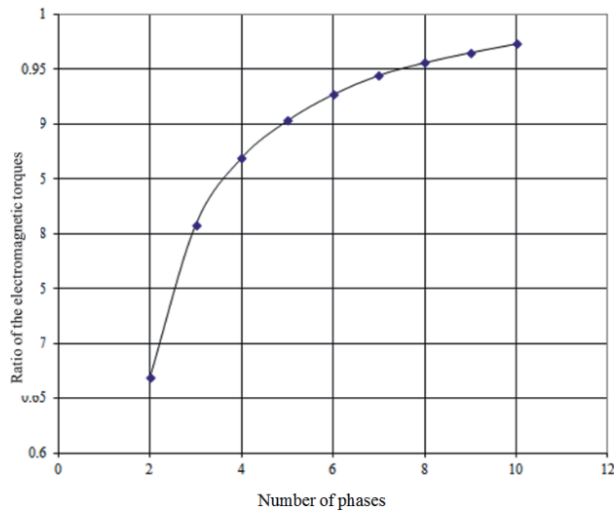


Figure 8.

The compare of the $(180-180/m)$ -degree commutation with the 180 -degree commutation for pole factor 0.8 .

1. The electromagnetic torque will be increasing for both type commutations with increasing the number of phases.
2. 180 -degree commutation has the advantage with different phases and different pole factors if compare it with the $(180-180/m)$ -degree commutation.

These conclusions determine the trend of increasing efficiency, but in practice, it is necessary to calculate the price for choosing the best type of commutation.

3. Analysis of electromagnetic power of various designs of the BMAMF

BMAMF have a large number of designs. Different designs in the same dimensions develop different torque and power. To compare the effectiveness of various designs, we will classify them.

3.1 Classification of various BMAMF designs

The shape of active elements that create an electromagnetic moment can classify a large number of design modifications of BMAMF. The shape of permanent magnets may be cylindrical, prismatic and segmental magnets. BMAMF phase coils can have ring, trapezoidal, wave, and toroid shapes. The combination of various permanent magnet shapes with armature winding shapes creates a variety of BMAMF designs [14, 15]. The classification of BMAMF structures is shown in **Figure 9**.

The main design versions of BMAMF active parts with various forms of magnets and coils are shown below. On their basis, it is possible to build various design modifications. Let us call these models basic. **Figure 10** shows a BMAMF with cylindrical magnets and ring coils. **Figure 11** shows a BMAMF with segment magnets and trapezoidal coils. **Figure 12** shows a BMAMF with segment magnets and toroid coils.

The development of computational models for the above structures has its own peculiarities. Let us output the values of the electromagnetic moment and electromagnetic power for the basic versions shown in **Figure 10–13**.

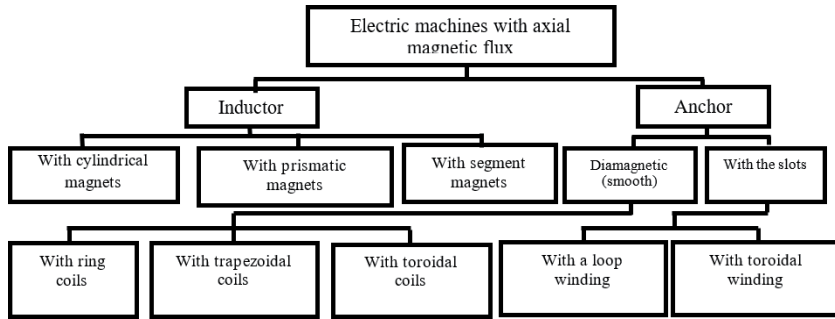


Figure 9.
Classification of BMAMF.

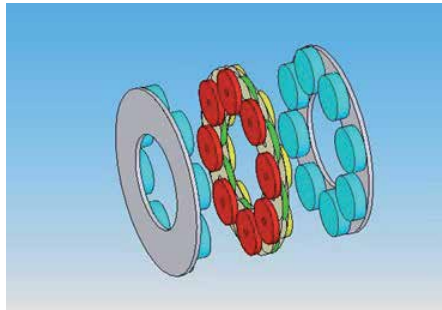


Figure 10.
BMAMF with cylindrical magnets and a smooth anchor with ring coils.

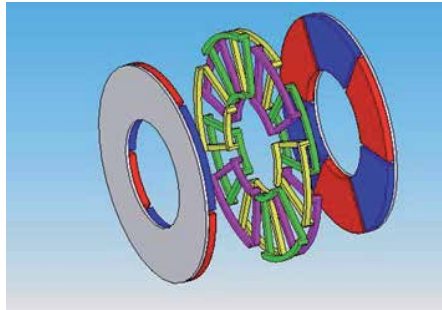


Figure 11.
BMAMF with segment magnets and a smooth anchor with trapezoidal.

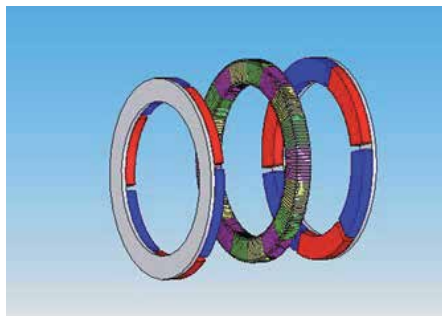


Figure 12.
BMAMF with segment magnets and a smooth armature with toroidal coils.

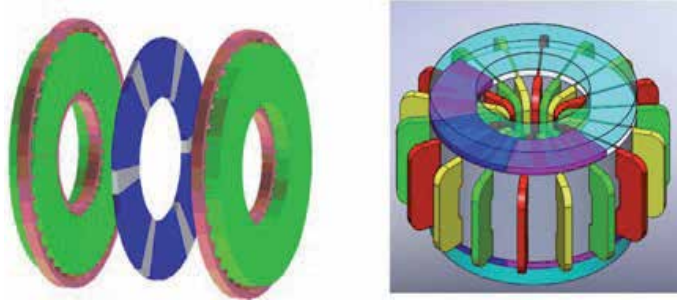


Figure 13.
BMAMF with segment magnets and toothed anchor.

3.2 Electromagnetic torque and electromagnetic power for BMAMF with cylindrical magnets and smooth armature with ring coils

Let us define the electromagnetic moment of the phase in the position at which it has the maximum value. This is the position at which the axis of the ring coil coincides with the geometric neutral. A sketch of the magnetic system and the armature winding is shown in **Figure 14**. To facilitate reference to the dependencies given below, we denote this design as model 1.

The real value of the magnetic induction in the gap is replaced by its average value, assuming that it does not change within the pole division.

The ratio between the maximum induction and the average induction is determined by the formula

$$B_{sr} = B_{\delta} \frac{S_{pole}}{S_{\tau}}, \quad (26)$$

where S_{pole} – surface of the pole,
 S_{τ} – area of the pole division/.

Let us choose an arbitrary j turn with an anchor current i_a . On this turn, we select an elementary conductor with length dl on the left and right sides. These elementary conductors will be affected by elementary forces, like conductors in a magnetic field, which will be directed to the center of the anchor coil. These forces can be decomposed into components on the X-axis and on the y-axis. The forces on the Y-axis will compensate for each other as equal in magnitude and opposite in direction.

The electromagnetic moment will only be created by forces directed along the x-axis. Elementary moment of the j -th turn:

$$dM_j = dM_{\alpha 1j} + dM_{\alpha 2j}, \quad (27)$$

where

$$dM_{\alpha 1j} = dF_{\alpha 1xj} (R_{sr} + r_{vj} \sin \alpha_1) = i_a B_{sr} r_{vj} \cos \alpha_1 (R_{sr} + r_{vj} \sin \alpha_1) d\alpha_1. \quad (28)$$

$$dM_{\alpha 2j} = dF_{\alpha 2xj} (R_{sr} + r_{vj} \sin \alpha_1) = i_a B_{sr} r_{vj} \cos \alpha_2 (R_{sr} + r_{vj} \sin \alpha_2) d\alpha_2. \quad (29)$$

where $dF_{\alpha 1xj}, dF_{\alpha 2xj}$ – elementary forces acting on the left and right halves of the coil;

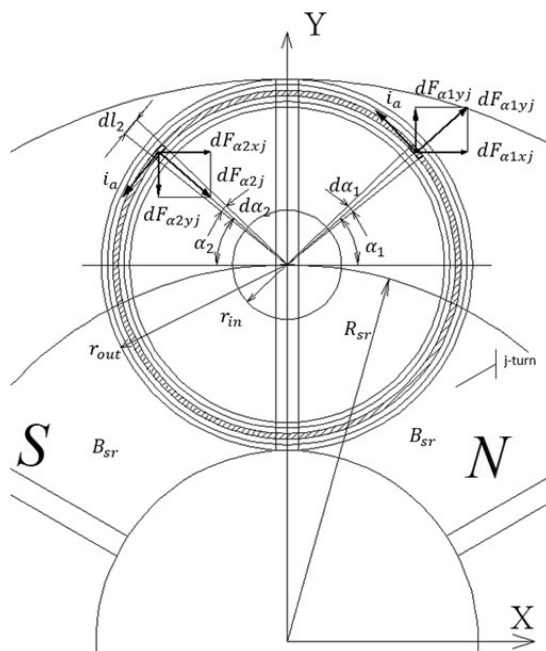


Figure 14. Sketch of the magnetic system and armature windings BMAMF with ring armature windings.

R_{sr} – average radius of the magnetic system ring;

r_{vj} – radius of the j -th turn.

Moment of the j -th turn

$$M_j = \int_0^{2\pi} (dM_{\alpha 1j} + dM_{\alpha 2j}) = i_a B_{sr} D_{sr} d_{vj}, \quad (30)$$

where D_{sr} – average ring diameter of the magnetic system;

d_{vj} – diameter of the j -th turn.

The maximum moment of phase

$$M_{maxfmod1} = p \sum_{j=1}^{W_s} M_j = i_a B_{sr} D_{sr} d_{r sr} p W_s, \quad (31)$$

where W_s – number of turns in the coil section;

$d_{r sr}$ – the average diameter of the coil section ring.

Let us express the average ring diameter of the coil section in terms of the ring thickness of the magnetic system.

From the angle of rotation, the moment of the phase changes according to the law of cosine

$$M_{fmod1}(\gamma_{el}) = M_{maxfmod1} \cos(\gamma_{el}), \quad (32)$$

where γ_{el} – turn of the armature relative to the inductor in electrical degrees.

Let us determine the maximum electromagnetic moment of the machine for various switching options.

For (180–180/m)-degree commutation

$$\begin{aligned}
 M_{max\ mod1(180-\frac{180}{m})} &= M_{fmod1} \sum_{i=1}^{m-1} \cos\left(-\frac{\pi}{2} + \frac{\pi}{m} + \frac{\pi}{m}(i-1)\right) \\
 &= \frac{1}{2} i_a B_{sr} D_{sr} L_{ring} p W_s \sum_{i=1}^{m-1} \cos\left(-\frac{\pi}{2} + \frac{\pi}{m} + \frac{\pi}{m}(i-1)\right) \\
 &= \frac{\pi}{2} A_{sr} B_{sr} D_{sr}^2 L_{ring} K_{mod1(180-\frac{180}{m})}, \tag{33}
 \end{aligned}$$

where $K_{mod1(180-\frac{180}{m})}$ – the coefficient of efficiency of model 1 for $(180-180/m)$ -degree commutation

$$K_{mod1(180-\frac{180}{m})} = \frac{\sum_{i=1}^{m-1} \cos\left(-\frac{\pi}{2} + \frac{\pi}{m} + \frac{\pi}{m}(i-1)\right)}{2m}. \tag{34}$$

The graphical dependence of this coefficient on the number of phases for $(180-180/m)$ - degree commutation (Eq. (34)) is shown in **Figure 15**.

For 180-degree commutation

$$\begin{aligned}
 M_{max\ mod1(180)} &= M_{fmod1} \sum_{i=1}^m \cos\left(-\frac{\pi}{2} + \frac{\pi}{2m} + \frac{\pi}{m}(i-1)\right) \\
 &= \frac{1}{2} i_a B_{sr} D_{sr} L_{ring} p W_s \sum_{i=1}^m \cos\left(-\frac{\pi}{2} + \frac{\pi}{2m} + \frac{\pi}{m}(i-1)\right) \\
 &= \frac{\pi}{2} A_{sr} B_{sr} D_{sr}^2 L_{ring} K_{mod1(180)}. \tag{35}
 \end{aligned}$$

where $K_{mod1(180)}$ – efficiency coefficient of model 1 on the number of phases for 180- degree commutation

$$K_{mod1(180)} = \frac{\sum_{i=1}^m \cos\left(-\frac{\pi}{2} + \frac{\pi}{2m} + \frac{\pi}{m}(i-1)\right)}{2m}. \tag{36}$$

The graphical dependence of this coefficient on the number of phases for 180-degree switching (Eq.(36)) is shown in **Figure 16**.

Physical meaning of the efficiency coefficients of the model is to determine the share that the phases invest in creating the maximum moment.

Let us determine the average electromagnetic moment and electromagnetic power for the model1 BMAMF for various switching options, taking into account the efficiency coefficients derived above.

For $(180-180/m)$ - degree commutation:

$$M_{sr\ mod1(180-\frac{180}{m})} = \frac{\pi}{2} A_{sr} B_{sr} D_{sr}^2 L_{ring} K_{mod1(180-\frac{180}{m})} K_{ef(180-\frac{180}{m})}; \tag{37}$$

$$P_{el\ mod1(180-\frac{180}{m})} = \frac{\pi}{2} A_{sr} B_{sr} \omega D_{sr}^2 L_{ring} K_{mod1(180-\frac{180}{m})} K_{ef(180-\frac{180}{m})}, \tag{38}$$

where ω – rotation speed in rad/s.

For 180 - degree commutation:

$$M_{sr\ mod1(180)} = \frac{\pi}{2} A_{sr} B_{sr} D_{sr}^2 L_{ring} K_{mod1(180)} K_{ef180}; \tag{39}$$

$$P_{el\ mod1(180)} = \frac{\pi}{2} A_{sr} B_{sr} \omega D_{sr}^2 L_{ring} K_{mod1(180)} K_{ef180}. \tag{40}$$

It is of theoretical interest to choose the most efficient type of switching for model 1 with the same electromagnetic loads and in the same dimensions. For

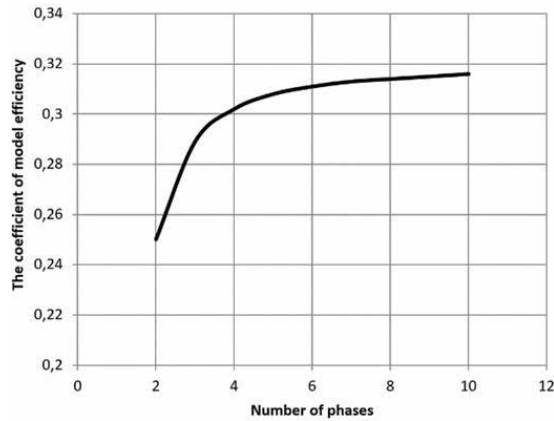


Figure 15.
 Dependence of the efficiency coefficient of model 1 on the number of phases for (180–180/m) - degree commutation.

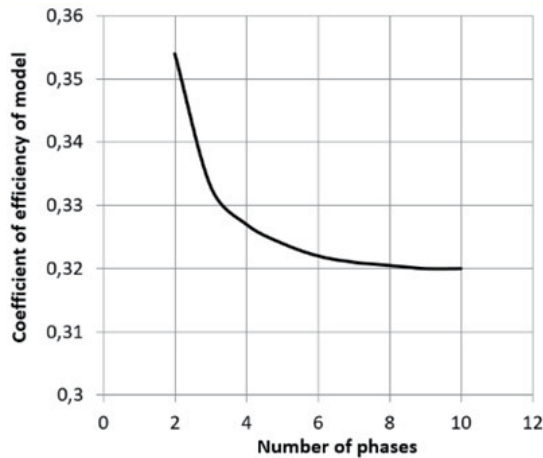


Figure 16.
 Dependence of the efficiency coefficient of model 1 on the number of phases for 180 - degree commutation.

quantitative evaluation, we introduce the commutation comparison coefficient as the ratio of electromagnetic powers (180–180/m) - degree commutation and 180-degree commutation:

$$K_{comp_com_mod1} = \frac{P_{el\ mod1(180-\frac{180}{m})}}{P_{el\ mod1(180)}} = \frac{K_{mod1(180-\frac{180}{m})}K_{ef(180-\frac{180}{m})}}{K_{mod1(180)}K_{ef180}} \quad (41)$$

The graphical dependence of this coefficient on the number of phases is shown in **Figure 17**.

The dependence analysis shows that for model 1, 180-degree commutation has an advantage with a small number of phases. As the number of phases increases, this advantage decreases.

3.3 Electromagnetic moment and electromagnetic power for BMAMF with segment magnets and trapezoidal coils

A sketch of the magnetic system and the BAMF armature winding of this design is shown in **Figure 18**. Let us refer to this design as model 2.

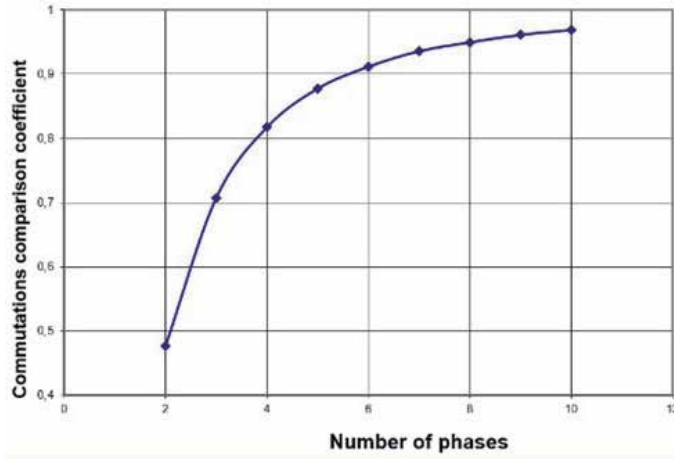


Figure 17. Dependence of the commutations comparison coefficient for model 1.

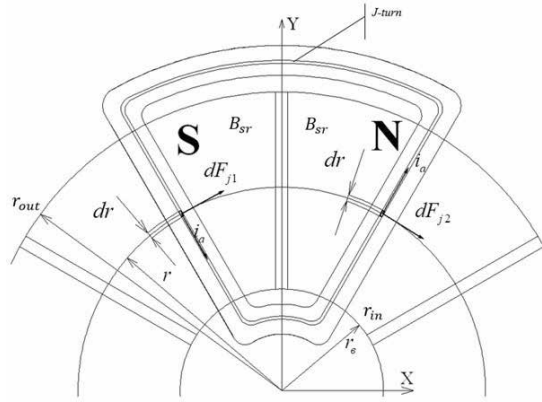


Figure 18. Sketch of the magnetic system and armature winding BMAMF with segment magnets and trapezoidal armature windings.

Let us select elementary conductors of length dr on an arbitrary j -turn of the winding and define elementary moments for them. They will be a function of the angular position and radius of the elementary section.

$$dM(\alpha, r)_{1j} = dM(\alpha, r)_{2j} = i_a B(\alpha) r dr, \quad (42)$$

where r – radius, where the elementary conductor is located.
Electromagnetic moment j -th of the turn

$$M(\alpha, r)_j = \int_{r_{in}}^{r_{out}} dM(\alpha, r)_{1j} + \int_{r_{in}}^{r_{out}} dM(\alpha, r)_{2j} = 2i_a B(\alpha) \frac{r_{out}^2 - r_{in}^2}{2}. \quad (43)$$

Electromagnetic moment of the phase section

$$M(\alpha, r)_{W_s} = \sum_{j=1}^{W_s} dM(\alpha, r)_j = 2i_a B(\alpha) \frac{r_{out}^2 - r_{in}^2}{2} W_s. \quad (44)$$

Electromagnetic moment of an arbitrary i -th phase

$$M(\alpha, r)_{fi\ mod\ 2} = M(\alpha, r)_{W_s p} = 2i_a B(\alpha) \frac{r_{out}^2 - r_{in}^2}{2} W_s p. \quad (45)$$

The maximum moment of all phases in the intercommutation interval will depend on the pole overlap coefficient of the magnetic system, determined by equation (Eq. (1)), the number of phases, and the type of switching. Let us determine the influence of these factors on model 2. By analogy with model 1, we introduce the efficiency coefficient of model 2, which is the ratio of the maximum moment of the armature winding at the real pole overlap coefficient to the maximum moment at the theoretical pole overlap coefficient equal to 1.0. As a rule, the distance between the side faces of permanent magnets is the same on the inner and outer diameters. In this case, the pole overlap coefficient changes linearly when moving from the inner diameter to the outer one. Therefore, analytical expressions can be derived for the average diameter of a ring with magnets and further use this linear relationship.

For (180–180/m)-degree commutation, the efficiency coefficient of the model is defined by the following expression

$$K_{mod2(180-\frac{180}{m})}(\alpha, m) = \frac{M(\alpha_{sr}, m)_{(180-\frac{180}{m})\ max}}{M(\alpha_{sr} = 1, m)_{(180-\frac{180}{m})\ max}} = \frac{M(\alpha_{sr}, m)_{(180-\frac{180}{m})\ max}^*}{\frac{\pi}{m}(m-1)}, \quad (46)$$

where α_{sr} – real coefficient of pole overlap on the average ring diameter of the magnetic system;

$M(\alpha_{sr}, m)_{(180-\frac{180}{m})\ max}$ – maximum moment of the armature winding at the real coefficient of pole overlap;

$M(\alpha_{sr} = 1, m)_{(180-\frac{180}{m})\ max}$ – the maximum moment of the armature winding with a pole overlap coefficient equal to 1, which is only theoretically possible;

$M(\alpha_{sr}, m)_{(180-\frac{180}{m})\ max}^*$ – relative value of the maximum moment of the armature winding at the real coefficient of pole overlap.

The relative value of the maximum moment of the armature winding can be determined from the expression (Eq. (17)) for the offset of the armature from the neutral by $x = \frac{\pi}{2m}$ (see **Figure 19**)

$$M(\alpha_{sr}, m)_{(180-\frac{180}{m})\ max}^* = M_{(180-\frac{180}{m})\ max}^* \left(\frac{\pi}{2m} \right) = \sum_{i=1}^{m-1} M_{fi}^* \left(\frac{\pi}{2m} \right). \quad (47)$$

The physical meaning of the efficiency coefficient of model 2 is similar to the coefficient for model 1. The graphical dependence of the coefficient for (180–180/m) - degree switching (Eq.(46)) is shown in **Figure 20**.

Taking into account the introduced efficiency coefficient of the model, we can write the following expression of the maximum electromagnetic moment for (180–180/m) - degree commutation

$$\begin{aligned} M_{\max\ mod2(180-\frac{180}{m})} &= \sum_{i=1}^{m-1} M(\alpha, m)_{fi\ mod2} K_{mod2(180-\frac{180}{m})} \\ &= 2i_a B_\delta \frac{r_{out}^2 - r_{in}^2}{2} W_s p K_{mod2(180-\frac{180}{m})} = \frac{\pi}{2} A_{sr} B_\delta D_{sr}^2 L_{ring} K_{mod2(180-\frac{180}{m})}. \end{aligned} \quad (48)$$

Average electromagnetic moment and electromagnetic power for $(180-180/m)$ - degree commutation

$$M_{srmod2(180-\frac{180}{m})} = M_{\max mod2(180-\frac{180}{m})} K_{ef(180-\frac{180}{m})} = \frac{\pi}{2} A_{sr} B_{\delta} D_{sr}^2 L_{ring} K_{mod2(180-\frac{180}{m})} K_{ef(180-\frac{180}{m})}; \quad (49)$$

$$P_{elmod2(180-\frac{180}{m})} = \frac{\pi}{2} A_{sr} B_{\delta} \omega D_{sr}^2 L_{ring} K_{mod2(180-\frac{180}{m})} K_{ef(180-\frac{180}{m})}. \quad (50)$$

By analogy, we derive the equations for 180-degree commutation.

For 180-degree switching, the efficiency coefficient of the model is defined by the following expression

$$K_{mod2(180)}(\alpha, m) = \frac{M(\alpha_{sr}, m)_{(180)max}}{M(\alpha_{sr} = 1, m)_{(180)max}} = \frac{M(\alpha_{sr}, m)_{(180)max}^*}{\pi}, \quad (51)$$

where $M(\alpha_{sr}, m)_{(180)max}$ – maximum moment of the armature winding at the real coefficient of pole overlap;

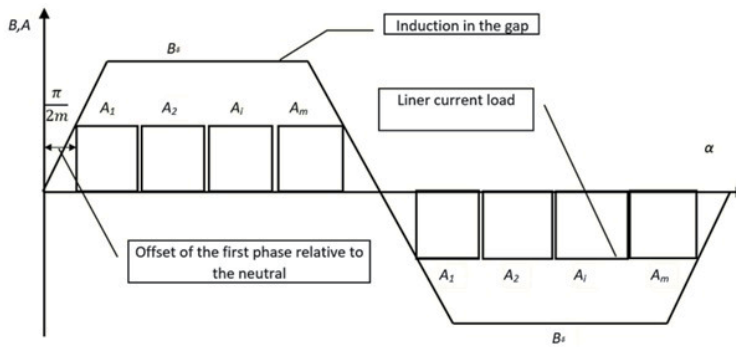


Figure 19. Position of multiphase armature winding sections at the maximum electromagnetic moment for $(180-180/m)$ -degree commutation.

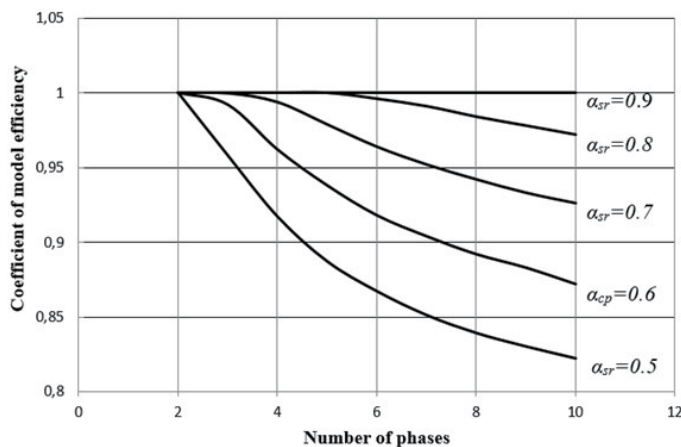


Figure 20. Efficiency coefficient of model 2 for $(180-180/m)$ - degree switching at different values of the number of phases and the coefficient of pole overlap on the average diameter of the ring of the magnetic system.

$M(\alpha_{sr} = 1, m)_{(180)max}$ – maximum moment of the armature winding with a pole overlap coefficient equal to 1, which is only theoretically possible;

$M(\alpha_{sr}, m)_{(180)max}^*$ – relative value of the maximum moment of the armature winding at the real coefficient of pole overlap.

Efficiency coefficient of model 2 for 180 - degree switching at different the coefficient of pole overlap on the average diameter of the ring of the magnetic system (Eq. (51)) is shown at **Figure 22**. We can see that this coefficient does not depend on the number of phases.

The relative value of the maximum moment of the armature winding can be determined from the expression (Eq.(21)) for the zero offset of the armature from the neutral (see **Figure 21**)

$$M(\alpha_{sr}, m)_{(180)max}^* = M_{(180)max}^*(0) = \sum_{i=1}^m M_{fi}^*(0). \quad (52)$$

Maximum electromagnetic torque for 180-degree commutation

$$\begin{aligned} M_{\max mod2(180)} &= \sum_{i=1}^m M(\alpha.r)_{fi \max mod2(180)} K_{mod2(180)} = 2i_a B_\delta \frac{r_{out}^2 - r_{in}^2}{2} W_{sp} K_{mod2(180)} \\ &= \frac{\pi}{2} A_{sr} B_\delta D_{sr}^2 L_{ring} K_{mod2(180)}. \end{aligned} \quad (53)$$

The average electromagnetic torque and electromagnetic power for 180-degree commutation

$$M_{sr mod2(180)} = M_{\max mod2(180)} K_{ef(180)} = \frac{\pi}{2} A_{sr} B_\delta D_{sr}^2 L_{ring} K_{mod2(180)} K_{ef(180)}; \quad (54)$$

$$P_{el mod2(180)} = \frac{\pi}{2} A_{sr} B_\delta \omega D_{sr}^2 L_{ring} K_{mod2(180)} K_{ef(180)}. \quad (55)$$

By analogy with the previous analysis, for quantitative evaluation, we introduce the switching comparison coefficient, as the ratio of electromagnetic powers (180–180/m) - degree commutation and 180-degree commutation:

$$K_{comp_com_mod2} = \frac{P_{el mod2(180-\frac{180}{m})}}{P_{el mod2(180)}} = \frac{K_{mod2(180-\frac{180}{m})} K_{ef(180-\frac{180}{m})}}{K_{mod2(180)} K_{ef180}}. \quad (56)$$

The graphical dependence of this coefficient on the number of phases and the coefficient of the pole arc (Eq.(56)) is shown in **Figure 23**.

It should be noted that such a comparative analysis makes sense only for the same electromagnetic loads: induction in the air gap and linear load on the average diameter of the disk of the magnetic system.

These dependencies are of great practical importance. Their analysis shows that for the same electromagnetic loads, magnetic systems with a high value of the pole overlap coefficient have an advantage for any number of phases. Graphic dependences of the switching comparison coefficient are below 1.0. However, for magnetic systems with a pole overlap coefficient of 0.7–0.5, which is very typical for practice, the advantage is (180–180/m) - degree commutation for the number of phases starting from 3 and higher.

Given that (180–180/m) - degree commutation has a simpler and cheaper technical implementation, this theoretical conclusion is of great practical importance.

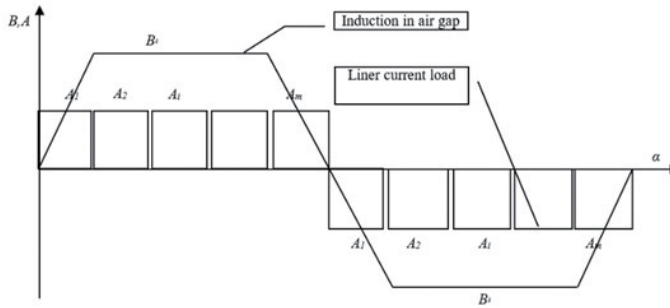


Figure 21. Position of multiphase armature winding sections at the maximum electromagnetic moment for 180-degree commutation.

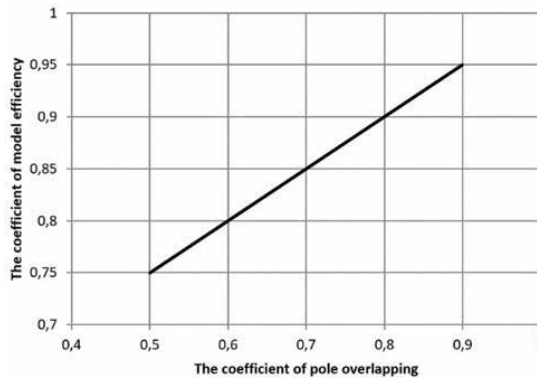


Figure 22. The efficiency coefficient of model 2 for 180-degree commutation at different values of the pole overlap coefficient on the average diameter of the ring of the magnetic system.

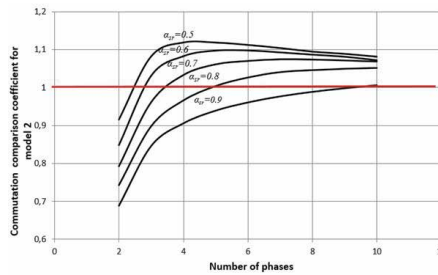


Figure 23. Dependence of the comparison coefficient (180–180/m) - degree commutation and 180-degree commutation for model 2.

3.4 Electromagnetic moment and electromagnetic power for BMAMF with segment magnets and toroidal coils

The analysis will be carried out by analogy with the previous models. A sketch of the magnetic system and armature winding BMAMF of this design is shown in **Figure 24**. Let us designate this design as model 3.

Let us select an elementary conductor of length dr on an arbitrary j -th turn of the winding and determine the elementary moment for it.

$$dM(\alpha, r)_j = i_a B(\alpha) r dr. \quad (57)$$

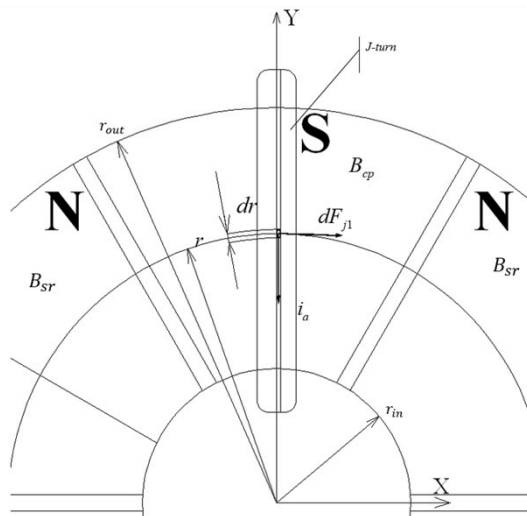


Figure 24. Sketch of the magnetic system and armature windings BMAMF with segment magnets toroidal armature windings.

Electromagnetic moment j -th of the turn

$$M(\alpha, r)_j = \int_{r_{in}}^{r_{out}} dM(\alpha, r)_j = 2i_a B(\alpha) \frac{r_{out}^2 - r_{in}^2}{2}. \quad (58)$$

Electromagnetic moment of the phase section

$$M(\alpha, r)_{W_S} = \sum_{j=1}^{W_S} dM(\alpha, r)_j = 2i_a B(\alpha) \frac{r_{out}^2 - r_{in}^2}{2} W_S. \quad (59)$$

Maximum value of the electromagnetic moment of an arbitrary i -th phase

$$M(\alpha, r)_{f_{imod3}} = M(\alpha, r)_{W_S} p = 2i_a B(\alpha) \frac{r_{out}^2 - r_{in}^2}{2} W_S 2p. \quad (60)$$

By analogy with model 2, we introduce the efficiency coefficient of model 3, which is the ratio of the maximum moment of the armature winding at the real pole overlap coefficient to the maximum moment at the theoretical pole overlap coefficient equal to 1.0. It should be noted that the electromagnetic moment for model 3 is 2 times higher than the electromagnetic moment of model 1. This can be seen from the comparison of equation (Eq. (47)) and equation (Eq. (61)). From a physical point of view, this is because with the same external and internal diameters of the magnetic system, the electromagnetic moment in model 3 is created from 2 sides. We will consider this in the following equations.

For $(180-180/m)$ -degree communication the efficiency coefficient of the model is defined by the following expression

$$K_{mod3(180-\frac{180}{m})}(\alpha, m) = \frac{M(\alpha_{sr}, m)_{(180-\frac{180}{m})max}}{M(\alpha_{sr} = 1, m)_{(180-\frac{180}{m})max}} = \frac{2M(\alpha_{sr}, m)_{(180-\frac{180}{m})max}^*}{\frac{\pi}{m}(m-1)}. \quad (61)$$

The relative value of the maximum moment of the armature winding, which is created on one side of the working air gap, can be determined from the expression (Eq. (17)), for the displacement of the armature from the neutral poles by an amount $x = \frac{\pi}{2m}$.

The graphical dependence of the coefficient for (180–180/m) - degree commutation is shown in **Figure 25**.

Maximum electromagnetic torque for (180–180/m)-degree commutation

$$M_{\max \text{ mod}3(180-\frac{180}{m})} = \sum_{i=1}^{m-1} M(\alpha, m)_{fi \text{ mod}3} K_{\text{mod}3(180-\frac{180}{m})} =$$

$$= 2i_a B_\delta \frac{r_{\text{out}}^2 - r_{\text{in}}^2}{2} W_{sp} K_{\text{mod}3(180-\frac{180}{m})} = \frac{\pi}{2} A_{sr} B_\delta D_{sr}^2 L_{ring} K_{\text{mod}3(180-\frac{180}{m})}. \quad (62)$$

Average electromagnetic moment and electromagnetic power for (180–180/m) - degree commutation, based on the above

$$M_{\text{sr mod}3(180-\frac{180}{m})} = M_{\max \text{ mod}3(180-\frac{180}{m})} K_{ef(180-\frac{180}{m})}$$

$$= \frac{\pi}{2} A_{sr} B_\delta D_{sr}^2 L_{ring} K_{\text{mod}3(180-\frac{180}{m})} K_{ef(180-\frac{180}{m})} \quad (63)$$

$$P_{\text{el mod}3(180-\frac{180}{m})} = \frac{\pi}{2} A_{sr} B_\delta \omega D_{sr}^2 L_{ring} K_{\text{mod}3(180-\frac{180}{m})} K_{ef(180-\frac{180}{m})}. \quad (64)$$

By analogy, we derive the equations for 180-degree switching.

For 180-degree commutation the efficiency coefficient of the model is defined by the following expression

$$K_{\text{mod}3(180)}(\alpha, m) = \frac{M(\alpha_{sr}, m)_{(180) \max}}{M(\alpha_{sr} = 1, m)_{(180) \max}} = \frac{2M(\alpha_{sr}, m)_{(180) \max}^*}{\pi}. \quad (65)$$

The relative value of the maximum moment of the armature winding can be determined from the expression (1.16) for the zero offset of the armature from the neutral (see **Figure 21**).

By analogy with model 2, the efficiency coefficient of model 3 for this type of switching will not depend on the number of phases and will be determined only by the value of the overlap coefficient on the average ring diameter of the magnetic system. The graphical dependence of this coefficient is shown in **Figure 26**.

Maximum electromagnetic torque for 180-degree commutation

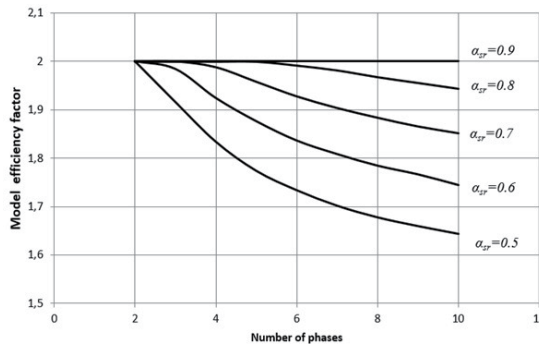


Figure 25.

The efficiency coefficient of model 3 for (180–180/m) - degree commutation at different values of the number of phases and the coefficient of pole overlap on the average diameter of the ring of the magnetic system.

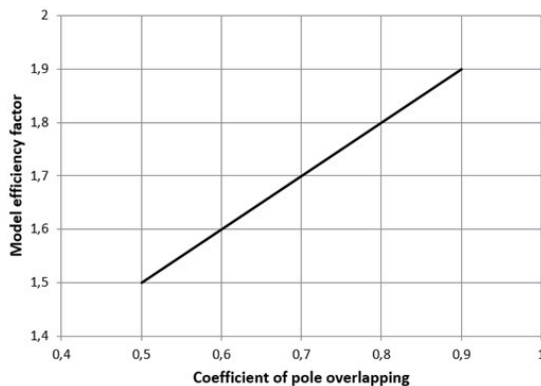


Figure 26. Model 3 efficiency coefficient for 180-degree commutation with different values of the pole overlap coefficient on the average ring diameter of the magnetic system.

$$\begin{aligned}
 M_{\max \text{mod}3(180)} &= \sum_{i=1}^m M(\alpha.r)_{f_{i \max \text{mod}3(180)}} K_{\text{mod}3(180)} = 2i_a B_\delta \frac{r_{\text{out}}^2 - r_{\text{in}}^2}{2} W_{sp} K_{\text{mod}3(180)} \\
 &= \frac{\pi}{2} A_{sr} B_\delta D_{sr}^2 L_{ring} K_{\text{mod}3(180)}.
 \end{aligned} \tag{66}$$

The average electromagnetic torque and electromagnetic power for 180-degree commutation

$$M_{\text{srmod}3(180)} = M_{\max \text{mod}3(180)} K_{ef(180)} = \frac{\pi}{2} A_{sr} B_\delta D_{sr}^2 L_{ring} K_{\text{mod}3(180)} K_{ef(180)}; \tag{67}$$

$$P_{el \text{mod}3(180)} = \frac{\pi}{2} A_{sr} B_\delta \omega D_{sr}^2 L_{ring} K_{\text{mod}3(180)} K_{ef(180)}. \tag{68}$$

By analogy with the previous analysis, for quantitative evaluation, we introduce the switching comparison coefficient for model 3 as the ratio of electromagnetic powers (180–180/m) - degree commutation and 180-degree commutation:

$$K_{\text{comp_com_mod}3} = \frac{P_{el \text{mod}3(180 - \frac{180}{m})}}{P_{el \text{mod}3(180)}} = \frac{K_{\text{mod}3(180 - \frac{180}{m})} K_{ef(180 - \frac{180}{m})}}{K_{\text{mod}3(180)} K_{ef180}}. \tag{69}$$

Since the analytical dependences of the efficiency coefficient for model 2 and model 3 are multiples of 2, the graphical dependence of this coefficient on the number of phases for different values of the pole overlap coefficient completely coincides with the curves shown in **Figure 23** for model 3, we can draw conclusions similar to those for model 2 regarding the advantages of commutations types when changing the number of phases and the pole overlap coefficient.

3.5 Electromagnetic moment and electromagnetic power for BMAMF with segment magnets and toothed anchor

The armature winding for this design can be made by analogy with a radial design (wave or loop) or toroidal. It should be noted that the windings for these three options would differ only in the shape of the frontal parts, which will only affect the calculation of active and inductive resistances. The active zone with copper (the groove-tooth zone) will be identical for all variants. Consequently, the electromagnetic processes of mutual conversion of electromagnetic and mechanical energy will also be identical. This allows you to combine all design types with a

toothed anchor into one basic model. We denote it as model 4. to analyze the tooth structure, we apply a well-known technique: we place all the ampere-conductors in a uniform layer on the armature surface in the working air gap with an equivalent linear current load. The value of the induction in the gap for this model will be considered equivalent to the real induction. If this assumption is accepted, all analytical expressions, including the electromagnetic moment, electromagnetic power, and model efficiency coefficients, will be similar to the expressions for model 3.

The average electromagnetic torque and electromagnetic power for (180–180/m)-degree commutation on the basis of the above

$$\begin{aligned} M_{srmod4(180-\frac{180}{m})} &= M_{\max mod4(180-\frac{180}{m})} K_{ef(180-\frac{180}{m})} \\ &= \frac{\pi}{2} A_{sr} B_{\delta} D_{sr}^2 L_{ring} K_{mod4(180-\frac{180}{m})} K_{ef(180-\frac{180}{m})}; \end{aligned} \quad (70)$$

$$P_{elmod4(180-\frac{180}{m})} = \frac{\pi}{2} A_{sr} B_{\delta} \omega D_{sr}^2 L_{ring} K_{mod4(180-\frac{180}{m})} K_{ef(180-\frac{180}{m})}. \quad (71)$$

where $K_{mod4(180-\frac{180}{m})}$ – the efficiency coefficient of the model, determined by **Figure 25**.

The average electromagnetic torque and electromagnetic power for 180-degree commutation

$$M_{srmod4(180)} = M_{\max mod4(180)} K_{ef(180)} = \frac{\pi}{2} A_{sr} B_{\delta} D_{sr}^2 L_{ring} K_{mod4(180)} K_{ef(180)}; \quad (72)$$

$$P_{elmod4(180)} = \frac{\pi}{2} A_{sr} B_{\delta} \omega D_{sr}^2 L_{ring} K_{mod4(180)} K_{ef(180)}. \quad (73)$$

where $K_{mod4(180)}$ – the efficiency coefficient of the model, determined by **Figure 26**.

It should be noted that, despite the analogy with model 3, the value of the average electromagnetic power and electromagnetic moment for model 4 would be approximately 4–6 times higher due to higher values of electromagnetic loads (induction in the gap and linear current load on the average armature diameter).

3.6 Comparative analysis of structures at (180–180/m) - degree commutation and 180-degree commutation

This analysis allows us to make a qualitative assessment of the effectiveness of models in terms of the development of the electromagnetic moment in the same volumes. Prong models are more efficient than models with a smooth anchor due to the large values of electromagnetic loads. For a BMAMF with a smooth anchor, due to different values of the model coefficient, we can conclude: model 2 is more efficient than model 1 and model 3 is more efficient than model 2 and, accordingly, model 1. A quantitative analysis of this efficiency is of Practical interest.

We perform this analysis using the following method: for a fixed number of phases, we determine the ratio of electromagnetic powers for different models and different switching options. For a BMAMF with a smooth armature, the value of the electromagnetic loads will be considered the same. The air gap induction value for the toothed armature is approximately 1.6 times higher than the gap induction value for the model 3 smooth armature (80% of the residual permanent magnet induction for the toothed armature and 50% for the smooth armature). Approximately the same ratio can be assumed for linear loads. These relations are confirmed by practical tests. Therefore, for a comparative analysis for model 4, you can enter an increasing coefficient of 2.56 compared to model 3. The Results are summarized in the table.

Table 1 shows a comparison of models for the variant: pole arc coefficient 0.8, number of phases 3, 120-degree commutation.

Table 2 shows a comparison of models for the variant: pole arc coefficient 0.8, number of phases 3, 180-degree commutation.

Tables 1 and **2** show that model 4 is the most efficient in terms of the electromagnetic moment and electromagnetic power.

These tables are convenient to use in practice for choosing the design and type of switching depending on the project.





Comparison of 3-phase models for 120-degree commutation and the pole arc coefficient 0.8		The model to compare with			
		Model 1	Model 2	Model 3	Model 4
Model for comparison	Model 1 	1	0.577	0.288	0.113
	Model 2 	1.733	1	0.5	0.195
	Model 3 	3.466	2	1	0.391
	Model 4 	8.87	5.12	2.56	1

Table 1. Comparison of the efficiency of models based on the developed electromagnetic moment for 120-degree switching.


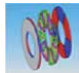


Comparison of 3-phase models for 180-degree commutation and the pole arc coefficient 0.8		The model to compare with			
		Model 1	Model 1	Model 1	Model 1
Model for comparison	Model 1 	1	0.667	0.333 π	0.13
	Model 1 	1.499	1	0.5	0.195
	Model 1 	3.0	2	1	0.391
	Model 1 	7.68	5.12	2.56	1

Table 2. A similar comparison for 180-degree commutation.

4. Conclusion

BMAMP is a new class of electric machines. Their use is expanding for electric drives for General industrial applications and special applications in medicine, space and robotics. The theory of their analysis is not fully developed. These studies expand the possibilities of this analysis. The following main conclusions can be drawn from the presented research.

1. Classification of the main types of commutations is carried out. For a BMAMP with an arbitrary number of phases the discrete $(180-180/m)$ -degree commutation and 180-degree commutation with galvanically isolated phase supply are selected.
2. The efficiency factor of the armature winding for various types of commutations is given. It is convenient to use this factor to compare the efficiency of commutation types.
3. The influence of the number of phases on the developed electromagnetic moment for $(180-180/m)$ -degree switching and 180-degree switching is analyzed. It is proved that to increase the electromagnetic moment in the same dimensions and with the same electromagnetic loads, it is necessary to increase the number of phases and the pole arc coefficient for both types of commutation.
4. Classification of BMAMF designs based on the shape of permanent magnets and armature winding sections is carried out. Basic models for analysis are defined.
5. The resulting equation of the electromagnetic torque and electromagnetic power for base structures is given. The equations determine the dependence of energy indicators on the main dimensions, electromagnetic loads, design features, and type of commutation. Model efficiency factors are derived for all basic models.
6. The comparative analysis of the effectiveness of the basic models for electromagnetic power for the same dimensions and the same electromagnetic loads is carried out. The results of the analysis are summarized in tables for different types of switching and the number of phases, quantitatively showing the advantages of one design over another. Tables are convenient to use in engineering practice to select the best option depending on the project situation.


Further research will be aimed at developing methods for computer-aided design of machines of this class.

Author details

Sergey Gandzha* and Dmitry Gandzha
South Ural State University, Chelyabinsk, Russia

*Address all correspondence to: gandzhasa@susu.ru

IntechOpen

© 2021 The Author(s). Licensee IntechOpen. This chapter is distributed under the terms of the Creative Commons Attribution License (<http://creativecommons.org/licenses/by/3.0>), which permits unrestricted use, distribution, and reproduction in any medium, provided the original work is properly cited. 

References

- [1] Gandzha, S.A Application of the Ansys Electronics Desktop Software Package for Analysis of Claw-Pole Synchronous Motor / S.A. Gandzha, B.I. Kosimov, D.S. Aminov //Machines.– 2019.–Vol. 7 No. 4 <https://ieeexplore.ieee.org/document/8570132> DOI: 10.1109/GloSIC.2018.8570132
- [2] Gandzha, S. Selecting Optimal Design of Electric Motor of Pilgrim Mill Drive for Manufacturing Techniques Seamless Pipe / S. Gandzha, B. Kosimov, D. Aminov //2019 International Conference on Industrial Engineering, Applications and Manufacturing, ICIEAM 2019.–2019 <https://ieeexplore.ieee.org/document/8742941> DOI: 10.1109/ICIEAM.2019.8742941
- [3] I.E. Kiessh, S.A. Gandzha, “Application of Brushless Machines with Combine Excitation for a Small and Medium Power Windmills”, *Procedia Engineering*.– 2016.–Vol. 129.– P.191–194, DOI: 10.1016/j.proeng.2016.12.031 <https://www.sciencedirect.com/science/article/pii/S1877705815039156?via%3Dihub>
- [4] Gandzha, S., Andrey, S., Andrey, M., Kiessh, I. The design of the low-speed brushless motor for the winch which operates in sea-water. *International Multidisciplinary Scientific GeoConference Surveying Geology and Mining Ecology Management, SGEM*
- [5] Gandzha, S. The application of the double-fed alternator for the solving of the wind power problems. *International Multidisciplinary Scientific GeoConference Surveying Geology and Mining Ecology Management, SGEM*
- [6] Gandzha S.A., Sogrin A.I., Kiessh I.E. The Comparative Analysis of Permanent Magnet Electric Machines with Integer and Fractional Number of Slots per Pole and Phase. *Procedia Engineering* 129: 408–414, December 2015.
- [7] Gandzha S., Aminov D., Bakhtiyor K. Application of the combined excitation submersible hydrogenerator as an alternative energy source for small and medium rivers. *IEEE Russian Workshop on Power Engineering and Automation of Metallurgy Industry*. 4–5 Oct. 2019 Magnitogorsk, Russia. DOI: 10.1109 / PEAMI.2019.8915294
- [8] Aydin, M. S. Huang and T. A. Lipo. “Axial Flux Permanent Magnet Disc Machines: A Review”, In *Conf. Record of SPEEDAM*, , May 2004, pp. 61–71
- [9] Akatsu K. and Wakui S. “A comparison between axial and radial flux PM motor by optimum design method from the required NTcharacteristics”, *Conference Proceeding of ICEM2004*, No. 361, Cracow-Poland, 2004.
- [10] Gandzha, S., Kiessh, I. The high-speed axial gap electric alternator is the best solution for a gas turbine engine. The high-speed axial gap electric alternator is the best solution for a gas turbine engine. *International Multidisciplinary Scientific GeoConference Surveying Geology and Mining Ecology Management, SGEM*.
- [11] Gandzha, S. Development of engineering technique for calculating magnet systems with permanent magnets / S. Gandzha, E. Kiessh, D.S. Aminov //Proceedings - 2018 International Conference on Industrial Engineering, Applications and Manufacturing, ICIEAM 2018.–2018 No. 10.15593/2224-9397/2019.1.04 <https://ieeexplore.ieee.org/document/8728650> DOI:10.1109/ICIEAM.2018.8728650
- [12] Gandzha S., Bakhtiyor K., Aminov D. Development of a system of multi-level optimization for Brushless Direct Current Electric Machines. *International Ural Conference on Electrical Power Engineering (Ural*

Con) 2019. 1–3 Oct. 2019 Chelyabinsk, Russia. DOI: 10.1109/URALCON.2019.8877650

[13] Gandzha, S., Kiessh, I. Selection of winding commutation for axial gap machines with any phases. Proceedings - 2018 International Conference on Industrial Engineering, Applications and Manufacturing, ICIEAM 2018

[14] Gandzha S.A. Application of Digital Twins Technology for Analysis of Brushless Electric Machines with Axial Magnetic Flux / Gandzha, S. // Proceedings - 2018 Global Smart Industry Conference, GloSIC 2018.– 2018 <https://ieeexplore.ieee.org/document/8570132> DOI:10.1109/GloSIC.2018.8570132

[15] Gandzha, S. Design of Brushless Electric Machine with Axial Magnetic Flux Based on the Use of Nomograms / S. Gandzha, D. Aminov, B. Kosimov // Proceedings - 2018 International Ural Conference on Green Energy, UralCon 2018.–2018.– P.282–287 <https://ieeexplore.ieee.org/document/8544320> DOI: 10.1109/URALCON.2018.8544320

Detection of Stator and Rotor Asymmetries Faults in Wound Rotor Induction Machines: Modeling, Test and Real-Time Implementation

Shahin Hedayati Kia

Abstract

This chapter deals with detection of stator and rotor asymmetries faults in wound rotor induction machines using rotor and stator currents signatures analysis. This is proposed as the experimental part of *fault diagnosis in electrical machines* course for master's degree students in electrical engineering at University of Picardie "Jules Verne". The aim is to demonstrate the main steps of real-time condition monitoring development for wound rotor induction machines. In this regard, the related parameters of classical model of wound rotor induction machine under study are initially estimated. Then, the latter model is validated through experiments in both healthy and faulty conditions at different levels of the load. Finally, an algorithm is implemented in a real-time data acquisition system for online detection of stator and rotor asymmetries faults. An experimental test bench based on a three-phase 90 W wound rotor induction machine and a real-time platform for hardware-in-the-loop test are utilized for validation of the proposed condition monitoring techniques.

Keywords: AC motor protection, asynchronous rotating machines, fault diagnosis, Fourier transform, hardware-in-the-loop, induction motors, monitoring, signal processing

1. Introduction

Fault diagnosis of electrical machines is a very active topic of research and several books have been published, which detail new developed techniques for efficient condition monitoring of electrical machines. The run-to-break is an unplanned strategy of maintenance that needs to be avoided at the expense of high emergency repair cost. By means of preventive maintenance at regular intervals, which is commonly shorter than the expected time between failures, the maintenance actions can be planned in advance. Any potential breakdown in industrial systems can be predicted through the condition based maintenance (CBM) so called 'predictive maintenance' which gives a reasonable remaining useful life and leads consequently to the optimum time maintenance planning [1]. Since the electrical machines are the key components of the majority of industrial processes, it is essential to setup a CBM in order to minimize their downtime and consequently

increase their availability [2, 3]. Modeling and numerical simulations are the initial design stage of fault detection and diagnosis (FDD) systems [4]. For prototyping and testing both software-in-the-loop (S-i-L) and hardware-in-the-loop (H-i-L) realizations can be performed before the final stage of FDD system integration [4]. This leads to a better evaluation of FDD methods in all possible working condition scenarios which are sometimes hard to acquire in real practice using an experimental test bench. In this chapter, the illustration of these previous stages to Masters' degree students who attend to assimilate the ability of FDD technique development for electrical systems will be highlighted. The example of wound rotor induction machine (WRIM) is a good choice since WRIMs have been widely used in electrical power generation, particularly as doubly fed induction generators (DFIGs) in variable speed wind turbines. Moreover, the internal circuit parameters of a WRIM can be easily deduced using some basic experimental electrical circuit tests. The asymmetry fault in practice can be obtained by adding series resistance in one phase of stator and/or rotor winding which simplifies the evaluation of FDD methods through both numerical simulations and experiments. The state-of-the-art methods for FDD of asymmetries in WRIMs have been well detailed [5]. However, the implementation of FDD algorithms in real-time systems has been rarely investigated [6]. Recently, the H-i-L configuration is used for static eccentricity analysis in induction machines (IMs). However, the proposed model is exclusively validated using finite elements method (FEM). The real-time simulation results have been demonstrated the presence of fault-related frequency components in the stator current spectrum [3]. In this regard, introducing engineering students to FDD system design for electrical machines including its development stages is totally new in the literature [7–9]. The aim of this paper is to illustrate the main stages of FDD system design for the stator asymmetry fault (SAF) as well as the rotor asymmetry fault (RAF) in WRIMs. This is proposed as the experimental part of *fault diagnosis in electrical machines* course offered to the master's degree students in electrical engineering at University of Picardie "Jules Verne". Both stator and rotor windings asymmetries are investigated. Main emphasis is dedicated to signal-based techniques which are commonly used for detection of these specific defects. It is illustrated that the stator current is directly affected by the RAF whereas the SAF has a direct influence on the rotor current [5]. The fault diagnosis is commonly performed by computing the stator/rotor current Fourier transform to identify the fault-related frequency components in the spectrum in steady-state working condition. Once the validated WRIM model is implemented in a real-time platform for H-i-L test, the measured stator and rotor currents signals, provided by the real-time system, can be analyzed by the CompactRIO data acquisition system for evaluation of signal processing tools (SPTs) in all working condition scenarios of WRIM. An experimental test bench, based on a three-phase 90 W wound rotor induction machine and a real-time platform for H-i-L tests, are utilized for validation of the proposed condition monitoring techniques.

2. Modeling of WRIM

The model of WRIM in "abc" reference frame may be expressed as [10]:

$$\mathbf{v}_{abcs} = \mathbf{r}_s \mathbf{i}_{abcs} + \frac{d}{dt} \lambda_{abcs} \quad (1)$$

$$\mathbf{v}_{abcr} = \mathbf{r}_r \mathbf{i}_{abcr} + \frac{d}{dt} \lambda_{abcr} \quad (2)$$

$$\begin{bmatrix} \lambda_{abc} \\ \lambda_{abcr} \end{bmatrix} = \begin{bmatrix} \mathbf{L}_s & \mathbf{L}_{sr} \\ \mathbf{L}_{sr}^T & \mathbf{L}_r \end{bmatrix} \begin{bmatrix} \mathbf{i}_{abc} \\ \mathbf{i}_{abcr} \end{bmatrix} \quad (3)$$

$$\mathbf{r}_s = \begin{bmatrix} r_{as} & 0 & 0 \\ 0 & r_{bs} & 0 \\ 0 & 0 & r_{cs} \end{bmatrix} \quad (4)$$

$$\mathbf{r}_r = \begin{bmatrix} r_{ar} & 0 & 0 \\ 0 & r_{br} & 0 \\ 0 & 0 & r_{cr} \end{bmatrix} \quad (5)$$

$$\mathbf{L}_s = \begin{bmatrix} L_{ls} + L_{ms} & -\frac{1}{2}L_{ms} & -\frac{1}{2}L_{ms} \\ -\frac{1}{2}L_{ms} & L_{ls} + L_{ms} & -\frac{1}{2}L_{ms} \\ -\frac{1}{2}L_{ms} & -\frac{1}{2}L_{ms} & L_{ls} + L_{ms} \end{bmatrix} \quad (6)$$

$$\mathbf{L}_r = \begin{bmatrix} L_{lr} + L_{mr} & -\frac{1}{2}L_{mr} & -\frac{1}{2}L_{mr} \\ -\frac{1}{2}L_{mr} & L_{lr} + L_{mr} & -\frac{1}{2}L_{mr} \\ -\frac{1}{2}L_{mr} & -\frac{1}{2}L_{mr} & L_{lr} + L_{mr} \end{bmatrix} \quad (7)$$

$$\mathbf{L}_{sr} = L_{sr} \times$$

$$\begin{bmatrix} \cos(\theta_r) & \cos(\theta_r + 2\pi/3) & \cos(\theta_r - 2\pi/3) \\ \cos(\theta_r - 2\pi/3) & \cos(\theta_r) & \cos(\theta_r + 2\pi/3) \\ \cos(\theta_r + 2\pi/3) & \cos(\theta_r - 2\pi/3) & \cos(\theta_r) \end{bmatrix} \quad (8)$$

$$\begin{aligned} T_e = & i_{as}L_{sr}\{-i_{ar}\sin(\theta_r) - i_{br}\sin(\theta_r + 2\pi/3) \\ & - i_{cr}\sin(\theta_r - 2\pi/3)\} \times p + \\ & i_{bs}L_{sr}\{-i_{ar}\sin(\theta_r - 2\pi/3) - i_{br}\sin(\theta_r) \\ & - i_{cr}\sin(\theta_r + 2\pi/3)\} \times p + \\ & i_{cs}L_{sr}\{-i_{ar}\sin(\theta_r + 2\pi/3) - i_{br}\sin(\theta_r - 2\pi/3) \\ & - i_{cr}\sin(\theta_r)\} \times p \end{aligned} \quad (9)$$

$$T_e - T_l = J \frac{d\Omega_r}{dt} + f\Omega_r \quad (10)$$

with

$$\Omega_r = 2 \times \pi \times p \times \frac{d\theta_r}{dt} \quad (11)$$

where L_{ms} , L_{mr} , L_{ls} and L_{lr} are magnetizing and leakage stator and rotor inductances and r_{as} , r_{bs} , r_{cs} , r_{ar} , r_{br} and r_{cr} are stator and rotor phase resistances respectively. T_e is the electromagnetic torque, T_l is the load torque, J is the total moment inertia, f is the viscous friction coefficient, p is the number of pole pairs, and θ_r is the rotor angular speed. The estimation of WRIM model parameters, described by relations (1) and (2), is straightforward and can be performed through some basic electrical circuit tests. DC voltage-current experiments at rated working

temperature of WRIM give an initial estimation of both stator phase resistances r_{as} , r_{bs} , and r_{cs} ($r_{as} \approx r_{bs} \approx r_{cs}$) and rotor phase resistances r_{ar} , r_{br} and r_{cr} ($r_{ar} \approx r_{br} \approx r_{cr}$) respectively. The obtained values are commonly good enough for arranging the model and for studying the asymmetry fault in WRIMs. Knowing these previous resistances, the respective stator-related self-inductances i.e. $L_{as} \approx L_{bs} \approx L_{cs} = L_{ms} + L_{ls}$ and mutual inductances i.e. $L_{abs} \approx L_{acs} \approx L_{bcs} = -0.5 \times L_{ms}$ can be obtained according to the relations (12)–(15). An AC voltage source is necessary for providing rated voltages to the stator phase windings as it is depicted in **Figure 1**.

$$L_{as} = \sqrt{\frac{\left(\frac{V_{as}}{I_{as}}\right)^2 - r_{as}^2}{\omega_s^2}} \quad (12)$$

$$L_{cs} \approx L_{bs} \approx L_{as} \quad (13)$$

$$L_{abs} = \frac{V_{bs}}{I_{as}\omega_s} \quad (14)$$

$$L_{bcs} \approx L_{acs} \approx L_{abs} \quad (15)$$

Similarly, the respective rotor-related self-inductances i.e. $L_{ar} \approx L_{br} \approx L_{cr} = L_{mr} + L_{lr}$ and mutual inductances i.e. $L_{abr} \approx L_{acr} \approx L_{bcr} = -0.5 \times L_{mr}$ can be evaluated according to the relations (16)–(19).

$$L_{ar} = \sqrt{\frac{\left(\frac{V_{ar}}{I_{ar}}\right)^2 - r_{ar}^2}{\omega_s^2}} \quad (16)$$

$$L_{cr} \approx L_{br} \approx L_{ar} \quad (17)$$

$$L_{abr} = \frac{V_{br}}{I_{ar}\omega_s} \quad (18)$$

$$L_{bcr} \approx L_{acr} \approx L_{abr} \quad (19)$$

The stator-rotor mutual inductance L_{sr} can be determined using (20).

$$L_{sr} = \frac{V_{ar-max}}{I_{as}\omega_s} \quad (20)$$

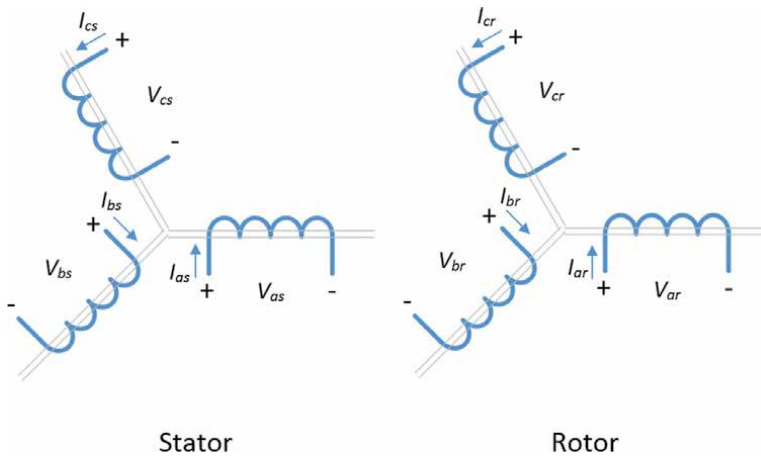


Figure 1. Scheme of experiments for estimation of WRIM 'abc' reference frame model parameters.

where V_{ar-max} is the voltage peak value obtained across one phase of the rotor winding when the stator is supplied by a voltage source and its current is I_{as} .

3. Healthy working condition

For development of FDD techniques, it is crucial to validate experimentally the proposed model of WRIM in healthy working condition at different levels of the load in both time and frequency domains. Accordingly, the parameters of “abc” reference frame model for a WRIM with electrical characteristics, shown in **Table 1**, are estimated using (12)–(20) and listed in **Table 2**. **Figure 2** illustrates the realization of the model in Matlab/Simulink software using trapezoidal integration

Power	90 W
Voltage	380 V
Stator current	0.27 A
Rotor speed	1430 rpm
Pole pairs	2
Torque	0.6 N.m
Rotor inertia	0.001 Kg.m ²

Table 1.
 Electrical and mechanical characteristics of three-phase 90W WRIM.

R_s	79.13 Ω
R_r	3.69 Ω
L_s	2.82 H
L_r	0.23 H
L_{ms}	2.20 H
L_{mr}	0.22 H
L_{sr}	0.67 H

Table 2.
 Estimated parameters of three-phase 90W WRIM “abc” reference frame model.

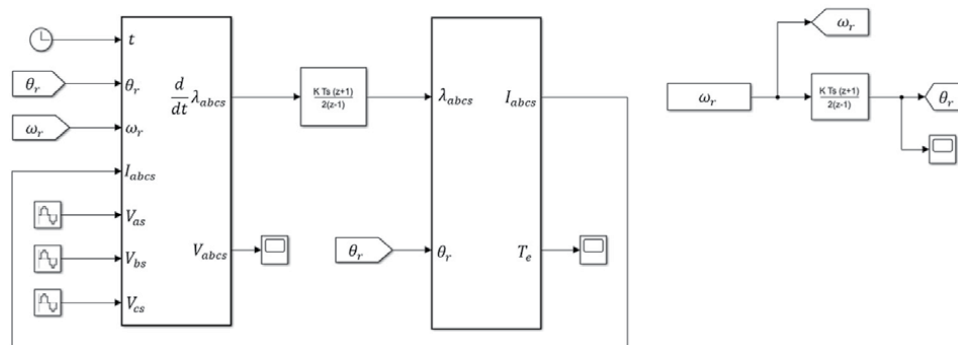


Figure 2.
 Realization of WRIM “abc” reference frame model in Matlab/Simulink.

method. Two discrete-time integrators which are closely linked to the relations (1), (2) and (11) are utilized. The model is initially validated through experiment in time domain at different levels of the load. **Figure 3** depicts the results of numerical simulation and experiment at rated load of WRIM. This simple approach gives a general idea of WRIM modeling to the students who are not familiar with this technique. Besides, it is helpful at this stage to localize the main frequency components in both stator and rotor phase currents spectra. f_s is the main frequency component in the stator phase current spectrum whereas f_{Ir} is the main frequency component in the rotor phase current spectrum.

$$f_{Ir} = f_s - p \frac{\Omega_r}{60} \quad (21)$$

where p is the pole pairs and Ω_r is the rotor mechanical speed. The stator and rotor currents spectra of numerical simulation and experiment at rated slip $s_r = 0.047$ are shown in **Figure 4**. The rotor and stator asymmetries can be performed simply by including an additional series resistance in one of the rotor and stator phases. This technique is the simplest way to familiarize students with fault detection methods in WRIMs which will be highlighted in next sections.

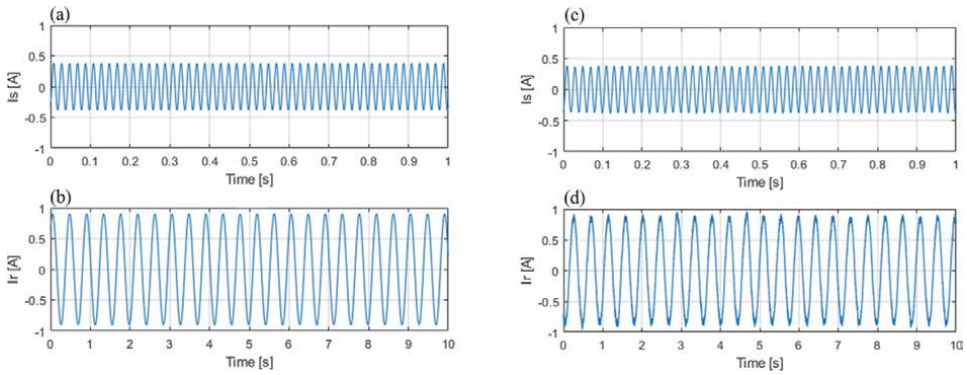


Figure 3. Healthy condition stator and rotor phase currents of WRIM in time domain (a), (b) numerical simulation (c), (d) experiment.

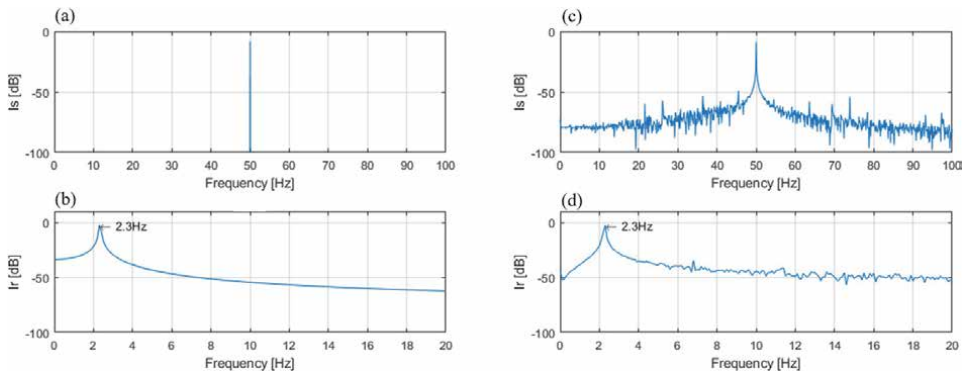


Figure 4. Healthy condition stator and rotor phase currents of WRIM in frequency domain (a), (b) numerical simulation (c), (d) experiment.

4. RAF detection

It is well known that any deviation from the normal operation of WRIM, resulted from an internal or external anomalies, may induce fault signatures in the electrical variables such as stator and rotor currents. It was illustrated that the stator current is directly affected by the RAF whereas the SAF has a direct influence on the rotor current [5, 11]. The fault diagnosis is commonly carried out by computing the stator/rotor current Fourier transform to locate fault frequency components in the spectrum. An addition resistance $R_{RAF} = 1\Omega$ is included in one of the rotor phases to create the RAF. **Figure 5** illustrates the numerical simulation and experimental results of the stator and rotor phase currents in time domain. As it can be observed, it is quite difficult to detect the RAF through time domain analysis, particularly for small values of R_{RAF} . If the rotor speed of WRIM is considered constant, the following unique frequency component will appear in the stator phase current spectrum [12]:

$$f_{RAF} = (1 - 2s)f_s \quad (22)$$

where s is the slip value. The RAF frequency-related component is well localized in both numerical simulation and experiment spectra of the stator phase current at rated slip value of WRIM (**Figure 6**). Furthermore, the fact that the stator phase current is directly affected by the RAF is well depicted in this last figure.

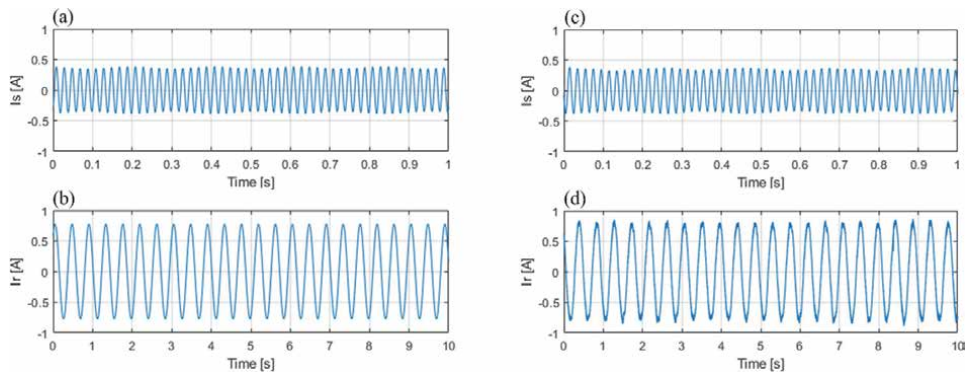


Figure 5. RAF condition stator and rotor phase currents of WRIM in time domain (a), (b) numerical simulation (c), (d) experiment.

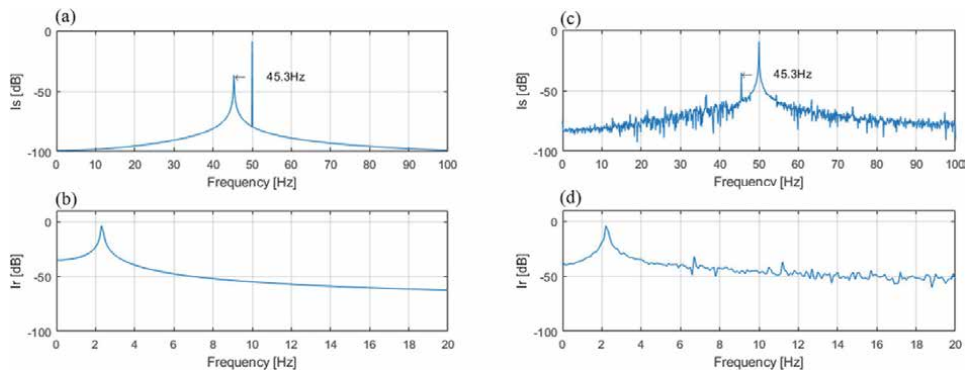


Figure 6. RAF condition stator and rotor phase currents of WRIM in frequency domain (a), (b) numerical simulation (c), (d) experiment.

5. SAF detection

The frequency components in the rotor phase currents due to the SAF can be obtained as [13]:

$$f_{SAF,k'} = \left\{ \frac{k'}{p}(1-s) \pm 1 \right\} f_s \quad (23)$$

where $k' = 1, 2, 3, \dots$. Taking only the fundamental frequency component into account with $\frac{k'}{p} = 1$, the relation (23) can be written as

$$f_{SAF} = (2-s)f_s \quad (24)$$

An additional series resistance $R_{SAF} = 10\Omega$ is included in one of the stator phases to create the SAF. **Figure 7** illustrates the numerical simulation and experimental results of the stator and rotor phase currents at rated slip value of WRIM in time domain.

The SAF frequency-related component is well localized in both numerical simulation and experiment spectra of the rotor phase current at rated load of WRIM (**Figure 8**). Besides, it is well illustrated in **Figure 8**, where the rotor phase current is directly affected by the SAF [11].

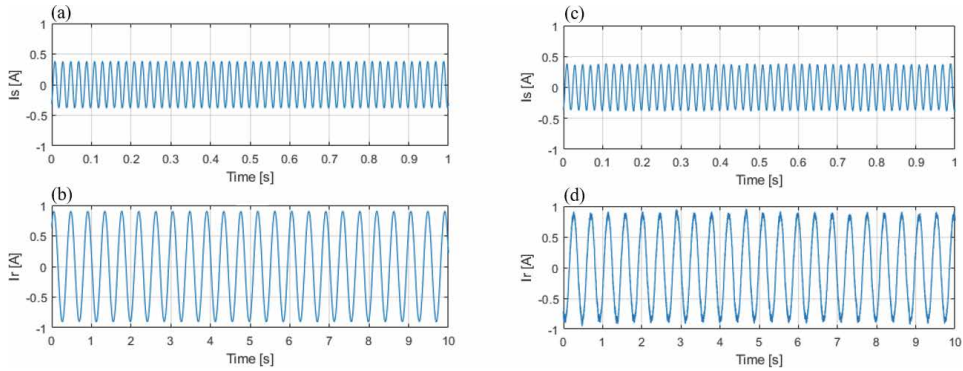


Figure 7. SAF condition stator and rotor phase currents of WRIM in time domain (a), (b) numerical simulation (c), (d) experiment.

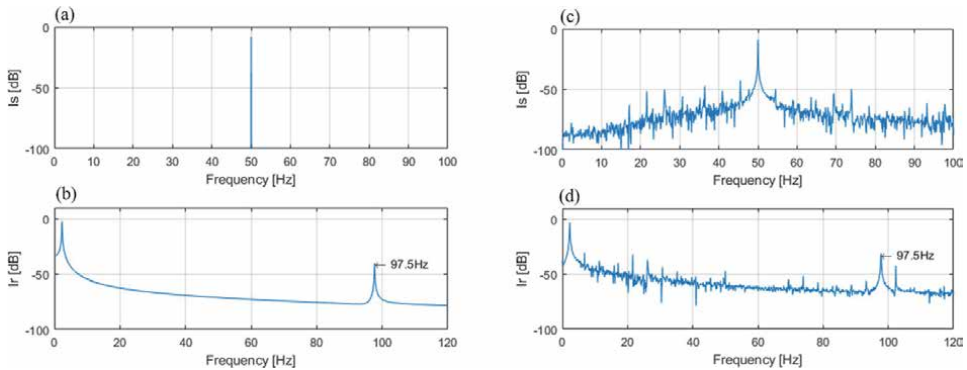


Figure 8. SAF condition stator and rotor phase currents of WRIM in frequency domain (a), (b) numerical simulation (c), (d) experiment.

6. Real-time RAF and SAF detections

The utilization of SPTs is the crucial stage of the RAF and the SAF detections in both steady-state and transient working conditions of WRIM. The developed methods can be classified in time, frequency and time-frequency/time-scale domains [2]. A brief review of the recent SPTs was mentioned in this topic of research [5]. Up to now, various experimental setups have been designed to evaluate the effectiveness of each SPT. They are mainly defined based upon the rated power of the installed electrical machine in the system. Furthermore, fault detection algorithms are commonly evaluated offline, whereas the new trends are mainly relied on the real-time FDD of electrical machines [6]. The concept of H-i-L is perfectly matched with such a development which is rarely studied [3]. In this regard, a real-time data acquisition system (CompactRIO data acquisition system) is used as a H-i-L with a high performance multi-core real-time platform in order to analyze the performance of different kinds of SPTs in practical conditions (Figure 9).

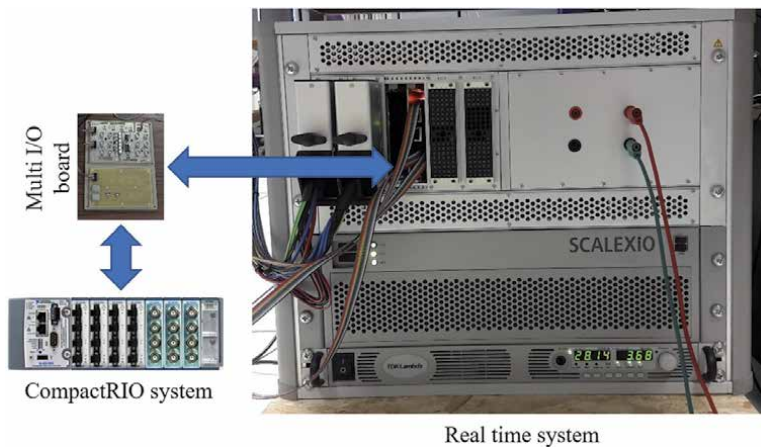


Figure 9.
Configuration of H-i-L test bench.

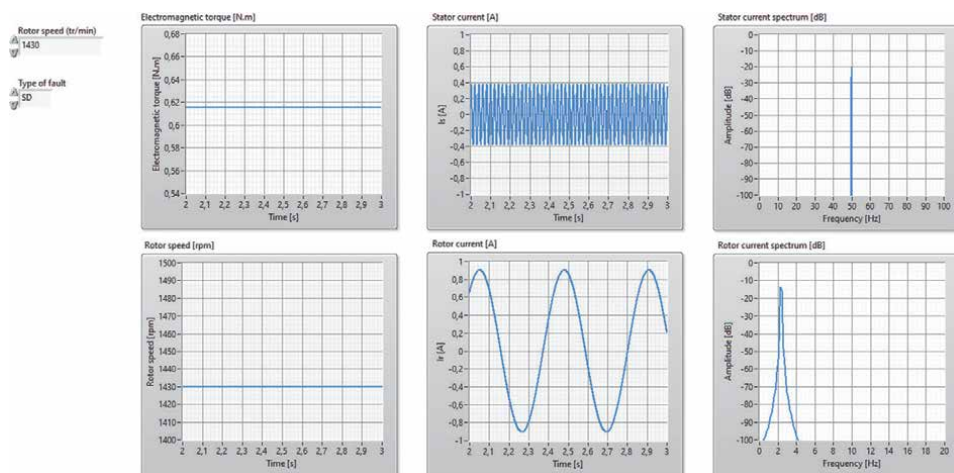


Figure 10.
Healthy condition H-i-L experimental results at rated load of WRIM.

This configuration is particularly attractive as it is totally independent of the type of the under study electrical machine and can be extended to any kind of fault for which an adapted model is well designed. Furthermore, there are more facilities to access the signatures which are commonly difficult to obtain without including high performance sensors in an experimental traditional test bench. The model of WRIM in “*abc*” reference frame, shown in **Figure 2**, is implemented in the real-time system with sampling time $T_s = 10^{-4}$. The stator and rotor current signals, provided by multi I/O board of real-time system, are measured and analyzed by the CompactRIO data acquisition system at 5 kHz sampling frequency for 10s to detect the RAF and the SAF in steady-state working condition of WRIM.

The results of the analysis are illustrated in **Figures 10–12** for the healthy, the RAF and the SAF conditions respectively. The stator and the rotor currents in healthy condition at rated load of WRIM in both time and frequency domains are shown in **Figure 10**. As it would be expected, the main frequency components which are well identified in the spectra are f_s and f_r , respectively. The fault-related

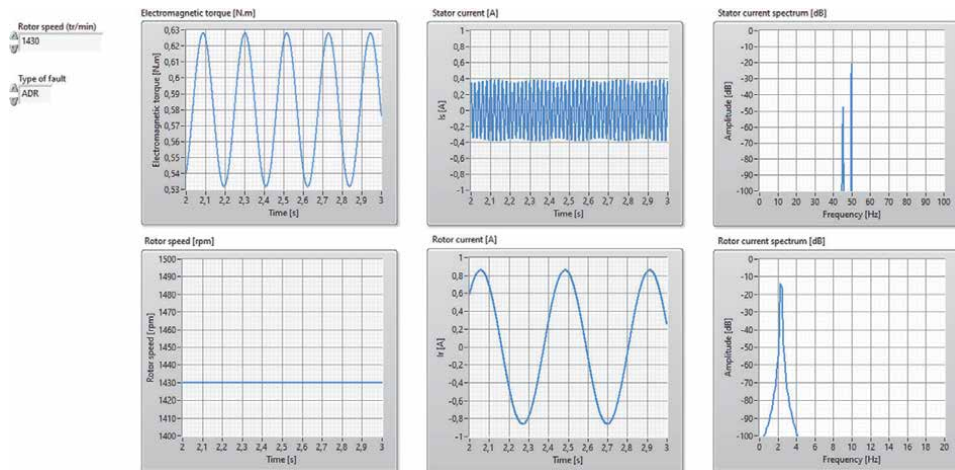


Figure 11.
RAF condition H-i-L experimental results at rated load of WRIM.

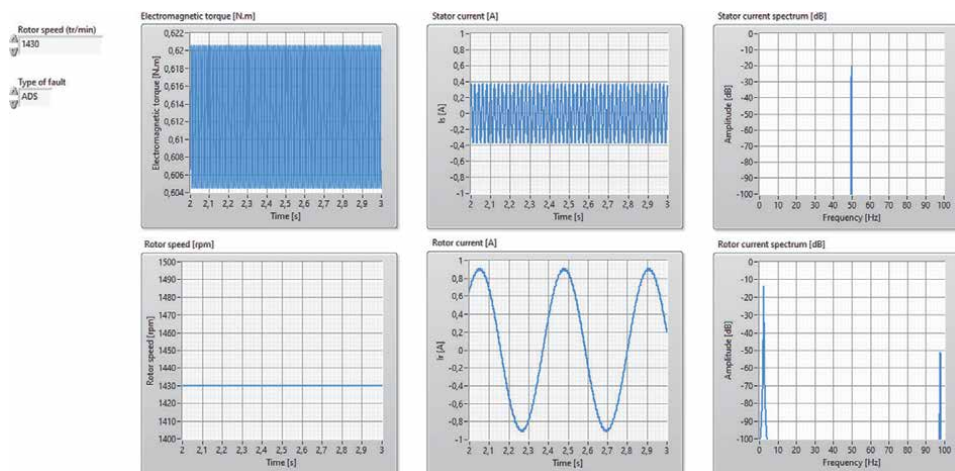


Figure 12.
SAF condition H-i-L experimental results at rated load of WRIM.

frequency component $(1 - 2s_r)f_s$ ($s_r = 0.047$) is detected in the stator phase current spectrum at rated rotor speed of WRIM (**Figure 11**). The SAF reveals $(2 - s_r)f_s$ frequency component in the rotor phase current spectrum as it is shown in **Figure 12**. Besides, the electromagnetic torque is a good indicator of both the RAF and the SAF and can be used as an alternative signature for FDD design (**Figures 11 and 12**).

7. Conclusion

This chapter presents for the first time the concept of H-i-L for fault diagnosis of WRIMs as a part of fault diagnosis of electrical machines course for master's degree students at University of Picardie "Jules Verne". The parameter of WRIM model in "abc" reference frame is estimated and validated through experiment at different levels of the load. The developed model is then implemented in a real-time system which is in the loop with a CompactRIO data acquisition platform. This configuration allows to evaluate the SPTs for real-time FDD design in all working conditions of WRIMs. Furthermore, this concept can be extended to condition monitoring of any complex electromechanical system at development stage design.

Abbreviations


RAF	Rotor asymmetry fault
SAF	Stator asymmetry fault
WRIM	Wound rotor induction machine
IM	Induction machine
DFIG	Doubly fed induction generator
FDD	Fault detection and diagnosis
CBM	Condition based maintenance
SPT	Signal processing tool
FEM	Finite element method
S-i-L	Software-in-the-loop
H-i-L	Hardware-in-the-loop

Author details

Shahin Hedayati Kia
MIS Lab. (EA4290), University of Picardie "Jules Verne", Amiens, France

*Address all correspondence to: shdkia@u-picardie.fr

IntechOpen

© 2021 The Author(s). Licensee IntechOpen. This chapter is distributed under the terms of the Creative Commons Attribution License (<http://creativecommons.org/licenses/by/3.0>), which permits unrestricted use, distribution, and reproduction in any medium, provided the original work is properly cited. 

References

- [1] Randall RB. *Vibration-Based Condition Monitoring: Industrial, Aerospace and Automotive Applications*. Wiley; 2011.
- [2] Frosini L. Monitoring and diagnostics of electrical machines and drives: A state of the art. In: 2019 IEEE workshop on electrical machines design, Control and Diagnosis (WEMDCD). vol. 1; 2019. p. 169–176.
- [3] Sapena-Bano A, Riera-Guasp M, Martinez-Roman J, Pineda-Sanchez M, Puche-Panadero R, Perez-Cruz J. FEM-analytical hybrid model for real time simulation of IMs under static eccentricity fault. In: 2019 IEEE 12th International Symposium on Diagnostics for Electrical Machines, Power Electronics and Drives (SDEMPED); 2019. p. 108–114.
- [4] Isermann R. Fault diagnosis systems an introduction from fault detection to fault tolerance. SERBIULA (sistema Librum 20). 2006 01.
- [5] Kia SH. Monitoring of wound rotor induction machines by means of discrete wavelet transform. *Electric Power Components and Systems*. 2018; 46(19–20):2021–2035.
- [6] Monmasson E, Idkhajine L, Cirstea MN, Bahri I, Tisan A, Naouar MW. FPGAs in industrial control applications. *IEEE Transactions on Industrial Informatics*. 2011;7(2): 224–243.
- [7] Gómez-de-Gabriel JM, Mandow A, Fernández-Lozano J, García-Cerezo A. Mobile robot lab project to introduce engineering students to fault diagnosis in mechatronic systems. *IEEE Transactions on Education*. 2015 Aug;58(3):187–193.
- [8] Record P. Teaching the art of fault diagnosis in electronics by a virtual learning environment. *IEEE Transactions on Education*. 2005 Aug; 48(3):375–381.
- [9] Pagiatakis G, Dritsas L, Chatzarakis G, Todorov G, Stoev B. Introducing concepts and methodologies of fault detection into electrical engineering education: The induction machine example. In: 2017 IEEE Global Engineering Education Conference (EDUCON); 2017. p. 381–388.
- [10] Krause P, Wasynczuk O, Sudhoff SD, Pekarek S. In: *Induction motor drives*. IEEE; 2013. Available from: <https://ieeexplore.ieee.org/document/6739387>.
- [11] Penman J, Sedding HG, Lloyd BA, Fink WT. Detection and location of interturn short circuits in the stator windings of operating motors. *IEEE Transactions on Energy Conversion*. 1994;9(4):652–658.
- [12] Filippetti F, Franceschini G, Tassoni C, Vas P. AI techniques in induction machines diagnosis including the speed ripple effect. *IEEE Transactions on Industry Applications*. 1998;34(1):98–108.
- [13] Shah D, Nandi S, Neti P. Stator inter-turn fault detection of doubly-fed induction generators using rotor current and search coil voltage signature analysis. In: 2007 IEEE Industry Applications Annual Meeting; 2007. p. 1948–1953.

Prospects for Increasing the Dynamic Efficiency of Asynchronous Double-Feed Machines and Wind Power Generators Using Structural Methods and Solutions

*Vladimir L. Kodkin, Alexandr S. Anikin
and Alexandr A. Baldenkov*

Abstract

The chapter proposes to consider the problems of control of asynchronous machines with dual power supply, as a nonlinear structure, the transfer functions of which depend on the frequency of the stator voltage and the relative slip. The authors cite the results of research confirming the high efficiency of control of asynchronous electric motors, using cross-dynamic connections on the developed torque or a signal close to it (active component of the motor stator current). The proposed correction operates in a wide range of changes in the rotation and sliding speeds of the asynchronous electric generator. This is especially important for wind turbines that need to remain efficient at different speeds. As a justification, the results of experiments, modeling and industrial application of control algorithms with positive torque coupling are presented. Research results suggest that such algorithms will improve the efficiency of wind power by 5–10%.

Keywords: asynchronous called double-feed machines (DFM), frequency regulation, dynamic positive feedbacks, active stator current, rotor current, signal spectrum, parrying of step and harmonic moments

1. Introduction

The squirrel cage induction motors (SCIM), widely used in industry and power engineering, are distinguished primarily by their high reliability and low cost. Asynchronous electric drive (AED) of mechanisms in which they are used, as a rule, do not require a significant range of speed and torque control, high control accuracy and fast transients. Even in drives with rather expensive frequency and voltage converters (FC), it is not easy to solve the problems of SCIM control. Research of control systems of such drives continues at the present time.

At the same time, in a number of units, wound rotor induction motors (WRIM) are widely used. The design of these motors allows connecting additional active resistances to the rotor and adjusting the ratio of active and reactive power. In this case, the stator and rotor currents, the rotation speed and the developed torque change at a constant rotation speed of the magnetic field. At the same time, the design of the engine becomes somewhat more complicated, and accordingly, its cost increases (slightly). It was this ability to regulate speed and torque that made WRIM the main electric motors in a number of mechanisms in the 60s and 70s before the widespread introduction of available FC. In a number of countries (for example, in Russia and the CIS), such drives are still used in hoisting and transport mechanisms. At the same time, the problems with the dynamics of the drive remain, in general, the same as for the SCIM.

The ability to adjust the WRIM operating mode from the rotor side not only in motor, but also in generator modes ensured the use of WRIM in the power industry, in those generating sets in which the rotation speed of driving machines cannot be sufficiently stable. At the same time, asynchronous machines with a phase rotor were called double-feed machines (DFM). Since the water flow rate in hydropower generators cannot be constant and it cannot be controlled by mechanical means with an accuracy of more than 1%, a voltage source is included in the rotor of the machine, which corrects the voltage parameters on the stator of the machine connected to the power grid.

In recent years, asynchronous dual-feed machines have become widely used in wind energy, which over the past few decades has emerged in a number of countries in a separate energy sector that successfully competes with traditional energy sources. DFM in wind turbines allow to generate electricity with the required parameters at different wind speeds, supplying energy directly to the network through the stator windings (Figure 1) [1].

At the same time, the problems with the regulation of the DFM, as an asynchronous electric machine, are fully manifested. They play a significant role in reducing the efficiency of wind turbines. A whole range of problems should be noted.

Problem analysis. The generally accepted mathematics for describing processes in AC electric machines plays a significant role. When describing the work of DFM [1, 2], vector equations and dependencies, traditional for AC machines, are used with a large number of assumptions and simplifications. One of the main ones is the neglect of the components of higher harmonics in the rotor and stator currents and voltages in the DFM. The DFM equations, like the equations describing all asynchronous and synchronous motors, do not take into account changes in the

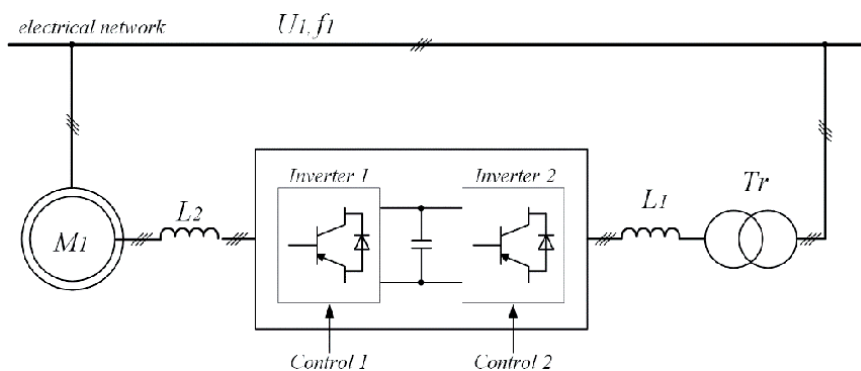


Figure 1. Connection diagram DFM.

frequency of voltages and currents at all. Naturally, these vector equations take into account transient processes in a very simplified way [2]:

Consider an example of such a description [1]:

$$\begin{cases} U_1 = R_1 i_1 + \frac{d\Psi_1}{dt} + j\omega_k \Psi_1; \\ U_2 = R_2 i_2 + \frac{d\Psi_2}{dt} + j(\omega_k - p\omega) \Psi_2; \\ \Psi_1 = L_1 i_1 + L_m i_2; \\ \Psi_2 = L_2 i_2 + L_m i_1; \end{cases} \quad (1)$$

where U_1, U_2 – stator and rotor voltage vectors; Ψ_1, Ψ_2, i_1, i_2 – vectors of flux linkages of stator and rotor currents; R_1, L_1, R_2, L_2 – active resistances and inductance of stator and rotor; L_m – main inductance of the magnetizing circuit; ω_k – angular velocity of rotation of the coordinate system; ω – angular speed of rotation of the rotor; p – number of pole pairs of the machine.

Eq. (1) are obtained from the equations of an alternating current electric machine under the assumption that the processes of changing currents and voltages in the DFM are sinusoidal signals of constant frequency. If we assume the change in this frequency, which occurs when regulating the speed and torque of the DFM, the original equations become so complicated that it will be impossible to analyze them and select an effective correction based on them.

These methods of describing asynchronous electric drives with vector equations lead to a number of limitations in control devices. For example, an increase in the stator magnetic flux (ratio U/f) leads to a violation of stability and an increase in stator currents at low loads [3–6], therefore control algorithms in many inverters limit this parameter, reducing the possibility of accelerating transient processes.

Another problem is the dependence of the drive dynamics on the stator voltage frequency [7–10]. Vector equations describing asynchronous electric drives do not allow to reliably describe these processes and suggest effective correction.

Figure 2 shows the results of experiments with an asynchronous drive with vector control, closed by a speed signal with surges of a torque load. The processes of

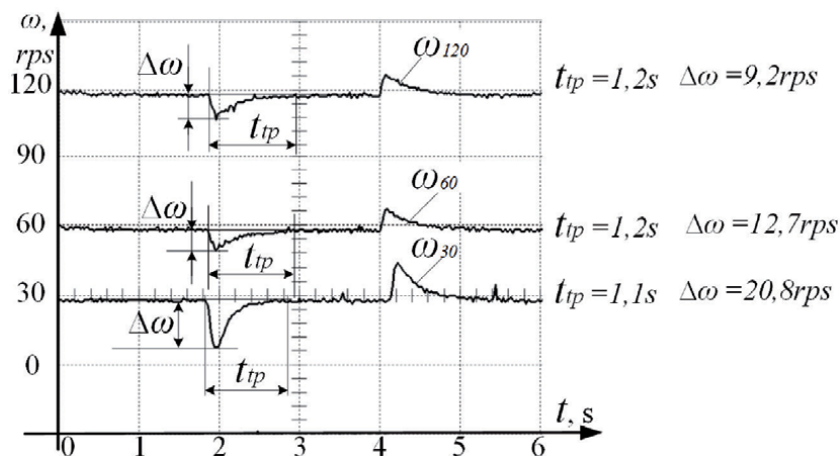


Figure 2. Diagrams of the speed change when parrying a stepped torque at different speeds of rotation in a drive with vector control.

parrying a torque load are different at different speeds of rotation and frequencies of stator voltage and are strongly “tightened”. At even higher speeds, the stability of the drive [7–9, 11, 12] is impaired.

It should be noted that the traditional means and methods of regulation of asynchronous electric drives with frequency control (PID speed or torque controllers) with vector control or direct torque control work very poorly precisely when parrying “step” or harmonic torque loads. This is shown in articles [7–10, 13].

In DFM wind turbines, the wind works exactly as a moment load. In this case, the wind parameters are not stationary and difficult to predict.

There are many works devoted to the study of the parameters of wind flows, one of the time dependences is shown in **Figure 3**. As a rule, several ranges of speed variation can be distinguished in the wind speed - slow and faster.

The frequency of rapid variations in wind speed is from too high for its effective “tracking” by powerful and large-sized electric drives of wind turbines [14–17]. Electric generators and wind turbines in general have significant inertia – tens and hundreds of seconds due to their very large dimensions.

The control systems of these installations should work as follows. DFM, as a generator, must convert mechanical wind energy, determined by the average wind speed, into electrical energy. And, as an electric drive, it must correct and smooth out wind gusts so that they do not “distort” the frequency and amplitude of the stator voltage. To solve this problem in the DFM must be the inverter connected to the rotor circuit. It can adjust the frequency and amplitude of the stator voltage precisely. At the same time, a change in the voltage in the rotor has a complex effect on the DFM, causing “its” transient processes.

In DFM, most often, rather traditional algorithms for asynchronous electric drives are used to optimize stationary modes - depending on the wind speed, the structure of the drive changes - the torque or speed of the motor is controlled by loops with a PID controller. At the same time, during the change in the wind speed, the restoration of the parameters of the DFM operation mode - the torque, the speed of rotation and, accordingly, the frequency of the stator voltage - occurs rather slowly, and in order not to violate the compliance with the requirements of the parameters of the stator voltage – frequency and amplitude, most often,

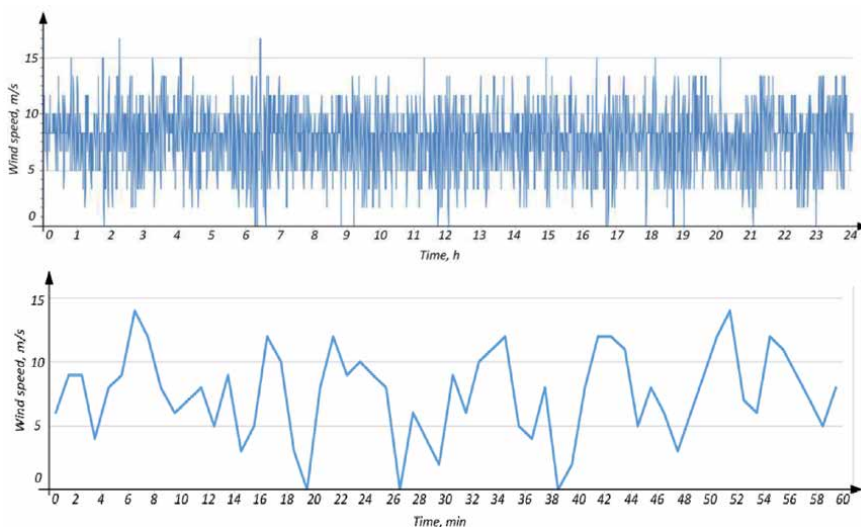


Figure 3.
Example of a graph of the change in wind speed.

energy transfer is blocked and the entire wind turbine is stopped. That is, the use of optimization methods is limited to modes of uniform power generation, i.e. they can be used only when the wind turbine is in a stationary state, with small and slow changes in the parameters of wind flows. In case of transient processes or in emergency situations, the methods are not applicable.

The reason that DFMs are disconnected from the grid during transient modes is the inability of the regulation system to track these changes in wind speed with minimal transients. The shutdown and protection devices receive considerable attention from developers and researchers. At the same time, the purpose of the protection devices is to preserve the operability of the equipment with “non-mode” parameters of the wind and power grid, and to reduce the time of inoperability of wind power units. But in all these devices, little attention is paid to the dynamics of installations in operating states. The modes and settings of the regulators remain standard, which means that they are quite ineffective in terms of dynamics. All this also reduces the efficiency of wind turbines to critically low values. At the same time, the “dynamic potential” of asynchronous electric drives is far from being exhausted and is not used in most drives because most often it is not required. But not in the case of wind turbines.

The authors carried out research on the dynamics of asynchronous electric drives with frequency control, which are of undoubted interest for wind power. The research consisted of the development of theoretical provisions, bench experiments, simulation and application of industrial units in electric drives.

2. Theoretical provisions

Vector equations were replaced by continuous ones in a certain area of the multidimensional space formed by variable coordinates of the electric drive - rotation speed and mechanical moment and independent functions - stator voltage frequency and relative slip. As a result, a nonlinear transfer function was obtained that connects the developed mechanical torque and absolute slip - the difference between the stator voltage frequency and the engine speed. The formula for this function includes, as variables, the frequency of the stator voltage and the relative slip. The formula can be called the nonlinear transfer function or the dynamic Kloss formula. In articles [18–26] the conclusion of the proposed nonlinear transfer function is given in sufficient detail, the result is as follows:

$$W(p) = \frac{2M_k(T_2'p + 1)S_k}{\omega_1[(1 + T_2'p)^2 S_k^2 + \beta^2]} \quad (2)$$

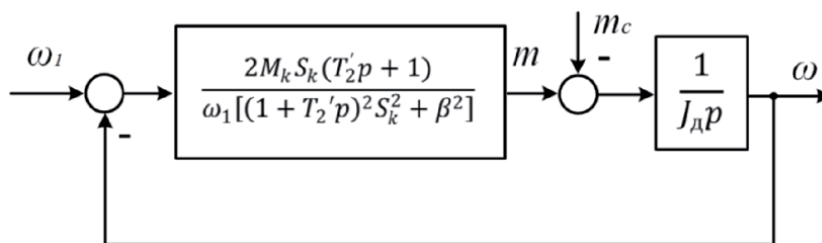


Figure 4.
 Block diagram of the working section of the mechanical characteristics of an alternating current machine.

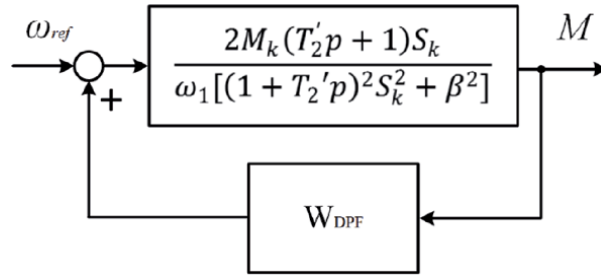


Figure 5.
Block diagram of the corrected electric drive.

where, ω_1 is the stator voltage frequency, β is the relative slip, depending on the drive load.

This transfer function corresponds to the block diagram shown in **Figure 4**.

In works [18–27] it is shown how it is possible to linearize the specified transfer function, that is, to exclude the dependence of the transfer function and the dynamics of the asynchronous drive on the frequency of the stator voltage and slip by positive feedback on the developed torque. The structural diagram will take the form (**Figure 5**).

The transfer function of the correcting link, which is necessary in positive feedback to maintain the stability of the drive, is as follows:

$$W_{DPF} = \frac{\omega_1 \beta^2}{2M_k S_k (T_2' p + 1)} \quad (3)$$

Equivalent transfer function of the drive with this connection will take the form:

$$W_{eqv} = \frac{2M_k S_k (T_2' p + 1)}{\omega_1 [(1 + T_2' p)^2 S_k^2]} = \frac{2M_k}{\omega_1 S_k (1 + T_2' p)} \quad (4)$$

The resulting transfer function of an asynchronous electric motor with parameters depending on the frequency of the stator voltage and slip is an “incorrect” expression from the point of view of the exact mathematics of functional transformations (Laplace transforms). But Eqs. (2) and (3) can describe the dynamics of transient processes with small frequency changes and slip (which change little the value of $W(p)$) with significantly smaller errors than vector equations, which are accurate not only at a constant frequency, but also with the mandatory sinusoidality of currents and voltages in the stator and rotor of an induction motor [11, 15, 23–25, 28–30].

The method using nonlinear transfer functions turns out to be more accurate than the generally accepted apparatus of vector equations. Especially important for the DFM wind turbine is the fact that the efficiency of the choice of correction is also significantly higher for the processes of parrying moment disturbances in asynchronous electric drives with frequency control [21, 22, 27, 28, 31–33].

Thus, the proposed positive dynamic connection by the torque of the engine or its analogue significantly reduces the time of the transient parrying processes and their maximum values. Experiments investigating the response of the drive to load surges with various methods of WRIM control have fully confirmed this.

This made it possible to formulate a hypothesis that the identification of an induction motor with a frequency converter by a nonlinear transfer function is more accurate than vector equations, which is confirmed by the choice of a more effective correction selected for this transfer function.

It should be noted that experiments with parrying the moment disturbance at a constant frequency of the stator voltage with minimal transients in the speed of rotation of the engine and in the torque is the most desirable process for the DFM of wind turbines.

In this case, the corrected drive will ensure the “bringing” of all variable coordinates of the DFM to the required “zone, where the rotor frequency converter will equalize the frequency of the stator voltage to the specified value with high accuracy.

In asynchronous electric drives using mass-produced frequency converters, it is quite problematic to introduce a positive torque connection. As experiments have shown [8–10, 18–27], it can be replaced by a connection according to the active component of the stator current, which is measured by almost all known frequency converters widely used in industry.

In powerful and not cheap drives of wind power systems, it is advisable to install sensors for direct measurement of the mechanical moment and speed sensors, and magnetic flux sensors in the DFM. In this case, the complexity and uniqueness of each high-power wind turbine allows the application of solutions with a high cost, but at the same time with high efficiency.

As mentioned above, analytical expressions describing asynchronous electric drives have significant errors. Therefore, decisive importance in assessing the correctness and effectiveness should be given to experimental research.

3. Bench experiments

The test bench (**Figure 6**), On which the research was carried out, contains - a load asynchronous squirrel-cage motor (M1) and a working electric motor with a phase rotor (M2) operating on one shaft, frequency converters (FC1, FC2) that control motors, rotor current sensors of the working electric motor, and a common shaft speed sensor (BR1) and a periodic reference signal generator (SG1).

The order of experiments is formulated according to the transfer function of the electric drive (2)-(4).

The signal supplied to the input of the frequency converter U2 of the working WRIM drives the drive to a certain speed of rotation (and the corresponding frequency of the stator voltage). This determines the parameters of the transfer function, depending on the frequency of the stator voltage.

The signal generator SG sends a periodic signal of a certain frequency to the input of the frequency converter U1 of the load SCIM, which creates a load torque with an amplitude of 10% of the nominal value, which determines the range of variation of the transfer function parameter, which depends on slip – formula (2). The same input receives a step signal at the level of 100% of the nominal mechanical torque.

The purpose of the experiment is to provide evidence of the effectiveness of the drive control method. The control system of the drive must ensure maximum parrying of any moment disturbance, that is, the better the drive maintains the rotation speed (the less it deviates from the set speed), the more efficient its control.

Various operating modes of electric drives were investigated.

For studies of the DFM of wind power plants, the reactions of control systems to moment loads are of greatest interest.

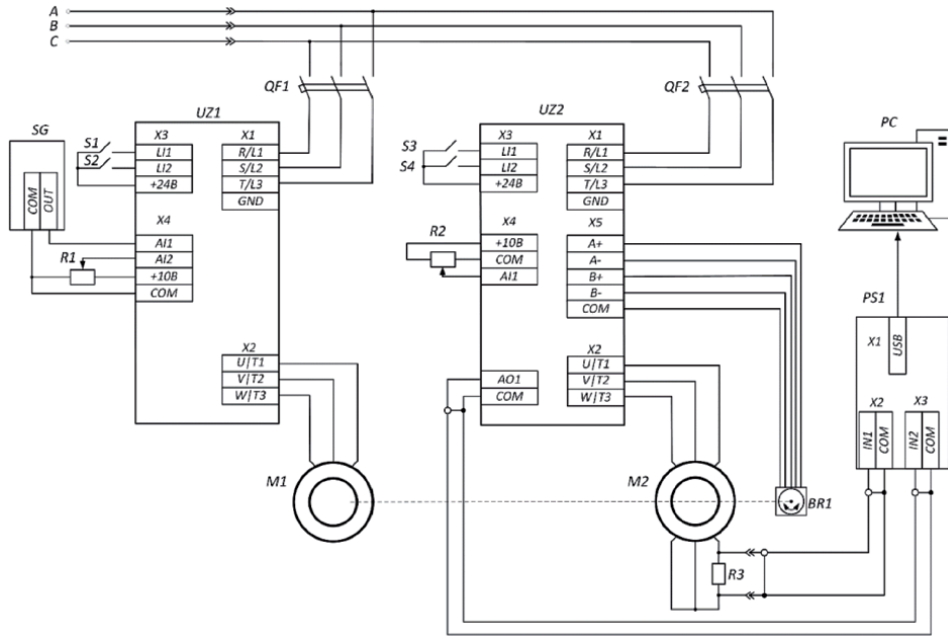


Figure 6.
Electrical circuit of the experimental stand.

Figure 7 shows the diagrams of changes in the speed of rotation of the engine with a “step” load with various control methods - open scalar control, vector control with speed feedback, and in a drive with torque (current) coupling. Transient time and maximum speed deviation for stepped load torque – minimum in an electric drive with DPF.

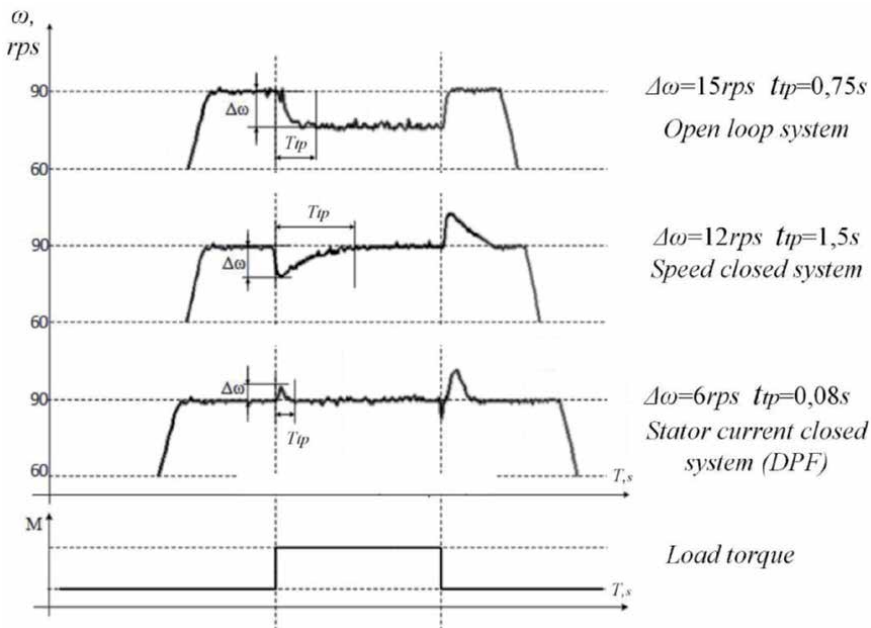


Figure 7.
Drive response to “step” load surge

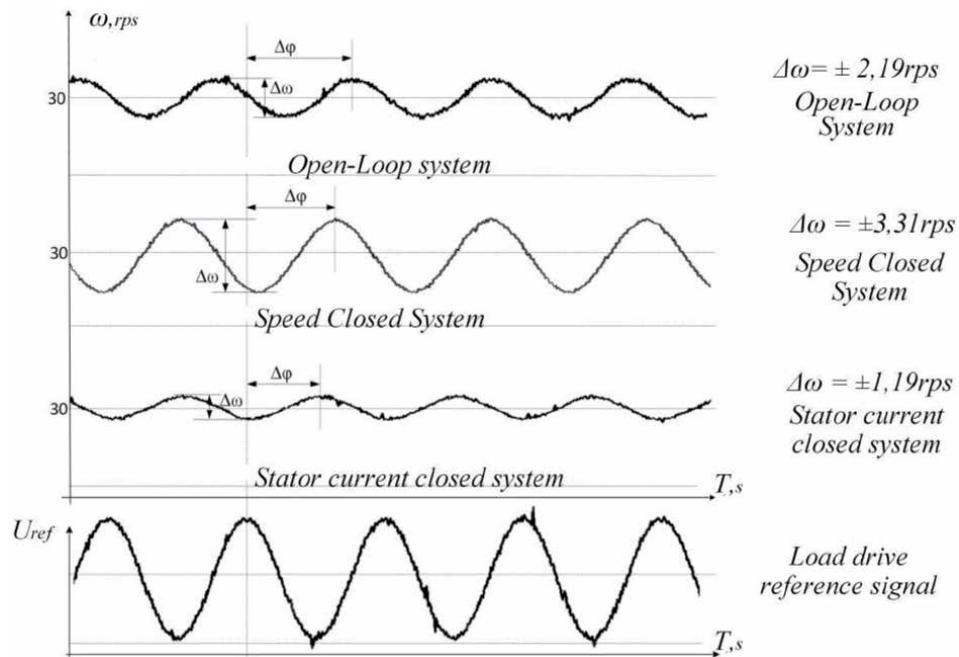


Figure 8.
 Drive response to harmonically varying load torque.

In **Figure 8** diagrams obtained in the course of experiments with variable load - harmonic change in torque with a frequency of 1 Hz, – in the example, the amplitude of change is 10% of the nominal torque value.

The amplitude of deviations from the set speed for a periodic disturbing torque with a frequency of 1 Hz in an electric drive with DPF is also the smallest.

Advantages of a drive with positive torque coupling (or its close analogue - active stator current) are obvious.

4. Analysis of the efficiency of asynchronous drives in the rotor current spectrum

In a number of modes, according to the speed diagrams, it is rather difficult to assess the degree of advantage of this or that control method for asynchronous electric drives.

A technique for assessing the dynamics of the drive by the frequency of the rotor current is proposed and developed, which is of undoubted interest for DFM. Experiments have shown that this estimate is much more convincing than the analysis of velocity diagrams.

Since the frequency of the rotor current is precisely determined by the slip in the motor, the rotor current spectra characterize the control efficiency of the drive. This technique is discussed in detail in [18–21, 23–27, 34].

Figures 9–11 shows diagrams and spectra of the rotor currents with load surges with different control methods: DPF drive (**Figure 9**), open-loop scalar drive (**Figure 10**), closed loop scalar drive (**Figure 11**). Particular attention should be paid to the nature of the stator current when using a dynamic positive connection for the motor torque (for the active stator current).

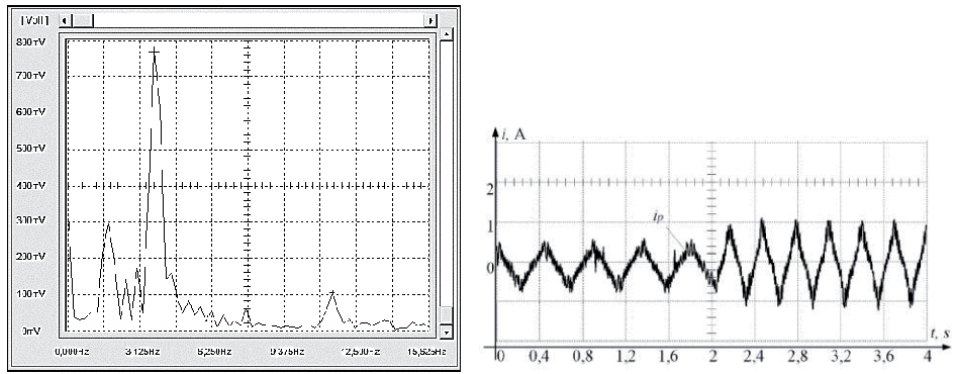


Figure 9.
Diagram and spectrum of the rotor current for scalar control with positive feedback.

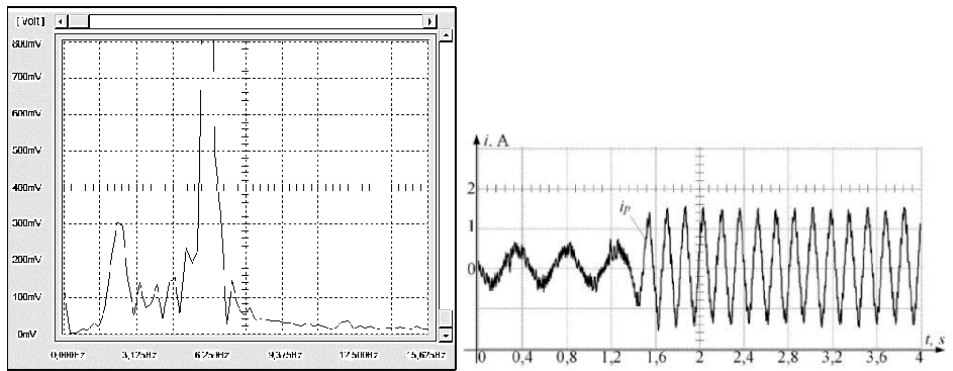


Figure 10.
Diagram and spectrum of the rotor current with vector control.

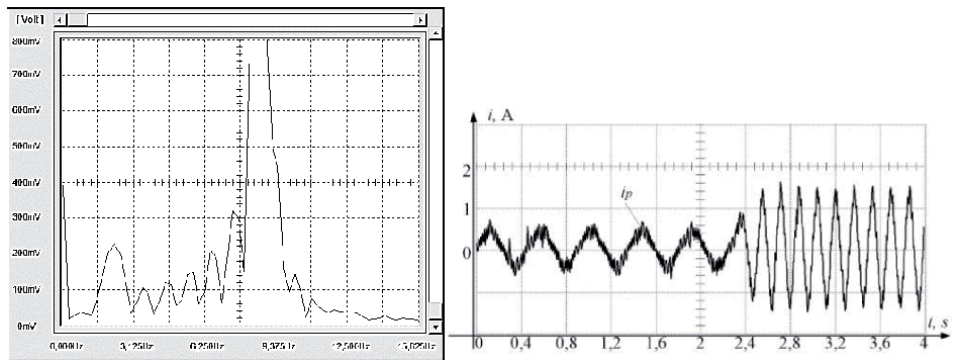


Figure 11.
Diagram and spectrum of the rotor current for scalar control.

Experiments with load surges have unambiguously shown a significant advantage of this scheme.

Basic frequencies of the rotor current.

- no load – 1,7 Hz in an asynchronous drive with scalar control,
- 2,1 Hz in an asynchronous drive with a vector control and.

- -1,7 Hz in an asynchronous drive with a positive torque coupling.
- both with load- 4,75 Hz in an asynchronous drive with scalar control,
- 8,75 Hz in an asynchronous drive with a vector control and.
- -3,5 Hz in an asynchronous drive with a positive torque coupling.

That is, an electric drive with a dynamic positive connection in terms of the torque developed by the drive (or an analogue of this signal - the active component of the stator current) requires significantly less slip to create the required torque than in drives with scalar or vector, speed-closed controls. (Position P1).

Detailed drive experiments with this feedback have shown the nature of this efficiency. Since the transfer function (2) depends on the frequency of the stator voltage, the experiments were carried out at several different speeds of rotation of the engine and, accordingly, these frequencies.

The experiments were carried out at five operating speeds (31,42 rps, 62,83 rps, 94,25 rps, 125,67 rps, 157,08 rps) which corresponds to the frequencies of the stator voltage - 10 Hz, 20 Hz, 30 Hz, 40 Hz, 50 Hz. Diagrams of processes in speed, rotor currents and their spectra are shown in **Figures 12–14**. In all cases, under load, rotor current distortions and the third harmonic are observed, compared with the main one in the rotor current spectra.

It is known from the theory of automatic control that odd harmonics in periodic signals of a closed automatic control system (ACS) arise in the presence of symmetric static nonlinearities. In AED, such a static nonlinearity is the magnetization curve of the stator and rotor. This nonlinearity is characterized by saturation regions in which an increase in the magnetic field strength proportional to the current does not lead to a significant increase in magnetic induction.

This testifies to the saturation of the magnetic structure of the motor, which occurs only under load and ensures high efficiency of torque generation under load with a smaller mismatch between the synchronous speed and the rotor speed. It can

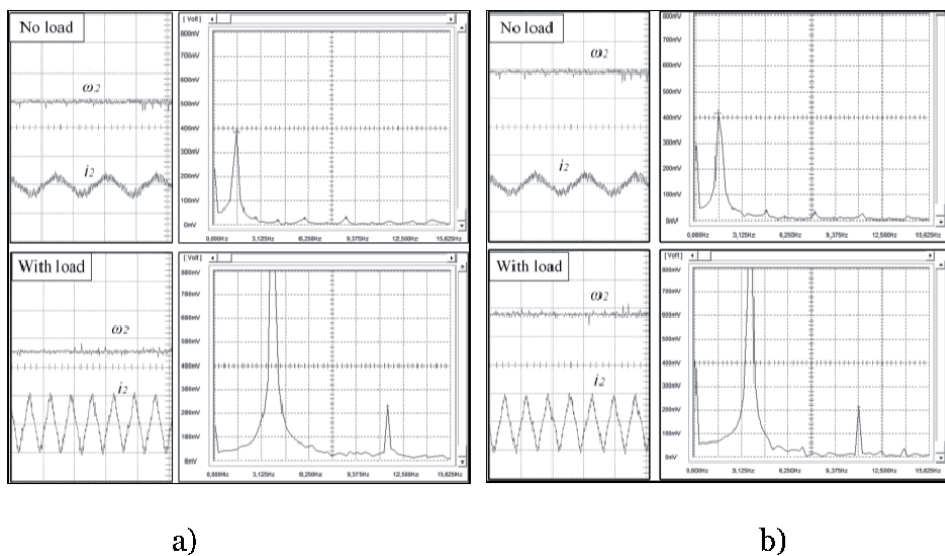


Figure 12.
 The frequency of the stator voltage is 10 Hz (a) and 20 Hz (b).

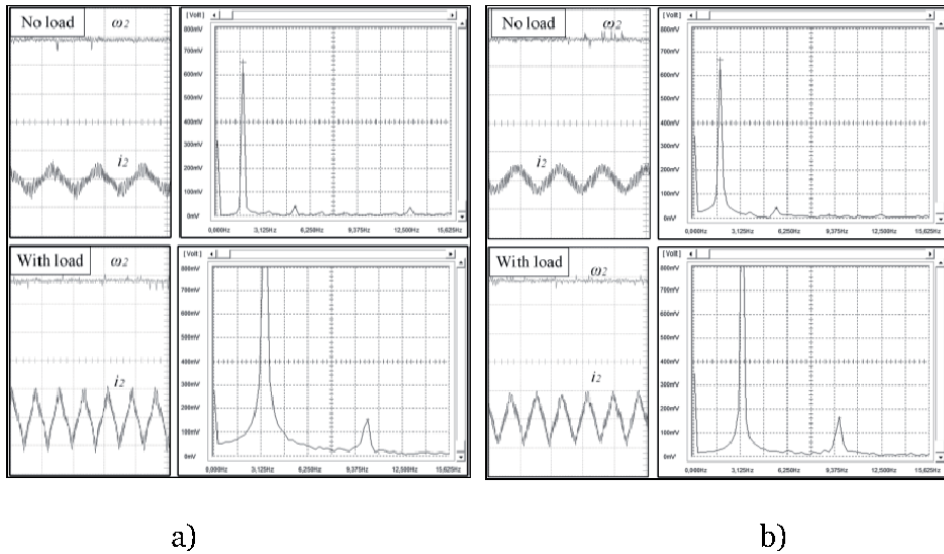


Figure 13.
The frequency of the stator voltage is 30 Hz (a) and 40 Hz (b).

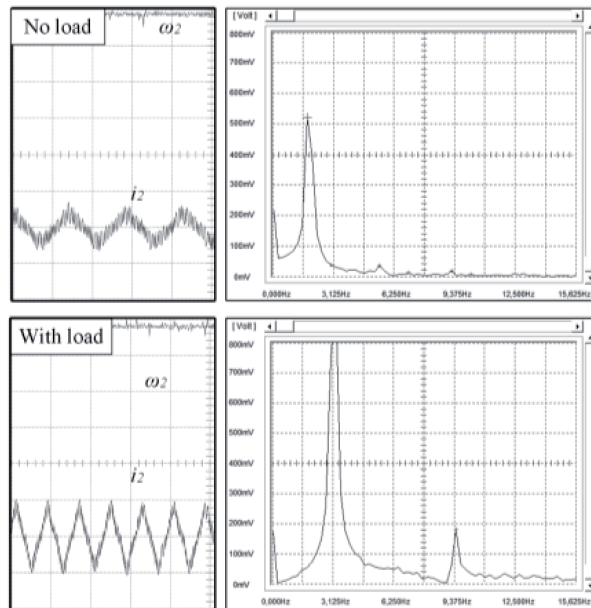


Figure 14.
The frequency of the stator voltage is 50 Hz.

be assumed that sections 1 (**Figure 15**) of the rotor current, characterized by rapid rise and fall, correspond to precisely these sections of the saturation.

With changes in load, the frequencies of the 1st and 3rd harmonics also changed, but the ratio of frequencies did not practically change. The distribution of frequencies and amplitudes of the rotor current depending on different frequencies of the supply voltage is presented in **Table 1**.

Experiments have shown two very important results of a positive torque relationship.

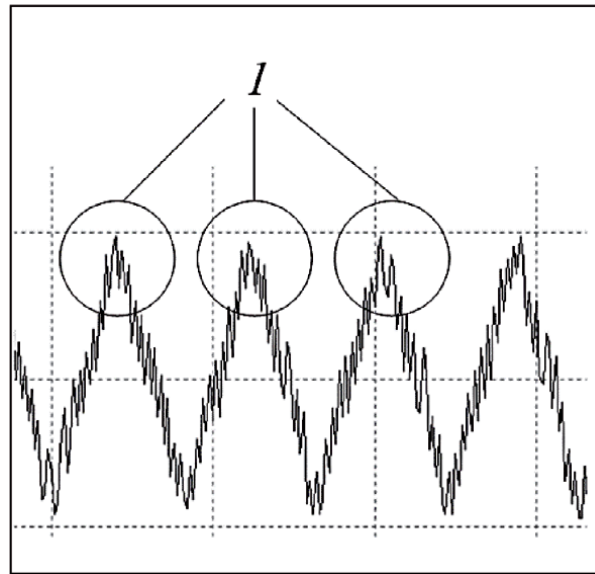


Figure 15.
 Saturation sections characteristic.

ω_1 , Hz	No load				With load			
	1st harm.		3rd harm.		1st harm.		3rd harm.	
	f , Hz	A , V	f , Hz	A , V	f , Hz	A , V	f , Hz	A , V
10	1,5	0,39	4,25	0,019	3,75	1,24	11,5	0,23
20	1,5	0,42	4,75	0,037	3,75	1,32	11	0,21
30	1,75	0,65	5,25	0,039	3,5	1,0	10,25	0,15
40	1,75	0,66	5,5	0,042	3,25	1,35	9,75	0,16
50	1,75	0,52	5,5	0,036	3,25	0,96	9,5	0,18

Table 1.
 Numerical values of the frequencies and amplitudes of the prevailing harmonics of rotor currents in experiments to parry the load at different speeds of rotation (Figures 12–14).

1. These experiments show that the proposed corrections force the magnetic flux under load - that is, they make it possible to obtain the maximum stator magnetic flux - the maximum possible drive efficiency and at the same time the drive maintains the stability of the processes in all modes.
2. According to the frequency of the rotor current without load and under load, it follows that at all speeds of rotation, the parrying of the load occurs at the same absolute slip - 3 Hz, i.e. an initially non-linear asynchronous electric drive is linearized by this connection more accurately than by vector control with a PID speed controller (Figure 11).

In general, the experiments carried out with the stand shown in Figure 6 showed that an electric drive with a torque correction (or an active component of the stator current) has advantages in the dynamics of almost all possible modes - parrying load surges - stepwise and periodic.

5. Modeling

Simulations have also confirmed the effectiveness of the dynamics of corrective link actuators. So in the model (Figure 16) with load surges, the parrying efficiency in schemes with DPF is much higher. This is proved by both the processes in speed (Figures 17–19(a)) and the rotor current spectra (Figures 17–19(c)) and Table 2).

Figures 17–19 shows diagrams of simulated drive acceleration processes from zero to speed corresponding to the frequencies of the stator voltage 10, 20, 30, 40, 50 Hz. Load surges are modeled at steady-state speeds. The diagrams of the speed (diagram a), of the mechanical torque, developed by the motor (diagram b) and the rotor current (diagram c) are displayed. It is obvious that in all modes the frequency of the rotor current in the drive model closed in speed (Figure 17) is significantly higher than in a drive with stator current feedback (Figure 19).

The values of the fundamental frequencies of the rotor current in the models of the electric drive with different control algorithms is presented in Table 2.

In these diagrams, the processes in the speeds of rotation do not differ significantly, but the processes in the rotor currents have significantly different frequencies, which shows the high efficiency of the proposed method for evaluating the

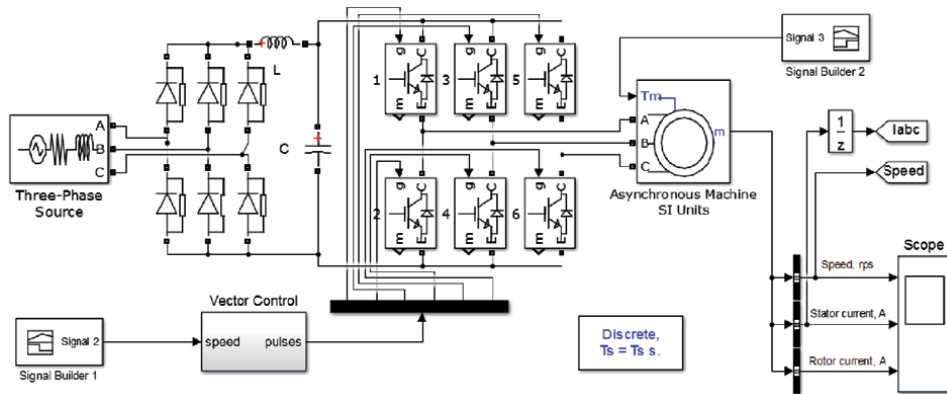


Figure 16. Model of an asynchronous electric drive with vector control in Matlab Simulink.

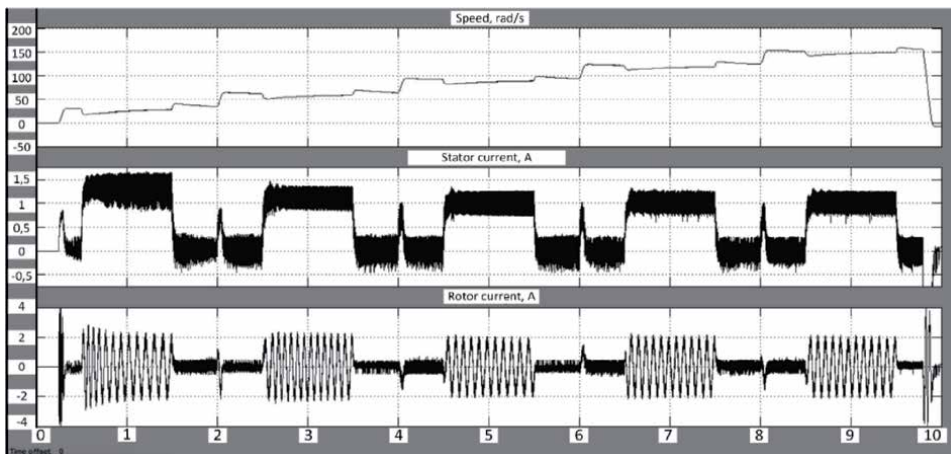


Figure 17. Processes in a vector control drive model.

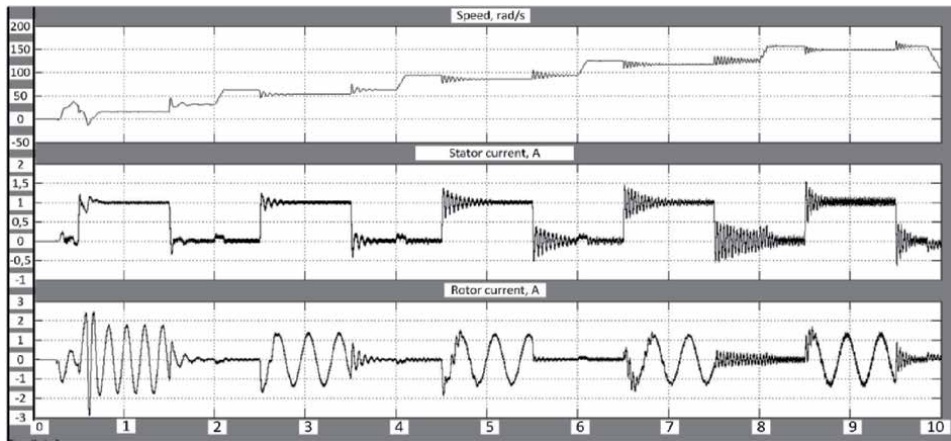


Figure 18.
 Processes in a scalar drive model.

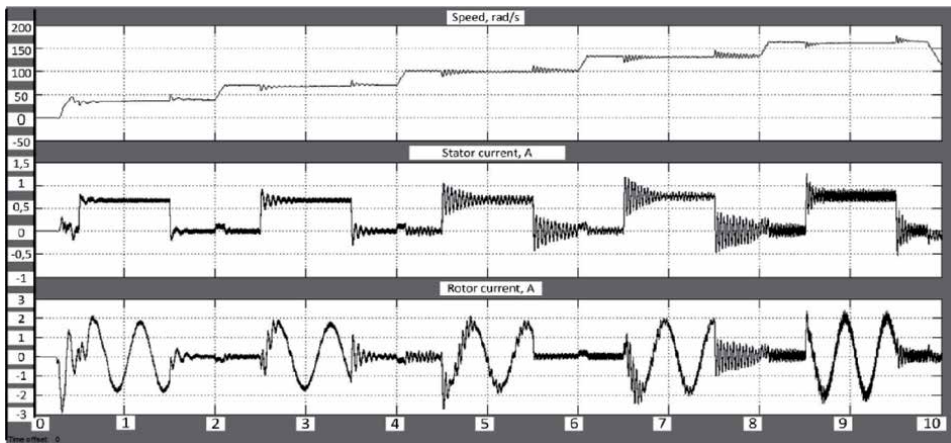


Figure 19.
 Processes in the drive model with torque feedback (active stator current).

Control algorithm	Fundamental frequency, Hz				
	10	20	30	40	50
SC	5,12	2,98	2,66	2,56	2,66
SVC	10,64	12,81	10,62	11,63	11,63
SC with DPF	1,90	1,71	1,71	1,75	2,06

Table 2.
 The fundamental frequencies of the rotor currents of the processes in the model shown in **Figures 17–19**.

method of controlling asynchronous electric machines by rotor currents. It should be expected that the method will be useful in milking machines of wind power plants.

6. Implementation in production mechanisms

The correction was introduced into the electric drives of the transport line, which were experiencing moment loads. According to the conditions of the

technology, transient processes during the “capture” of the transported workpieces had to be minimized. At the same time, it was important to leave asynchronous drives of mechanisms, without transferring these mechanisms to expensive precision drives. Also, several control methods were tested, according to transient processes, shown in **Figures 20–22**. A clear advantage in the quality of working out disturbances - behind a drive with torque coupling (active component of the stator current).

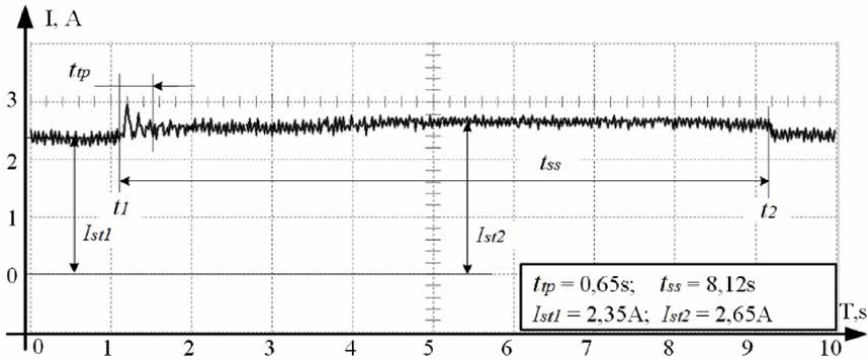


Figure 20.
Scalar controlled electric drive (SC).

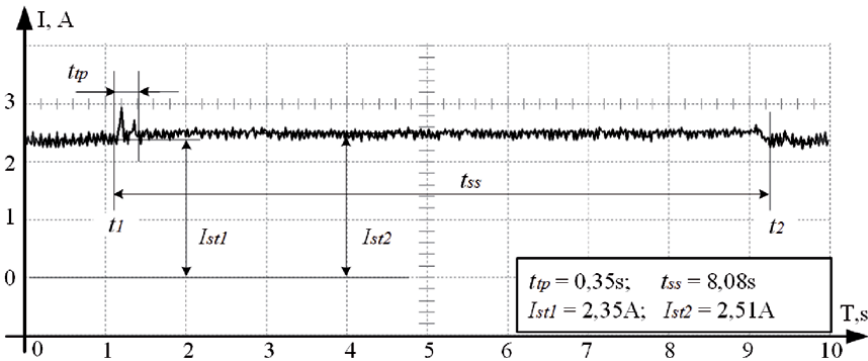


Figure 21.
Vector controlled electric drive (SVC).

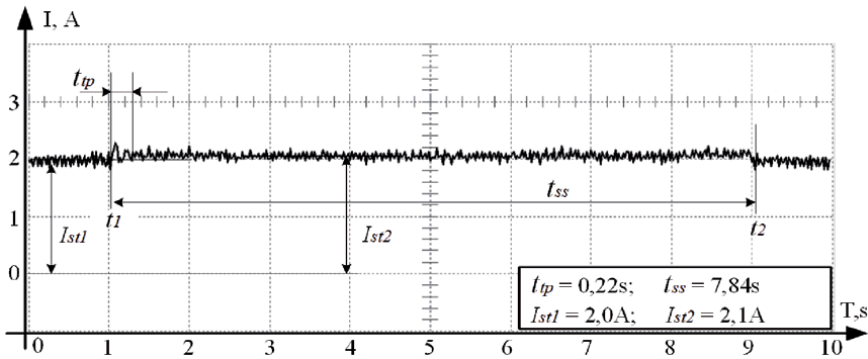


Figure 22.
Stator current feedback electric drive (DPF).

Under production conditions, it was possible to achieve a significant reduction in currents in all modes and times of the transient process.

7. The discussion of the results

According to the simplified vector equations of the DFM during transient processes in the drive, it is quite simple to correct the frequency of the stator voltage by changes in the voltage supplied to the DFM rotor within small limits. As follows from the vector equations, it is sufficient to take into account changes in the rotation speed of the DFM. However, in reality, a wind power plant is a multi-connected structure with complex mutually influencing transient processes that are caused by dynamic gusts of wind and transients in the wind turbines themselves. Vector equations that greatly simplify the description of these complexes do not allow obtaining an effective control structure in transient processes.

The identification of processes in asynchronous electric motors with a wound rotor by a nonlinear transfer function proposed in previous studies describes the processes in SCIM, WRIM and DFM much more accurately and efficiently.

Multidimensional transfer functions will make it possible to describe transient processes in such complex control systems as DFM or induction motors with a wound rotor and effective methods of their correction.

Numerous experiments have shown that cross-connections compensate for the influence of these factors - the influence of variable loads, different frequencies of stator voltage (in this case, it is invariable) is much more effective than other known control methods.

In addition to transient processes, transfer functions will make it possible to describe reactions to variable disturbing factors - periodic reference signals and moment disturbances are described in the works, and in this case, these are the effects of wind and regulation from the rotor.

The dynamic drive will fend off gusts of wind and keep the rotor speed in the range without significant dips, and the stator frequency loop will perform precise control as now. The network mismatch time will decrease and the wind utilization rate will increase. Thus, the DPF correction improves the overloading capacity of the asynchronous machine, and with a dynamic load this improvement is more active than with a static load, which makes the application of this solution in TIR even more effective.

8. Conclusion

Experiments and simulations have shown that in a system with DFM, cross-links in torque and speed also linearize the DFM electric drive system, as in asynchronous electric drives with moment disturbances, providing minimal transient processes that do not interfere with the operation of the system when the wind changes. It should be expected that an asynchronous electric drive with linearizing couplings, effectively working with moment disturbances, will also be effective in wind turbines.

Thus, it can be assumed that the correction has significant prospects when it is used in electric drives based on DFM in wind turbines.

Thus, the advantage of the method of controlling asynchronous electric motors with dynamic torque coupling, confirmed in all experiments and simulations, suggests that for machines with double power supply, a similar algorithm for controlling a frequency converter from the rotor side of the machine will improve their dynamic characteristics and the final efficiency by 5–10% with minimal capital investment.

Author details

Vladimir L. Kodkin*, Alexandr S. Anikin and Alexandr A. Baldenkov
South Ural State University, Chelyabinsk, Russian Federation

*Address all correspondence to: kodkina2@mail.ru

IntechOpen

© 2021 The Author(s). Licensee IntechOpen. This chapter is distributed under the terms of the Creative Commons Attribution License (<http://creativecommons.org/licenses/by/3.0>), which permits unrestricted use, distribution, and reproduction in any medium, provided the original work is properly cited. 

References

- [1] Lyapin Anatoly Sergeevich. "Structural model, model study of the dynamics of an electric drive with a double-feed machine and direct torque control" Scientific and Technical Bulletin of Information Technologies, Mechanics and Optics, no. 4 (80), 2012, pp. 60-64.
- [2] Lyapin A.S. Model study of the double fed machine with current control. Scientific and Technical Journal of Information Technologies, Mechanics and Optics, 2016, vol. 16, no. 4, pp. 731-737. doi: 10.17586/2226-1494-2016-16-4-731-737
- [3] Pat. No. 2336624 Russian Federation, IPC H02P 27/06. Direct Motor Speed Controller / V.L. Kodkin, E.R. Khaybakov. - No. 2006106477/09; Claimed. 02.03.2006; Publ. 02.03.2006, Bul. № 29. – 11p.
- [4] Malcher, M.A. Problems of introduction of frequency regulation in the mining industry / M.A. Malcher, A.S. Anikin // Mining equipment and electromechanics. - 2011. - №4.
- [5] PROBLEMS OF IMPLEMENTATION OF FREQUENCY CONTROL IN MINING INDUSTRY / V.L. Kodkin, A.S. Anikin, M.A. Malcher // Bulletin of the South Ural State University Series: Energy. - Vol. 18. - No.37.-2012.- P.67-71.
- [6] FREQUENCY CONTROL OF ASYNCHRONOUS ELECTRIC DRIVES IN TRANSPORT Kodkin V.L., Anikin A.S. In the collection: 2015 International Siberian Conference on Control and Communications, SIBCON 2015 - Proceedings 2015. C. 7146978. WOS:000380571600016 DOI : 10.1109/SIBCON.2015.7146978
- [7] EFFECTIVE FREQUENCY CONTROL FOR INDUCTION ELECTRIC DRIVES UNDER OVERLOADING Kodkin V.L., Anikin A.S., Shmarin Y.A. Russian Electrical Engineering. 2014. 85. No. 10. P. 641-644. DOI : 10.3103/S1068371214100101
- [8] Experimental research of asynchronous electric drive with positive dynamic feedback on stator current Kodkin V.L., Anikin A.S., Baldenkov A.A. 2017 International Conference on Industrial Engineering, Applications and Manufacturing (ICIEAM) - Proceedings 2017 DOI: 10.1109/ICIEAM.2017.8076179
- [9] Dynamic Load Disturbance Correction for Alternative Current Electric Drives V.L. Kodkin, A.S. Anikin, Y.A. Shmarin 2nd International Conference on Industrial Engineering, Applications and Manufacturing (ICIEAM); South Ural State University Chelyabinsk - Proceedings 2016 DOI: 10.1109/SIBCON.2015.7146978
- [10] Spectral Analysis of Rotor Currents in Frequency-controlled Electric Drives Kodkin V.L., Anikin A.S., Baldenkov A.A. 2nd International Conference on Automation, Mechanical and Electrical Engineering (AMEE 2017) - Proceedings 2017 DOI: doi:10.2991/amee-17.2017.26
- [11] Popov, V. M. [Hyperstability of Dynamic Systems], Springer-Verlag, Berlin (1973)
- [12] Kodkin. V.L. Methods of optimizing the speed and accuracy of optical complex guidance systems based on equivalence of automatic control system domain of attraction and unconditional stability of their equivalent circuits/ V.L. Kodkin// Proceedings of SPIE - The International Society for Optical Engineering. – 2016
- [13] Pat. No. 2412526 Russian Federation, IPC H02P 23/00. The device for frequency control of

an asynchronous electric drive / V.L. Kodkin, A.S. Anikin. - No. 2010108563/07; Claimed. 09/03/2010; Publ. 20.02.2011, Bul. № 5-12 p.

[14] Pat. №155 351 Russian Federation, IPC F03D 7/04, F03D 1/00, F03D 3/00. Adaptive combined device for regulating the rotor speed of the wind power plant / E.V. Solomin, A.S. Anikin., E.A. Sirotkin, E.E. Solomin, A.A. Sirotkin, S.V. Kozlov - No. 2014154564/06; Claimed. 12/31/2014; Publ. 10/10/2015 Bul. № 28-5 p.

[15] Vorob'ev, N.N. Theory of series. //4 ed., Revised. And additional. - Moscow: Science, 1979, – 408 p.

[16] Meshcheryakov VN, and Bezdenezhnykh DV. "Flux linkage observer for a double feed machine controlled by stator and rotor circuits" Vestnik Voronezh State Technical University, vol. 6, no. 11, 2010, pp. 170-173.

[17] Mazalov Andrey Andreevich. "Adaptive wind turbine with a double-feed AC machine" Izvestia of the Southern Federal University. Engineering Sciences, vol. 126, no. 1, 2012, pp. 26-33.

[18] Kodkin, V.L The dynamics identification of asynchronous electric drives via frequency response / V.L. Kodkin, A.S. Anikin, A.A. Baldenkov //International Journal of Power Electronics and Drive Systems.–2019.– Vol. 10 No. 1.– P.66-73

[19] Kodkin, V. Families of Frequency Characteristics, as a Basis for the Identification of Asynchronous Electric Drives / V. Kodkin, A. Anikin, A. Baldenkov //2018 International Russian Automation Conference (RusAutoCon).–2018

[20] Usoltsev, A.A. Vector control of asynchronous motors. Tutorial. - Spb.: ITMO, 2002-120 p. [http://servomotors.](http://servomotors.ru/documentation/frequency_control_of_asynchronous_motors/chastupr.pdf)

[ru/documentation/frequency_control_of_asynchronous_motors/chastupr.pdf](http://servomotors.ru/documentation/frequency_control_of_asynchronous_motors/chastupr.pdf)

[21] Kodkin, V.L Analysis of Stability of Electric Drives as Non-linear Systems According to Popov Criterion Adjusted to Amplitude and Phase Frequency Characteristics of Its Elements, A.S. Anikin, A.A. Baldenkov //2nd International Conference on Applied Mathematics, Simulation and Modelling (AMSM 2017) - Proceedings 2017 P.7-14, DOI: 10.12783/dtetr/amsm2017/14810

[22] Kodkin, V.L The analysis of the quality of the frequency control of induction motor carried out on the basis of the processes in the rotor circuit / V.L. Kodkin, A.S. Anikin, A. A. Baldenkov //Journal of Physics: Conference Series.–2018.–Vol. 944(1)

[23] Kodkin, V. Stabilization of the stator and rotor flux linkage of the induction motor in the asynchronous electric drives with frequency regulation / V. Kodkin, A. Anikin, A. Baldenkov //International Journal of Power Electronics and Drive Systems.– 2020.– Vol. 11 No. 1.– P.213-219 DOI: <http://doi.org/10.11591/ijpeds.v11.i1.pp213-219>

[24] Kodkin, V. Structural correction of nonlinear dynamics of frequency-controlled induction motor drives / V. Kodkin, A. Anikin, A. Baldenkov //International Journal of Power Electronics and Drive Systems.–2020.– Vol. 11 No. 1.– P.220-227 DOI: <http://doi.org/10.11591/ijpeds.v11.i1.pp220-227>

[25] Kodkin, V. Experimental study of the VFD's speed stabilization (retention) efficiency under torque disturbances / V. Kodkin, A. Anikin, //International Journal of Power Electronics and Drive Systems.– 2021.– Vol. 12 No. 1

[26] Kodkin, V. The experimental identification method of the dynamic efficiency for frequency regulation algorithms of AEDs / V. Kodkin, A.

- Anikin, //International Journal of Power Electronics and Drive Systems.– 2021.– Vol. 12 No. 1 (IJPEDS), Vol. 5, No. 3, February 2015, pp. 336~343 <https://www.iaescore.com/journals/index.php/IJPEDS/article/view/5068/4681>
- [27] Boguslavsky Ilya Zelikovich, Danilevich Yanush Bronislavovich, Popov Viktor Vasilievich, and Rogachevsky Vladimir Samuilovich. “Features of the calculation of electromagnetic loads for machines with double power supply taking into account saturation and higher harmonics” SPbPU Scientific and Technical Bulletin. Natural and engineering sciences, no. 1 (166), 2013, pp. 67-73.
- [28] Yahya Ahmed Alamri, Nik Rumzi Nik Idris, Ibrahim Mohd. Alsofyani, Tole Sutikno Improved Stator Flux Estimation for Direct Torque Control of Induction Motor Drives // International Journal of Power Electronics and Drive System (IJPEDS), Vol. 7, No. 4, December 2016, pp. 1049~1060 <https://www.iaescore.com/journals/index.php/IJPEDS/article/view/5822/5589>
- [29] Bonar D.D., Khoury M.J. Real Infinite Series / The Mathematical Association of America, 2006. — 274 p.
- [30] Loday-Richaud M. Divergent Series, Summability and Resurgence II. Simple and Multiple Summability / Springer International Publishing, 2016. — 272 p.
- [31] Srinivas Gangishetti, Tarakalyani Sandipamu Different Control Schemes for Sensor Less Vector Control of Induction Motor // International Journal of Power Electronics and Drive System (IJPEDS), Vol. 8, No. 2, June 2017, pp. 712~721. <https://www.iaescore.com/journals/index.php/IJPEDS/article/view/6757/6394>
- [32] Md. Rashedul Islam, Md. Maruful Islam, Md. Kamal Hossain, Pintu Kumar Sadhu Performance Analysis of a DTC and SVM Based Field-Orientation Control Induction Motor Drive // International Journal of Power Electronics and Drive System
- [33] Kodkin, V.L Performance identification of the asynchronous electric drives by the spectrum of rotor currents / V.L. Kodkin, A.S. Anikin, A.A. Baldenkov //International Journal of Power Electronics and Drive Systems.–2019.–Vol. 10 No. 1.– P.211-218 DOI: <http://doi.org/10.11591/ijpedsv10.i1.pp211-218>
- [34] Pat. No. 2599529 Russian Federation, IPC H02P 25/02. The device for frequency control of an asynchronous electric drive / V.L. Kodkin, A.S. Anikin., Ya.A. Shmarin, A.A. Baldenkov - № 2014151549/07; Claimed. 11/17/2015; Publ. 10.10.2016, Bul. № 28-12 p.

Very Low Voltage and High Efficiency Motorisation for Electric Vehicles

Daniel Matt and Nadhem Boubaker

Abstract

This chapter details the design of a new innovative solid bar winding for electrical machines (either motors or generators) dedicated to the electric propulsion. The goal of this new winding technique is to enhance the performance by better utilizing the stator slot and increasing the copper fill factor to higher than 75%, and also to reduce the inactive copper at the end-windings. Accordingly, many advantages arise from the application of this solid bar winding: higher torque-to-weight ratio, better thermal behavior, lower rotor losses, higher efficiency, higher reliability and lower cogging torque. However, the solid bar has its inherent constraints, which should be considered with care when designing an electric motor: the AC copper losses and the manufacturing process. The suggested winding technique aims at addressing these challenges.

Keywords: solid bar winding, permanent magnet synchronous machine, high performance electric motor, high power-to-weight ratio, electric propulsion, AC copper loss, low voltage winding, high slot fill factor

1. Introduction

The need for a higher competitive electrical machines, mainly in terms of power density and efficiency, is increasing especially in embedded applications (aerospace, Vertical Take-Off and Landing, Electric Vehicle, etc.); these performances are a key differentiator between competitors. As a rule of thumb, nowadays, a good power-to-weight ratio of PM electric motors is around 3 kW/kg (EMAG + mechanical packaging) [1]. Nevertheless, higher values have been proclaimed by many companies and star-ups, but for experimental prototypes where the maturity of the product is still questionable. The definition of the power to weight ratio is still versatile and controversial because, on one hand, the estimation of the total motor weight relies on many parts where some of them are not always considered in the calculation: EMAG, mechanics, coolant weight (in some cases is shared with the system), cables, power electronic, etc., on the other hand, the flexible definition of the output power (continuous or transient).

The opportunities for achieving a big improvement against the state of the art are very limited and challenging due to the very small degree of freedom.

The following expression provides the basic relationship of the sizing electromagnetic power of electric motors (rotational movement). This expression highlights some, but not all, obvious paths to follow in order to improve the performance.

$$P = C k_w \lambda_e B D^2 L_s \Omega \quad (1)$$

Where, C: constant coefficient, k_w : winding factor, λ_e : electric loading (number of ampere-conductors per meter around the bore of the stator), B: magnetic loading (magnetic flux-density in the airgap), D: rotor diameter, L_s : stator corepack length (active length), and Ω : rotation speed.

These are the main routes to enhance the performance of the electrical machines:

- The ferromagnetic materials: there is no noticeable progress since the last 30 years on the electrical steels. The Iron Cobalt alloy (FeCo) is still the best electrical steel point of highest saturation level around 2.4 T and lowest coreloss (at a given lamination thickness and heat treatment), however is much more expensive and require a specific manufacturing process (specific annealing etc.) in comparison with other more conventional electrical steels like the Iron-Silicon alloy (FeSi) [1].
- The permanent magnet grade: the catalog of the permanent magnet suppliers has been extended in the last few years, even though there is no noticeable since many years. High-grade magnets work well at development level (prototype), but they show some serious limitations when it comes to use them in a harsh environment (NdFeB are not suitable for high temperature $> 200^\circ\text{C}$), or to consider the industrialization (high volume production/cost).
- The thermal management: cooling is a key subject nowadays to push the performance of electric motors beyond certain limits. Some novel cooling technologies are very promising but not fully mature yet, such as: hollow conductor (technique so far reserved for high power machines $> \text{MW}$), flooded slot cooling, ...

For a given specification, the selection of an efficient cooling technique can be very challenging because it can compromise the overall performance of the system (optimisation issue) by adding cost, complexity, and weight, and compromising the reliability as well, which can be prohibitive in some embedded applications.

The bar winding presented in this chapter permits to improve the heat exchange in both the slots and the end-windings [1–3].

- The rotational speed: this has been always a research topic of interest. Very high speed motors have their own limitations and constraints, mainly mechanical (rotor sleeving, integrity of the structure, ...).

Many applications require a rotational speed of few 1000 rpm with a minimum stage of reduction between the electric motor and the driven load (typically driven propeller of electric VTOL), which prohibit the use of very high speed motors.

- The fundamental frequency: this is largely exploited nowadays; high fundamental frequency reduce the dimensions and the mass of electrical machines by making the stator back iron and the rotor yoke very thin (few millimeters). High fundamental frequency usually leads to a high pole count paired with a concentrated winding around the tooth ($q < 1$) which offer a very compact motor due to the short end-windings [4].

A thin stator back iron will noticeably reduce the thermal resistance between the copper and the external cooling sources, especially for forced air-cooled motors via the housing fins.

Furthermore, halfbach arrangement is suitable for this type of motors and help getting rid of the rotor yoke, by, for example, gluing the magnets on a non-magnetic wheel such as aluminum or composite material in order to further reduce the weight.

- The electric loading: this is an avenue for improvement, especially through the use of superconducting materials. There definitely has been a lot of progress, but the materials with low critical temperature have not given the expected results so far and the associated cooling devices prohibits any on-board use.

We suggest in this chapter to focus on a different approach to increase the performance of the electric motors by using a new winding technique with solid bars in order to improve the copper fill factor in the slot [1–3]. The fill factor of a conventional electrical machine with random round wire is always less than 45% (CSA pure copper/CSA naked slot). The use of a solid conductor allows reaching higher fill factor at least 75% and consequently enhances the performance of electric motors.

2. Advantages of the solid bar winding

Despite these attractive advantages, the use of solid bar in the armature winding of synchronous machines has been reserved to very limited applications such as MW turbo generators and the aircraft 3-stage generators (APUG, VFG, IDG). Such a winding type becomes more and more common while being introduced in the electric and hybrid electric vehicle for a medium power ranging from 40 kW to 200 kW, it is called hairpin winding. A winding of this ilk is ideal to provide the needed performance when the traction motor of the vehicle required to develop high torque at low speed or during accelerations.

The winding covered in this chapter is different from the hairpin winding and has been used for many applications: electric vehicle, small sport car, utility vehicles, full electric boat, ...

2.1 Enhanced slot fill factor greater than 80%, so better performance and better thermal behavior at both the slots and the end-windings

The performance of any electrical machine is intimately linked to the slot fill factor. There few definition of slot fill factor, here we consider the ratio of total pure copper in one slot per total slot area.

In a conventional overlapping winding with round wire, the copper fill factor is always mediocre and it is very complicated to exploit beyond 45% of the slot area (non-segmented stator), so almost half of the slot volume is inactive and occupied by the air and the different insulation materials (cf. **Figure 1**).

As regards the solid conductor winding we propose here, the slot fill factor is typically higher than 75%. Indeed, the bar is housed in a rectangular slot slightly larger than the bar to allow the slot insulation (slot liner). The slot dimensions are equal to: $w_{\text{slot}} = w_{\text{bar}} + \delta_{\text{sl}}$ and $h_{\text{slot}} = h_{\text{bar}} + \delta_{\text{sl}}$, where δ_{sl} is the gap between the slot wall and the solid conductor intended to receive the slot liner. δ_{sl} typically lies between 0.3 mm and 0.5 mm ($V < 1$ kV and $P < 300$ kW).

Improving the slot fill factor with solid bar will introduce these benefits:

- At a given electric loading and given DC copper loss: when the copper fill factor is improved, the height/size of the slot can be reduced in the same

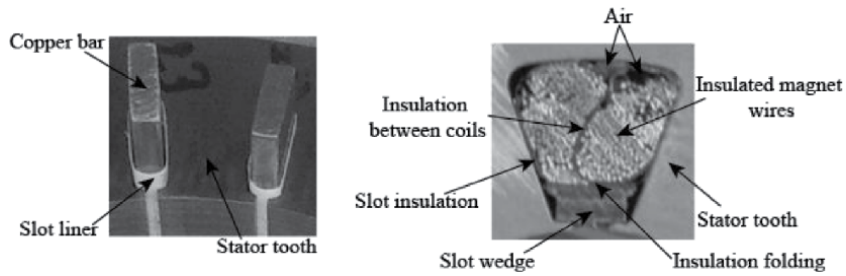


Figure 1. Illustration of the slot fill factor with round wire and with the solid bar proposed in this paper.

	20% fill factor	40% fill factor (baseline)	80% fill factor	90% fill factor
CSA copper in the slot [PU]	0.5	1	2	2.25
Total current in the slot [PU]	0.7071	1	1.4142	1.5
Current density J [PU]	1.4142	1	0.7071	0.6667
Electric loading λ [PU]	0.7071	1	1.4142	1.5000
Copper loss [PU]	1	1	1	1
Copper mass [PU]	0.5	1	2	2.25
Torque [PU]	0.7071	1	1.4142	1.5
Total EMAG weight [PU]	0.9	1	1.2	1.25
Copper weight / Total EMAG weight ratio [PU]	0.111	0.2	0.333	0.360
Torque-to-weight ratio [PU]	0.7857	1	1.18	1.20

Table 1. Motor performance (per unit calculation) versus slot fill factor, at a given slot area and a given DC copper losses.

proportion. A shorter slot leads to a smaller and lighter motor by reducing its outer diameter; or, at a given motor outer diameter (envelope), the stator inner diameter can be increased and, hence, the output torque.

- At a given slot area and a given DC copper losses: a better copper fill factor will permit to increase the torque-to weight ratio of the motor while keeping the same efficiency. For example, increasing the fill factor from 40% with round wire to 80% with solid bars (both values are practical) will permit to multiply the current in the slot by $\sqrt{2}$ and consequently getting +18% torque-to-weight ratio assuming that the copper is around 20% of the total EMAG weight. A per unit calculation is shown in the **Table 1** in order to give an overview of the motor performance for a copper fill factor lying between 20% and 90%, where the baseline case is 40% fill factor (well known value for a standard manufacturing).

In practice, it might be possible to increase the copper loss density in the solid bar winding because the thermal exchanges between the copper and the stator corepack and between the end-windings and the housing are improved (cf. **Figure 1**).

Enhancing the thermal management with solid bar will permit to homogenize the copper temperature and suppress the hotspots, which makes the winding insulation more reliable.

2.2 Less bulky, lighter, and better controlled end-winding, so higher power density and efficiency

The end-windings are always representing an Achilles heel for electric actuators. Indeed, they dissipate the energy without contributing to the creation of useful power. Hotspots usually occur in this part of the winding. The prediction of the volume of the end-windings is difficult, because the geometry is complex and dependent on several poorly controlled factors, such as the winding topology, the tact of the engineer or the machine carrying out the winding,...

In practice, to approximately take into account the loss in the end-windings with round wire in the calculation of the efficiency, the designers multiply the Joule loss dissipated in the slots by an add-on factor generally lying between 1.3 and 2 (distributed winding). It is not unusual to encounter a short electrical machine with end-winding factor of 2; it means that the half-turn axial length is equal to the double of the stator active length (stack length) and therefore the loss in the end-windings are equal to the loss in the active copper located in the slots.

For the bar winding that we propose here, the end-windings volume can be precisely estimated via the relation (13) or (14). Accordingly, the end-windings Joule loss can be accurately predicted as well as the global efficiency of the machine.

Furthermore, we gain in space (shorter machine) and weight and thus better power density and efficiency (**Figure 2**).

2.3 Less constraining slot opening, so improved cogging torque and rotor losses

Despite the fact that some performance of the electrical machine are closely linked to the slotting effect, the slot opening width is not really an optimization parameter in the case of a conventional winding, because it is imposed by the winder to facilitate the insertion of the coils into the slots.

The performance related to the slot opening are:

- Rated torque: the modulation of the flux density caused by the slotting effect impairs the fundamental of the airgap flux density (larger effective airgap) and consequently affects the produced torque.
- Cogging torque: the smoother the stator bore the lower the slotting effect and the cogging torque. This improves the acoustic and vibration behavior of the machine.

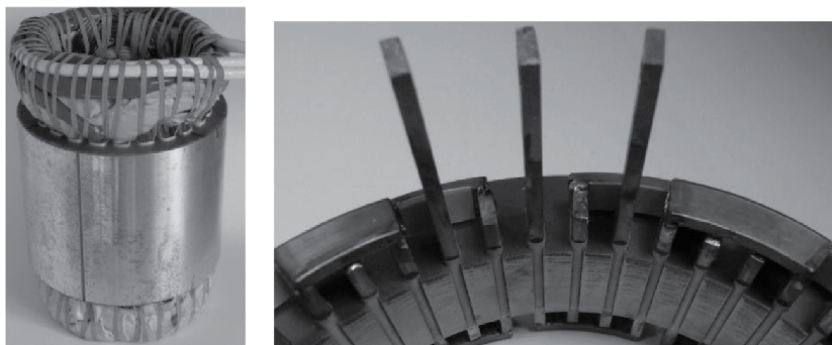


Figure 2.
End-windings of round wire winding (left) - End-windings of solid bar winding (right).

- Rotor eddy-current losses in the magnets, in the conducting retaining sleeve, and in the solid iron rotor: a low slot opening width will significantly mitigate the airgap reluctance modulation seen by the rotor and consequently less induced loss and better efficiency.
- The windage loss: is proportional to the roughness coefficient that depends directly on the surface state of the rotor and stator. It is minimal (~ 1) for a machine with a smooth rotor and low slot opening.

In the case of bar winding, there is no particular constraint on the slot opening because the conductors are inserted by sliding into the stator, which allows to optimize it and to improve the aforementioned performance. The optimum slot opening width with the bar winding proposed in this paper is typically lying between 0.5 mm and 1 mm. It corresponds to a trade-off between a minimal slotting effect and minimal leakage flux (highest produced torque).

3. Novel solid bar winding for electrical machines

3.1 Design principle and manufacturing steps

Unlike the malleable round wire winding, the main complexity of a bar distributed winding is the connection of the overlapping poles at the end-windings level. To overcome this difficulty we have designed a relatively simple system to enable the end-windings connection by means of bent bars alternating overhead and frontally as shown in **Figure 3**, we called them “bow bar” and “crook bar”. The latter are brazed to the bars located in the slots and they have the same cross section (but could be different shape). According to the **Figure 3**, we can distinguish three different lengths of the bars located in the slots: short bar (bow/bow connection), medium bar (bow/crook), and long bar (crook/crook).

The assembly of the proposed bar winding can be broken down into four main steps:

- Cutting of the bars under the different lengths and then the bending of the end-windings connection bars.
- Insulating the stator core with a slot liner made from sheets of material such as: Nomex, Kapton, Dacron-Mylar-Dacron, ...

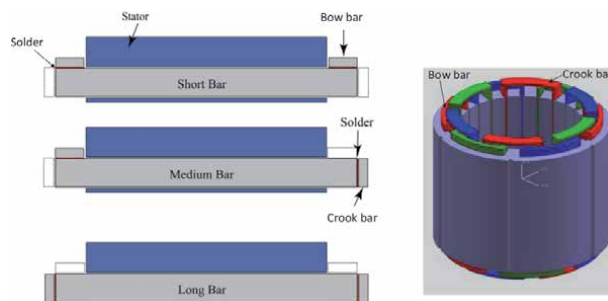


Figure 3. Illustration of the three different end-winding connections, from the top to the bottom: Bow/bow connection, bow/crook connection, and crook/crook connection.

- Insertion of the bars into the slots and joining them to the end-windings bars. Depends on the application (temperature and vibration level), we propose two approaches to connect the end-windings, the first method is based on the soldering only, whereas the second one is using both soldering and screws into threaded holes drilled in the copper.
- Finally, the encapsulation or impregnation of the winding to reinforce the electrical insulation, increase the mechanical strength of the bars, and improve the heat exchange (especially at the end-windings).

3.2 Analytical relationships governing the proposed winding technique

In this part, we propose some practical and generalized analytical relationships allowing a quick determination of the dimensional characteristics of the proposed winding.

We consider the case of three-phase distributed winding, with one slot per pole and per phase ($q = 1$), and star connection.

The proposed relationships depend on whether the number of pole pairs, p , is even or odd. To facilitate the determination of these relationships, we consider the developed winding layout shown in **Figure 4(a)** (p is even: $4p$, $24s$) and **Figure 4(b)** (p is odd: $5p$, $30s$).

According to the **Figure 4**, we can clearly note the different lengths of bars stated earlier in the previous section: short bar (bow/bow), medium bar

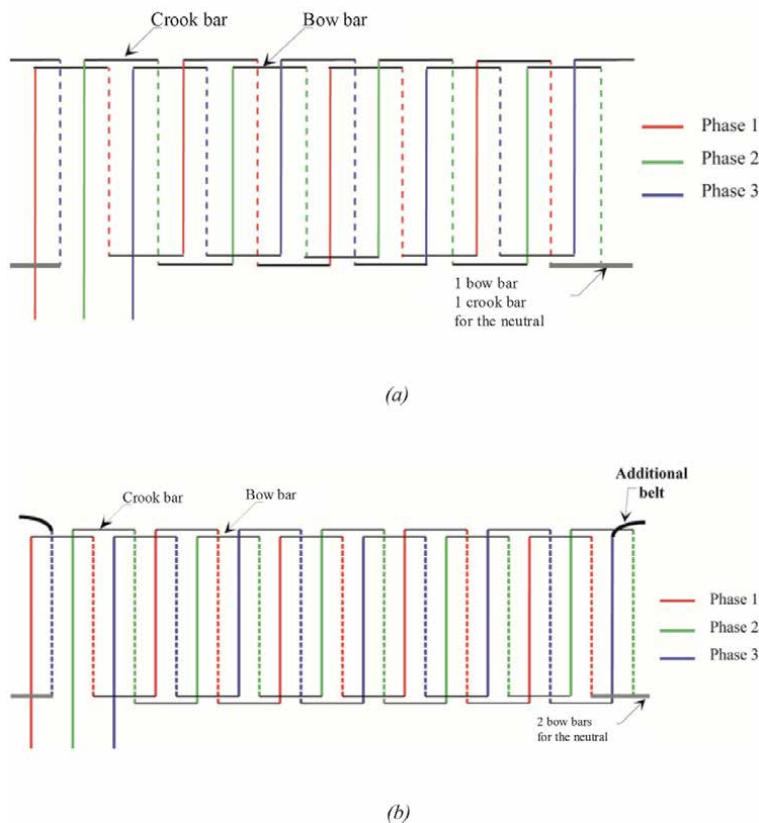


Figure 4. Developed winding layout, for two different cases: $4p/24s$ and $5p/30s$. (a) $p = 4$. (b) $p = 5$.

(bow/crook), and long bar (crook/crook). We also note that if p is even the connection of the neutral is ensured by an “bow bar” and “crook bar”, whereas if p is odd the connection of the neutral is performed with two “bow bars”.

3.2.1 Number of the different bars

If p is even, the number of short bars, n_{sb} , the number of medium bars, n_{mb} , the number of long bars, n_{lb} , the number of bow connection bars (including neutral), n_{bb} , and the number of crook connection bars (including neutral), n_{cb} , are given by the following relationships:

$$n_{sb} = \frac{N_{slot} - 8}{4} + 1 \quad (2)$$

$$n_{mb} = 2 \frac{N_{slot} - 8}{4} + 2 = 2 n_{sb} \quad (3)$$

$$n_{lb} = \frac{N_{slot} - 8}{4} + 2 = n_{sb} + 1 \quad (4)$$

$$n_{bb} = \frac{2N_{slot} - 8}{4} + 2 = n_{cb} + 1 \quad (5)$$

Otherwise, if p is odd:

$$n_{sb} = \frac{N_{slot} - 6}{4} + 1 \quad (6)$$

$$n_{mb} = 2 \frac{N_{slot} - 6}{4} + 2 = 2 n_{sb} \quad (7)$$

$$n_{lb} = \frac{N_{slot} - 6}{4} = n_{sb} - 1 \quad (8)$$

$$n_{bb} = \frac{2N_{slot} - 8}{4} + 2 = n_{cb} + 2 \quad (9)$$

The sum of the different bars must satisfy this relationship:

$$n_{sb} + n_{mb} + n_{lb} = N_{slot} - 3 = 6p - 3 \quad (10)$$

where N_{slot} is the stator slot number.

3.2.2 Total volume and length of the copper: end-winding ratio

One of the main advantages of the proposed bar winding, with respect to the conventional round wire winding, is that the end-winding copper volume can be accurately estimated from the machine's basic parameters (conductor height/width, slot number etc.).

All the machine's dimensions necessary to calculate the total length of the copper as well as the end-winding ratio are illustrated in the **Figure 5**.

The total volume of the winding copper, $V_{CopperTot}$, could be split into two parts: the copper located in the slots, $V_{CopperSlot}$, and the copper in the end-windings, $V_{CopperEW}$:

$$V_{CopperTot} = V_{CopperSlot} + V_{CopperEW} \quad (11)$$

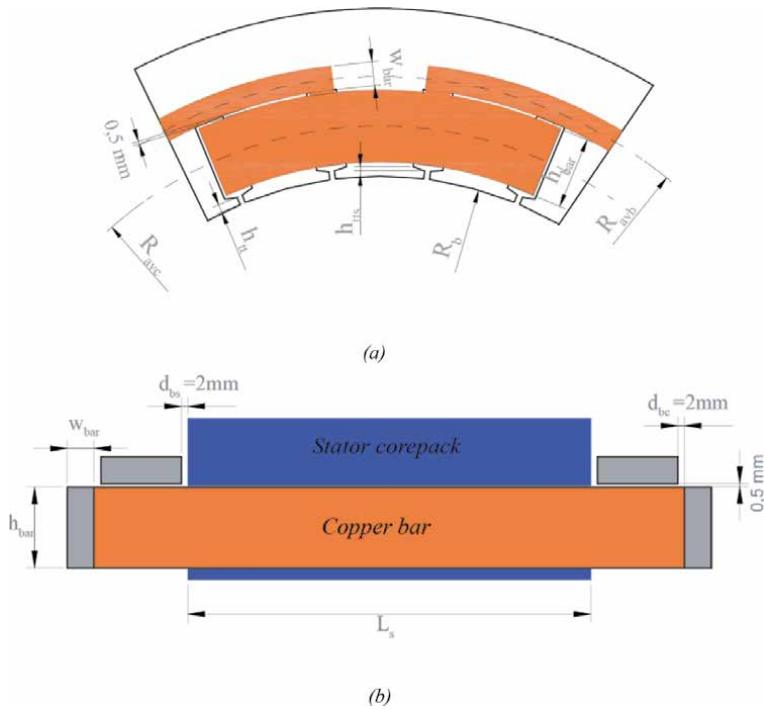


Figure 5. Geometrical parameters of the proposed solid bar winding. (a) Front view. (b) Longitudinal section view.

The end-winding copper is the sum of the bent connection bars (bow and crook) and the part of the bars located in the slots which overhangs the stator magnetic core.

Hence, $V_{CopperSlot}$ and $V_{CopperEW}$ could be accurately estimated by means of the relations (12), (13), and (14).

$$V_{CopperSlot} = N_{slot} h_{bar} w_{bar} L_s \quad (12)$$

where L_s is the length of the stator core pack; h_{bar} and w_{bar} are the height and the width of the solid conductor respectively.

If p is even:

$$V_{CopperEW} = h_{bar} w_{bar} \left[2 n_{sb} (h_{bar} + d_{bs}) + n_{mb} (2 h_{bar} + 2 d_{bs} + d_{bc}) + 2 n_{lb} (h_{bar} + d_{bs} + d_{bc}) + (n_{cb} - 1) \left(\frac{6\pi}{N_{slot}} R_{avc} + w_{bar} \right) + (n_{bb} - 1) \left(\frac{6\pi}{N_{slot}} R_{avb} + w_{bar} \right) + \frac{4\pi}{N_{slot}} (R_{avc} + R_{avb}) + 2 w_{bar} \right] \quad (13)$$

Otherwise, if p is odd:

$$V_{CopperEW} = h_{bar} w_{bar} \left[2 n_{sb} (h_{bar} + d_{bs}) + n_{mb} (2 h_{bar} + 2 d_{bs} + d_{bc}) + 2 n_{lb} (h_{bar} + d_{bs} + d_{bc}) + n_{cb} \left(\frac{6\pi}{N_{slot}} R_{avc} + w_{bar} \right) + (n_{bb} - 2) \left(\frac{6\pi}{N_{slot}} R_{avb} + w_{bar} \right) + \frac{8\pi}{N_{slot}} R_{avb} + w_{bar} \right] \quad (14)$$

We may express the total volume of the winding copper, $V_{CopperTot}$, as equal to the product $L_{CopperTot} h_{bar} w_{bar}$, where $L_{CopperTot}$ is the total length of the winding (3 phases) and can be inferred from the previous relations (12), (13) and expressed as:

$$L_{CopperTot} = \left[N_{slot} L_s + 2 n_{sb} (h_{bar} + d_{bs}) + n_{mb} (2 h_{bar} + 2 d_{bs} + d_{bc}) + 2 n_{lb} (h_{bar} + d_{bs} + d_{bc}) + (n_{cb} - 1) \left(\frac{6\pi}{N_{slot}} R_{avc} + w_{bar} \right) + (n_{bb} - 1) \left(\frac{6\pi}{N_{slot}} R_{avb} + w_{bar} \right) + \frac{4\pi}{N_{slot}} (R_{avc} + R_{avb}) + 2w_{bar} \right] \quad (15)$$

The end-winding ratio, τ_{EW} , which represents the ratio of the overhangs copper to the total winding copper, can be easily and precisely estimated via the relations (12) and (13) or (14):

$$\tau_{EW} = \frac{V_{CopperEW}}{V_{CopperTot}} = \frac{V_{CopperEW}}{V_{CopperSlot} + V_{CopperEW}} \quad (16)$$

Relation 15 gives an idea about the copper wasted in the end-winding which is inactive because it does not participate in the creation of the torque. The lower is τ_{EW} the higher are the performance of the machine in terms of power density and efficiency.

3.2.3 DC copper loss

Once the section of the conductor is known as well as the total length of the copper (cf. calculation in the previous section), the DC Joule loss can be accurately estimated from the following relation:

$$\begin{aligned} P_{ohmic} &= \rho_{20C} (1 + 0.004 (T_{op} - 20)) \frac{L_{CopperTot}}{h_{bar} w_{bar}} I_{rms}^2 \\ &= \rho_{20C} \left(\frac{234.5 + T_{op}}{235.5 + 20} \right) \frac{L_{CopperTot}}{h_{bar} w_{bar}} I_{rms}^2 \end{aligned} \quad (17)$$

where ρ_{20C} is the copper electrical resistivity at 20°C and T_{op} is the copper operating temperature.

The solid copper conductor is always prone to supplementary loss called AC copper loss. This topic is treated in the next section.

4. AC copper loss in solid conductor winding

A solid conductor is very favorable to additional losses due to the eddy-currents and circulating currents. Special attention must be paid to the bar design according to the frequency, otherwise the AC electrical resistance could increase tremendously. The cross-section area of the conductor is then restricted in the solid bar winding, which is a drawback. This problem does not arise for round wire winding where the use of stranded, insulated, and twisted wires (Litz wire) enable to overcome this limitation.

Three different phenomena could contribute to increase the loss in a solid conductor of electrical machines: the skin effect, the slot leakage flux, and the rotating field. A three-dimensional illustration of these effects is given in the **Figure 6**.

4.1 Skin effect in a solid conductor

It is the well-known effect that tends to concentrate the current at the periphery of the conductor, this in an increasingly way as the frequency increases. The skin effect is due to opposing eddy-currents induced by the varying magnetic field, B_{in} in the **Figure 6**, resulting from the alternating current.

The **Figure 7** illustrates the skin effect in a solid copper bar with a cross-sectional area of $4 \times 12 \text{ mm}^2$ and carrying an alternative current at 550 Hz.

The resistance factor, K_{skin} , which is the ratio of the AC effective resistance to the DC ohmic resistance, related to the skin effect in a solid rectangular conductor could be predicted from the Levasseur's relation [5]:

$$K_{skin} = \frac{R_{AC}}{R_{DC}} = \sqrt[6]{0.178 + \left(\frac{h_{bar} w_{bar}}{2(h_{bar} + w_{bar})} \sqrt{\sigma \mu r f} \right)^6} + 0.25 \quad (18)$$

where $\mu = \mu_0 \mu_r$: the magnetic permeability, σ : the electrical conductivity, f : the frequency of the current.

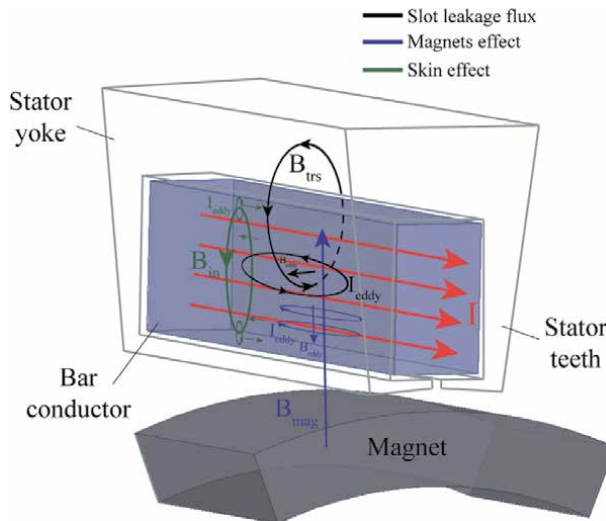


Figure 6. 3D representation of the magnetic fields and their associated eddy-currents in a solid bar winding.

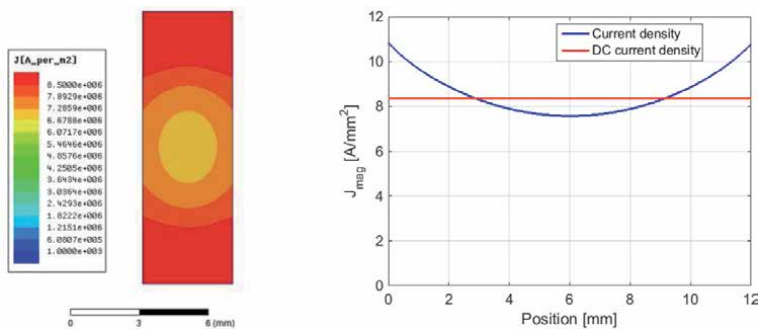


Figure 7. Skin effect in a rectangular solid bar.

For a better use of the copper area, the goal is always to obtain K_{skin} close to the unit.

The pure skin effect only concerns the end-windings, which is the part of the copper in the air.

For example, at $f = 1000$ Hz, $h_{bar} = 6$ mm and $w_{bar} = 4$ mm, the resistance factor K_{skin} is circa 1.05. For the considered frequencies, the conventional skin effect is negligible compared to the effect of the current displacement occurring inside the slots, cf. next section.

4.2 Effect of the cross-slot leakage flux: critic height of the solid bar

4.2.1 Effect of the cross-slot leakage - field effect

The slot leakage flux could create an extra copper loss in solid conductors surrounded by a magnetic material. This is an old phenomenon that was treated on large alternators and frequently called Field effect.

Indeed, the alternating leakage field due to the armature current, represented by B_{lrs} in **Figure 6**, tends to close through the stator slot and create eddy-currents that oppose the main current at the bottom of the slot and are superposed to it near to the slot opening. This induces an increased current density in the conductor cross-sectional area close to the bore of the stator. Hence, the unequal current distribution results in increased effective resistance and consequently higher copper loss.

The **Figure 8** shows 2D and 3D illustrations of the irregular current distribution in a solid copper bar surrounded by a magnetic material, with a cross-sectional area of 4×12 mm² and carrying an alternative current at 550 Hz.

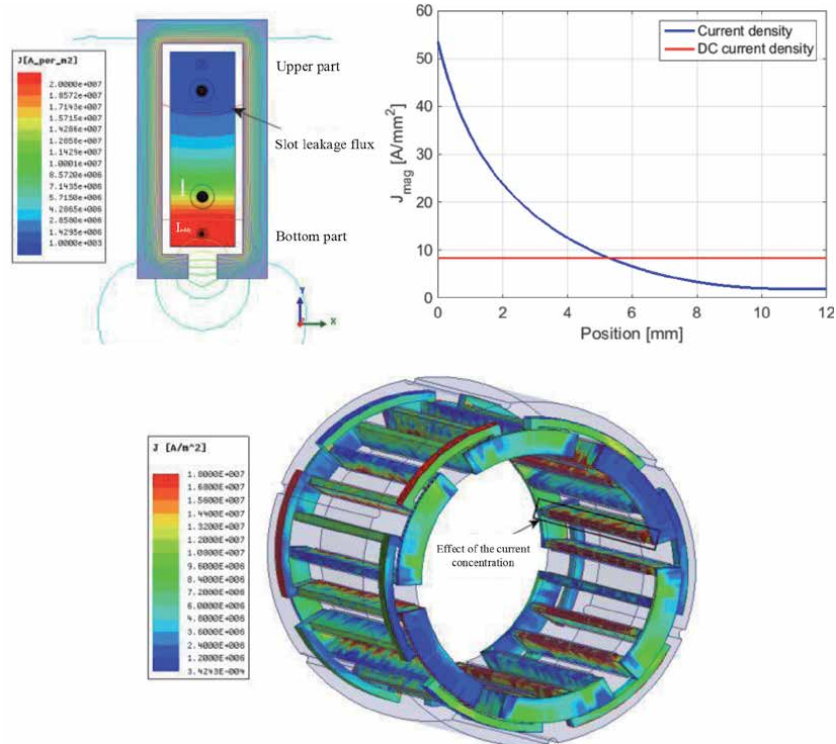


Figure 8. Non-uniform distribution of the current density in a solid conductor surrounded by a magnetic material. 2D FEA analysis (top) and 3D FEA analysis (bottom).

This same leakage flux effect is usefully exploited in double cage asynchronous machine to enhance the starting torque.

The resistance ratio, K_{leak} , related to the slot leakage flux in a solid conductor surrounded by a magnetic material could be estimated as follows [6]:

$$K_{leak} = \frac{R_{AC}}{R_{DC}} = \xi \frac{\sinh(2\xi) + \sin(2\xi)}{\cosh(2\xi) - \cos(2\xi)} \quad (19)$$

where ξ is the reduced height of the conductor, and is expressed by:

$$\xi = h_{bar} \sqrt{\sigma \mu \pi f \frac{w_{bar}}{w_{slot}}} = \frac{h_{bar}}{\delta} \sqrt{\frac{w_{bar}}{w_{slot}}} \quad (20)$$

It must be pointed out that the relation 18 is valid for simple layer winding (one bar per slot), which corresponds to the winding we are proposing here. Otherwise, a second term must be added in the relation 18 to take into account the proximity effect between the different elementary layers.

4.2.2 The critic height of the bar, important notion

For a given width and frequency, a solid conductor surrounded by a magnetic material has an optimum height called *critic height*, h_{critic} [1, 6]. Indeed, h_{critic} is the threshold corresponding to the lowest AC resistance, under which the losses increase strongly, whereas if it is exceeded the losses tend to stagnate or increase very slightly in spite of the increase of the conductor cross-section. In other words, the critic height corresponds to the useful cross-section in which the current flows, so, it is useless to go beyond this critical height, however, if $h_{bar} < h_{critic}$ the losses will increase because the current density increases in the conductor.

For the sake of illustrating what has been said above, we performed a 2D finite element calculation of the AC Joule loss in a copper bar with: fixed width of 4 mm, variable height between 1 mm and 20mm, a length of 1 m, carrying an alternating current of 285 A_{rms}, and with parameterized frequency between 50 Hz and 1000 Hz. The results are presented on the **Figure 9**; we notice that there is an optimal height where the additional losses are minimal (minimum AC resistance) and which decreases with the frequency.

The h_{critic} can be defined by the following relationship [6]:

$$h_{critic} = \frac{1.32}{2\pi \sqrt{\frac{w_{bar}}{w_{slot}} \frac{f}{\rho 10^7}}} = 1.32 \sqrt{\frac{w_{slot}}{w_{bar}}} \delta \quad (21)$$

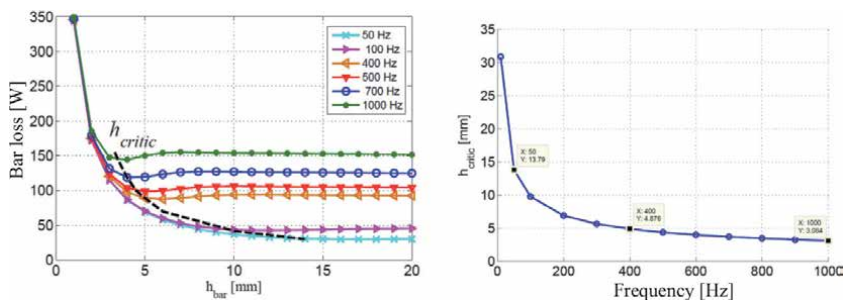


Figure 9. AC copper loss at 20°C in a rectangular solid bar with $w_{bar} = 4mm$ — Illustration of the critic height of the bar: Finite element analysis (left) and analytical relationship (21) (right).

Where δ is the skin depth of the bar, $\delta = 1/\sqrt{\sigma\mu\pi f}$.

The h_{critic} calculated by the relationship (21), for the same bar width $w_{\text{bar}} = 4$ mm, is presented in the **Figure 9(b)**, it can be shown that the analytical calculation is in good general agreement with the finite element analysis in the **Figure 9(a)**.

As a rule of thumb, at 1 kHz operating frequency, at copper operating temperature around 150°C, the optimum copper bar height is around 4 mm.

4.2.3 Optimization of the AC loss in a solid conductor located in a magnetic core

To overcome the phenomenon of the uneven distribution of the current density due to the slot leakage flux, the most famous technique consists in subdividing the stator bars into parallel layers insulated from each other and regularly transposed along the length, so that each elementary conductor occupies different positions in the slot from the root to the head of the slot. With this technique the slot root inductance and the slot head inductance are balanced and the current tends to flow over the entire copper cross-sectional area. Consequently, the extra loss is tremendously mitigated and getting closer to the ohmic loss (DC loss). This technique is complex and impairs the copper fill factor compared to undivided bar due to the multiple insulations between the elementary conductors. It is commonly used for large generators (> 100MW rating) and called “*Roebel bar*”.

Using insulated conductors with simple paralleling (without twisting) is not sufficient to reduce losses, because the bars create circulating currents between each other, resulting in additional losses identical to those produced in an equivalent solid bar. The 2D finite element simulation in **Figure 10** shows that the current density distribution in the parallel insulated conductors is the same with respect to a one solid bar (concentration near the slot opening).

However, the subdivision of the bar into n sub-conductors in series can optimize the AC copper losses by imposing a current of I/n in each elementary conductor independently of its position in the slot. However, it should be emphasized that this is subject to the judicious choice of the number of sub-conductor, otherwise, the additional loss can be significantly increased following an inadequate series connection (reverse effect).

4.3 Effect of the rotating field

In lesser extent, there is a third effect caused by the rotor field traveling in front of the stator which is represented by B_{mag} in **Figure 6**. In this case, it is the rotating

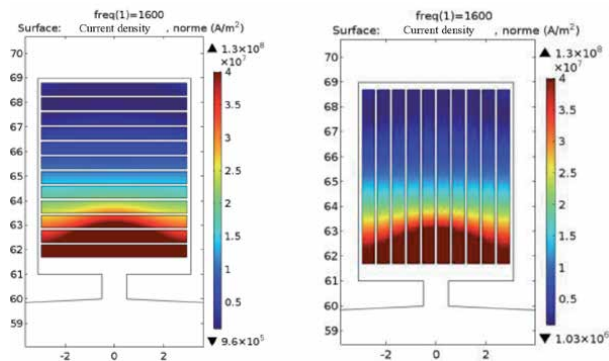


Figure 10. Current density distribution in a copper bar following a simple paralleling.

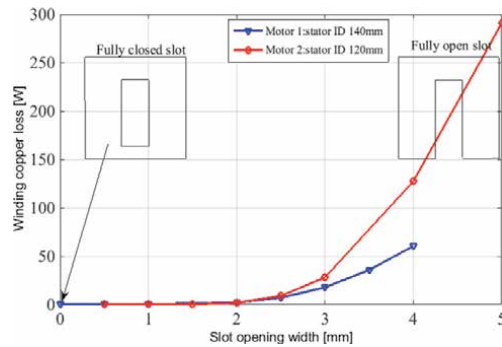


Figure 11.
Eddy-current loss in a solid bar due to the rotating field.

magnetic field of the permanent magnet mounted on the surface of the rotor. The variable B_{mag} could be seen by the solid conductors and, consequently, creates an extra eddy-current loss [1]. This loss component mainly depends on the slot opening and the saturation level of the iron surrounding the bar. If the slot is close enough the flux will be canalized by the iron and does not cross the copper. The typical slot opening width of the solid bar winding that we propose in this paper is between 0.5 and 1 mm (bar slipped into the slot). A finite element analysis, carried out on two different PM motors, has proven that the induced loss due to the rotating field is negligible for the slot opening lower than 2 mm, the results are shown in **Figure 11**.

5. Case study: FEA analysis, prototype manufacturing and testing

Many motor using the solid bar winding developed here were manufactured and tested successfully; all these motors were dedicated to the electric propulsion (e-Cars, e-Boats, ...).

The main characteristics of one of these motor are presented in the **Table 2**. The stator and rotor photos are presented in the **Figure 12**.

The first test was carried out at no load by driving the motor with another machine. The line to line back EMF was measured and showed a good agreement with the predicted back EMF via the commercial FEA tool ANSYS Maxwell (cf. **Figure 13**).

The electrical power at the input of the inverter driving the motor at no load was measured as well, this measurement represents the total no load losses of the motor. At 3700 rpm, the total no load losses are equal to 300 W, cf. **Table 3**.

Afterwards, a test rig was set up in back-to-back configuration (two identical motors) for the full load testing, as shown in **Figure 14**. The electrical power was measured at the output of the inverter driving one of the two motors by consuming the electrical power from the battery rack. The winding of the second motor is generating the power to charge the same battery. The output mechanical power was measured via a torque meter installed between the two motors.

The flux density and the full load torque were checked with ANSYS Maxwell and presented in the **Figures 15** and **16** respectively.

The extra on load losses dissipated in the motor were isolated based on the measurements and the AC copper losses predicted by means of the FEA analysis; the calculation is detailed in the **Table 3**. These extra losses present 8% of the total on load losses (42 W/520 W), they occur in any inverter fed electric motors and can be split into many components:

Dimensions	
Stator outer diameter	180 mm
Stator inner diameter	140 mm
Magnetic airgap	1,5 mm
Magent height	6.1 mm
Stator stack length	50 mm
Winding bar dimensions (h _x w)	6x4 mm
Slot dimensions (h _x w)	7x5 mm
Materials	
Stator corepack	M270-35A
Magnets	N35UH
Electrical parameters	
Pole number	16
Slot number	48
Phase resistance, 20°C - 100°C	1,3 mΩ - 1,7 mΩ
Phase inductance	12 μH
Back EMF coefficient k_e	41,1 mVs/rd
Torque coefficient k_t	0,123 Nm/A
Total weight (including mechanics)	10 kg
Nominal torque-to-weight ratio	2.5 Nm/kg
Cooling	Natural convection

Table 2.
Motor characteristics.



Figure 12.
Photo of the prototype. Left: Standalone wound stator with bar winding - Right: Glued magnets on the rotor wheel and sleeved rotor.

- The additional core loss due to the polluted current injected by the inverter.
- The extra AC copper loss due to the distorted current from the inverter (switching harmonics).
- Stray losses: these regroup all the “non-conventional” losses such as the eddy-current losses in the metallic structure of the motor (e.g. the end-windings leakage flux can generate eddy-currents in the flanges ...).

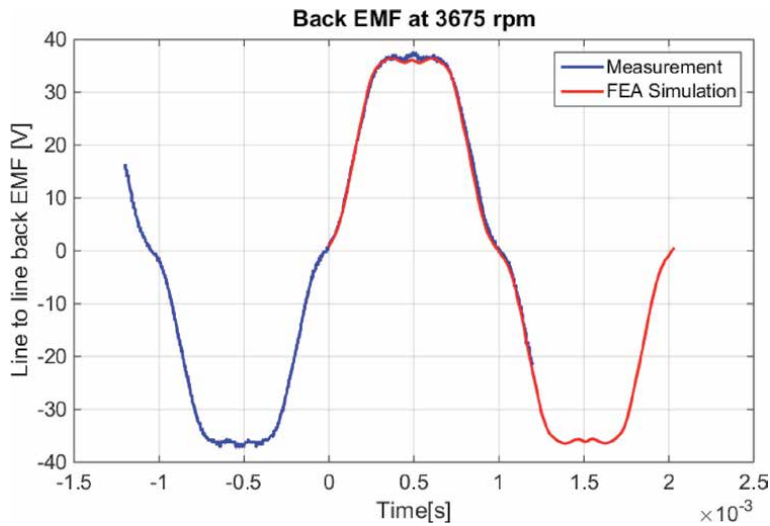


Figure 13.
 Line to line back EMF at 3700 rpm and at 80°C magnet temperature.

(1)	Phase current [Arms]	170
(2)	Copper temperature [°C]	100
(3)	Speed [rpm]	3700
(4)	Frequency [Hz]	493.33
(5)	Torque [Nm]	20
(6)	Total phase resistance - Measured [mOhms]	1.7
(7)	Total phase resistance - copper in slots only [mOhms]	0.739
(8)	Total phase resistance - copper the end-windings only [(6)–(7)] [mOhms]	0.961
(9)	DC copper loss at end-windings only [W]	83.36
(10)	DC copper loss in the slots only [W]	64.03
(11)	Kleak relationship 18 in Section 4.2.1	1.59
(12)	AC copper loss in the slots only - Analytical prediction [(11) x (9)] [W]	101.81
(13)	AC copper loss in the slots only - 2D FEA Ansys Maxwell [W]	93
(14)	Total no load losses - Measured (no load core loss + mechanical losses) [W]	300
(15)	Magnet eddy-current loss - 2D FEA Ansys Maxwell [W]	1.4
(16)	Sleeve eddy-current loss (non conductive) [W]	0
(17)	Motor electrical input power - Measured [W]	8270
(18)	Motor mechanical output power - Measured [W]	7750
(19)	Motor total on load losses - Measured [(17)–(18)] [W]	520.00
(20)	Total additional losses [(19)–(15) - (14) - (13) - (9)] [W]	42.24
(21)	Efficiency of the motor - Measured [%]	93.712

Table 3.
 Motor losses breakdown.

The different tests carried out have shown that the motor is able to reaches the required performance point of view output power, efficiency and thermal behavior. The total losses were proven to be at the predicted level.



Figure 14.
 Photo of the test rig – The identical motors are connected in back-to-back configuration.

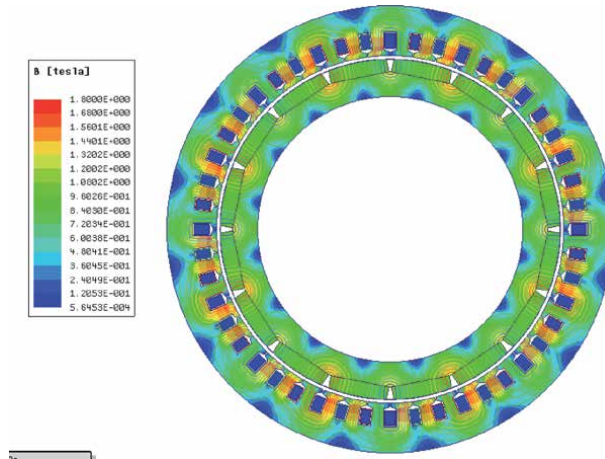


Figure 15.
 On load flux density obtained from FEA analysis (ANSYS Maxwell) at 170 arms/20 nm.

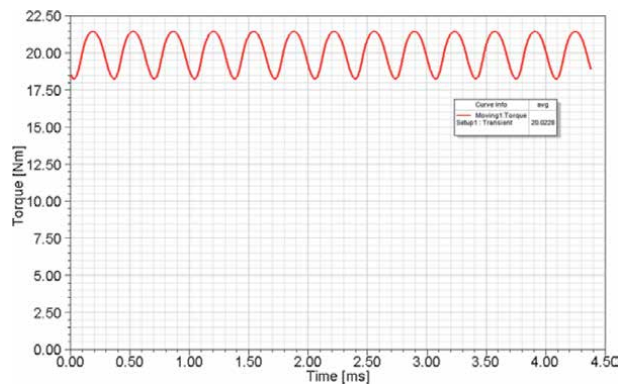


Figure 16.
 Electromagnetic torque calculated by FEA at 170 Arms and 80°C magnet temperature.

Author details


Daniel Matt^{1*} and Nadhem Boubaker²

1 University of Montpellier, Montpellier, France

2 Safran Electrical and Power, Pitstone, UK

*Address all correspondence to: daniel.matt@umontpellier.fr

IntechOpen

© 2021 The Author(s). Licensee IntechOpen. This chapter is distributed under the terms of the Creative Commons Attribution License (<http://creativecommons.org/licenses/by/3.0>), which permits unrestricted use, distribution, and reproduction in any medium, provided the original work is properly cited. 

References

- [1] Boubaker N. Study of atypical losses in high performance permanent-magnet synchronous machines for aircraft applications [thesis]. University of Montpellier; 2016.
- [2] Enrici Ph, Boubaker N, Matt D. Bar Winding for the Low-Voltage Motorization of an Electric Tractor. In: Proceedings of the International Conference on Electrical Machines (ICEM); 23–26 August 2020; Gothenburg. Sweden: IEEE; 2005. p. 1711–1717
- [3] Lorenzo P, Matt D, Gimeno A, Boubaker N. Contribution on AC bar windings losses reduction for a high frequency and high performance machine for aeronautical application. In: Proceedings of the International Symposium on Electromagnetic Fields in Mechatronics, Electrical and Electronic Engineering (ISEF); 29–31 August 2019; Nancy. France: IEEE; 2020. DOI 10.1109/ISEF45929.2019.9097026
- [4] Boubaker N, Matt D, Enrici Ph, Nierlich F, Durand G. Measurements of Iron Loss in PMSM Stator Cores Based on CoFe and SiFe Lamination Sheets and Stemmed From Different Manufacturing Processes. IEEE Transactions on Magnetics. 2018; DOI: 10.1109/TMAG.2018.2877995
- [5] Levasseur A. Nouvelles formules, valables à toutes les fréquences, pour le calcul. Journal de Physique et le Radium. 1930.
- [6] Liwschitz M. Calcul des machines électriques. SPES; 1967. 276 p.

MNLR and ANFIS Based Inductance Profile Estimation for Switched Reluctance Motor

Susitra Dhanarajalu

Abstract

This chapter aims in presenting the methods for the accurate estimation of highly non linear phase inductance profile of a switched reluctance motor (SRM). The magnetization characteristics of a test SRM is derived from the SRDaS (Switched Reluctance Design and Simulation) simulation software. Statistical interpolation based regression analysis and Artificial Intelligence (AI) techniques are used for developing the computationally efficient inductance model. Multi Variate Non linear Regression (MVNLR) from the class of regression analysis and Adaptive Neuro Fuzzy Inference System (ANFIS) under the class of AI are implemented and tested on the simulated data. Non linear Inductance profile $L(I, \theta)$ of SRM is successfully estimated for the complete working range of phase currents (I_{ph}). At each I_{ph} , $L(I, \theta)$ values are estimated and presented for one cycle of rotor position (θ). Estimated inductance profile based on the two proposed methods is observed to be in excellent correlation with the true value of data.

Keywords: SRM, electromagnetic profile, multivariate non-linear regression, ANFIS

1. Introduction

Over past two decades, there has been noticeable increase in the research publications on switched reluctance machine (SRM). The machine can be operated as both generator and motor by suitable control techniques. It has been proved from research publications that SRM is a valid alternative to conventional machines in almost all industrial applications. The characteristics of electromagnetic parameters are highly non-linear due to the following reasons; i) highly saturated working zone ii) eddy current and hysteresis current effects iii) double salient structure and iv) non uniform air gap. All these effects makes the machine's flux linkage and torque as the non-linear function of phase current (I_{ph}) and rotor position(θ). Flux linkage of the machine depends on its phase inductance. For the analysis and control of the machine, it is important to establish the accurate nonlinear mapping between its phase inductance, phase current and rotor position. The design and electrical analysis of the machine is greatly dependent on its electromagnetic behavior. Linear mathematical models are proposed by many publications that are not applicable for real time control. Non-linear models are developed by few researchers based on the following techniques; a) Analytical model [1–10] in which Fourier series based

expressions are derived. This method is highly time consuming and not suitable for real time control applications. b) magnetic model [11] c) finite element model (FEM) [11, 12] provides accurate results whereas it involves complicated mathematics computation. d) Artificial neural network models [13–21].

All these models have either fine precision or good computation speed. Both the benefits are not satisfied in any of these models. Few of the recent research publications have reported using the Adaptive Neuro fuzzy inference system (ANFIS) techniques for the computation of magnetic parameters [22–24] and estimation of rotor position [25]. On the overview of the publications on modeling of SRM, it is observed that none of the papers have paid attention in using Multivariate nonlinear regression technique (MVNLRT) for estimating its nonlinear inductance model. In this chapter, non-linear inductance model of SRM is developed based on the MVNLRT and ANFIS. Also the comparison between the results of ANFIS and MVNLRT inductance models are presented. This chapter is organized as follows; Section II discusses the mathematical model of SRM and the necessity of inductance modeling. The nonlinear inductance model based on MVNLRT and the one based on ANFIS are presented in section III and IV respectively. The comparative analysis of both the models is presented in section V and the inferential remarks are given in section VI.

2. Mathematical model of SRG and the necessity of inductance modeling

SRM is a singly excited and doubly salient machine shown in **Figure 1**. The number of phases wound on the stator poles differs from machine to machine. There is certain number of suitable combinations of stator and rotor poles thus giving many machine configurations. The phase windings are excited sequentially for rotating the rotor in desired direction. For efficient control, the phase windings are excited with the current pulses based on the rotor position.

The electromagnetic characteristics of the machine vary depending on the relative rotor position with respect to stator pole axis and magnitude of current in the excited phase winding. An ideal machine is one with equal stator and rotor pole axis and saturation of the core and leakage fluxes are neglected. In such a ideal machine,

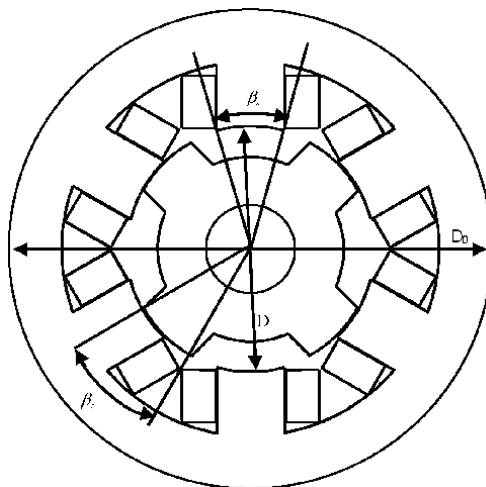


Figure 1.
Three phase 6/4 pole SRM configuration.

the variation of phase inductance is triangular in shape. However, in a practical machine, the variation is highly nonlinear. When the stator and rotor poles are coincident (aligned position), the inductance is maximum and minimum inductance is experienced when the rotor inter polar axis coincides with the excited stator pole axis (unaligned position). The position of rotor between these two positions is called intermediate positions. Upon exciting a particular stator phase, its nearest pair of rotor poles tends to move towards the path of minimum reluctance along the excited stator poles by developing a required torque. The magnitude of torque developed depends on the magnitude of the excited current and rate of change of inductance with rotor position. Accurate rotor position sensors, power converter and a controller with good control technique are required for the successful operation and precise control of SRM [26].

Owing to the high non-linearity of the machine, a mathematical model describing the behavior of the machine is required. This model can be used as a base for simulation and verification of static and dynamic characteristics of SRM.

2.1 Energy balance equation

The conversion of electrical energy to mechanical energy and vice versa by an electromechanical energy converter is illustrated by the energy-balance scheme shown in **Figure 2**.

A magnetic system couples the electrical and mechanical systems. The electromechanical energy converter illustrates the relationship between the electrical energy, mechanical energy, energy losses, energy stored and energies transferred between the electrical and mechanical systems. From **Figure 2**, and making an assumption that $W_{iron} = 0$ and $W_{leak} = 0$, the following equations are developed.

$$W_{ea} = W_{ei} - W_{cu} - W_{leak} \quad (1)$$

$$W_{emec} = W_{ea} - W_{field} - W_{iron} \quad (2)$$

$$W_{mech} = W_{emec} - W_{fri} - W_{iner} \quad (3)$$

$$\text{Energy input} = W_{ea} \quad (4)$$

$$\text{Energy losses} = W_{cu} + W_{iron} + W_{fri} \quad (5)$$

$$\text{Energy stored in the system} = W_{leak} + W_{field} + W_{iner} \quad (6)$$

$$\text{Energy output} = W_{mech} \quad (7)$$

Thus Energy output = Energy input - Energy losses - Energy stored.

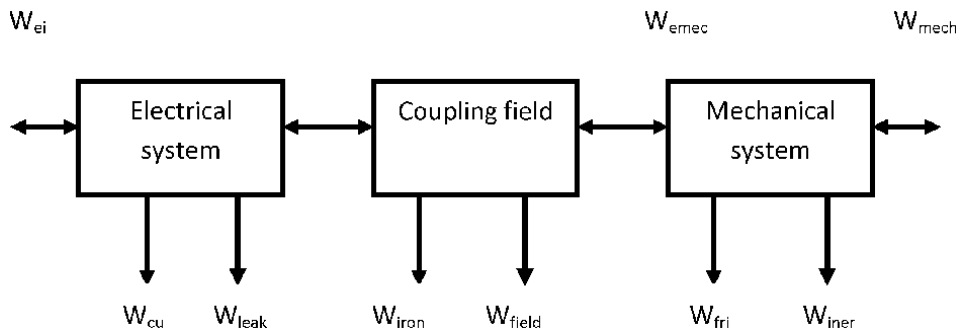


Figure 2.
 Electromechanical energy conversion model.

In an ideal system, if the energy losses are neglected, the output energy is equal to the energy input into the system minus energy stored in the various components of the system. However, the stored energies can be recovered through regenerative process.

2.2 Equation of phase voltage

Electromagnetic characteristics of a 6/4 pole SRM is shown in **Figure 3**. The illustration shows the mapping among the flux linkage (ψ), current (i) in excited phase and rotor position (θ) of SRM. The high non-linearity behavior of the machine is clearly visible from the figure. The curve is linear for small values of excitation current. As the rotor rotates from unaligned to aligned position, the mapping among the motor parameters becomes highly nonlinear.

Figure 4 shows the equivalent circuit of an excited phase of the motor.

According to **Figure 4**, the instantaneous voltage across the terminals of a phase of SRM winding related to the flux linked in the winding is given by,

$$V_{ph}(t) = i_{ph}(t)r_{ph} + \frac{d\psi_{ph}(i_{ph},\theta_{ph})}{dt} \quad (8)$$

$$\psi_{ph} = \int (V_{ph} - i_{ph}r_{ph})dt \quad (9)$$

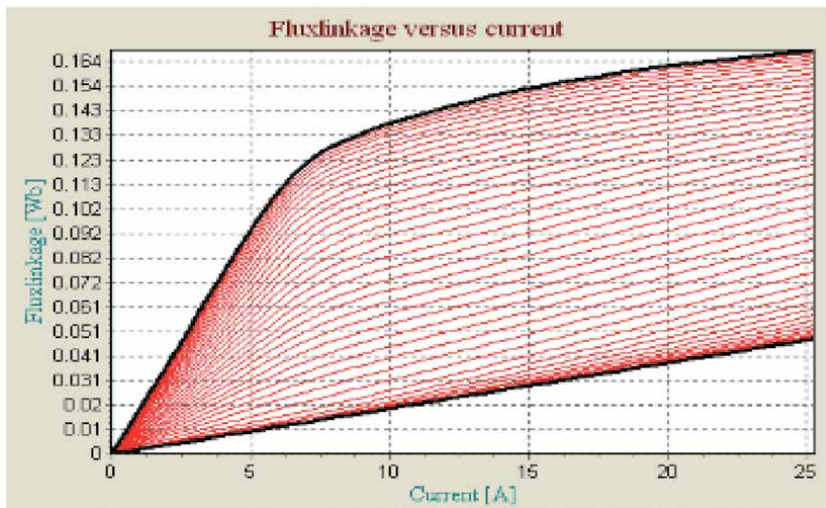


Figure 3. Magnetization characteristics of three phase 6/4 pole SRM.

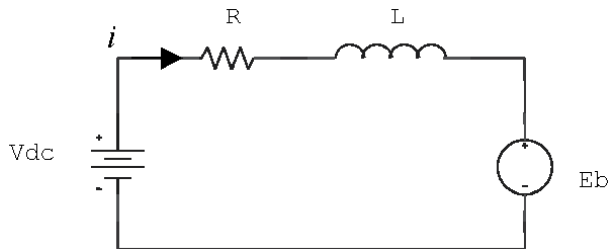


Figure 4. Electrical equivalent circuit of the SRM.

Due to the double salient structure and effect of magnetic saturation, the flux linkage (ψ_{ph}) and inductance of excited motor phase winding varies as a function of both rotor position (θ_{ph}) and phase current (i_{ph}). Therefore (8) is written as given in (10).

$$V_{ph} = i_{ph}r_{ph} + \frac{d[L_{ph}(i_{ph}, \theta), i_{ph}]}{dt} \quad (10)$$

$$V_{ph} = i_{ph}r_{ph} + L_{ph} \frac{di_{ph}}{dt} + i_{ph} \frac{\partial L_{ph}}{\partial \theta} \frac{d\theta}{dt} \quad (11)$$

$$V_{ph} = i_{ph}r_{ph} + \left[L_{ph} \frac{di_{ph}}{dt} + \frac{1}{2} i_{ph} \frac{dL_{ph}}{d\theta} \omega \right] + \frac{1}{2} i_{ph} \omega \frac{dL_{ph}}{d\theta} \quad (12)$$

2.3 Torque equation

When a phase of the SRM is excited by a voltage source, the instantaneous power is obtained by multiplying (12) by i_{ph} .

$$P = V_{ph}i_{ph} = i_{ph}^2 r_{ph} + i_{ph}L_{ph} \frac{di_{ph}}{dt} + \omega i_{ph}^2 \frac{dL_{ph}}{d\theta} \quad (13)$$

$$V_{ph}i_{ph} = i_{ph}^2 r_{ph} + \frac{d}{dt} \left(\frac{1}{2} L_{ph} i_{ph}^2 \right) + \frac{1}{2} \omega i_{ph}^2 \frac{dL_{ph}}{d\theta} \quad (14)$$

$$V_{ph}i_{ph} = i_{ph}^2 r_{ph} + \frac{dw_f}{dt} + T_m \omega \quad (15)$$

where

$$W_f = \frac{1}{2} L_{ph} i_{ph}^2 \quad (16)$$

is the energy stored in the magnetic field.
and

$$T_m = \frac{1}{2} i_{ph}^2 \frac{dL_{ph}}{d\theta} \quad (17)$$

is the expression for instantaneous torque produced in the energized phase winding. In (15), The instantaneous electrical power supplied to the motor is given on the left hand side of the equation. On the right hand side of equation, the first term represents the power loss due to phase resistance, the derivative of stored energy in the magnetic field is represented in the second term and the mechanical power developed by the motor is represented in the third term.

The stator and rotor pole arc combinations are equal in SRM. The machine has triangular shaped inductance characteristics. The inductance value is maximum at aligned position and minimum at unaligned position. For a 6/4 pole SRM, an inductance profile for unequal stator and rotor pole arc combinations are shown in **Figure 5**. From the Eq. (17), it is clear that SRM develops positive torque when the phase is excited during the period of rising inductance, when $\frac{dL}{d\theta} > 0$. Negative torque is developed when the phase is excited during the period of the falling inductance, when $\frac{dL}{d\theta} < 0$ and torque developed is zero when the phase is excited during the period of constant inductance, when $\frac{dL}{d\theta} = 0$. The machine can transform reversible modes of motoring and generating operations by suitable control of the switches in power converter. From this, it is understood that the operating mode of

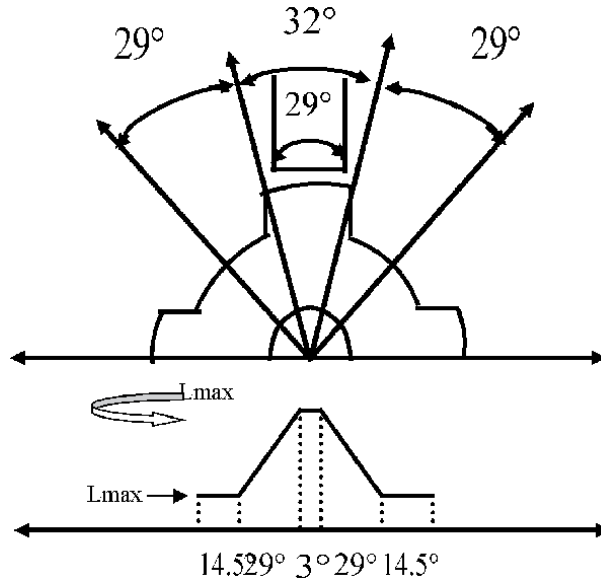


Figure 5.
Variation of inductance for one rotor pole pitch.

the machine greatly depends on its phase inductance value. Therefore inductance needs to be modeled accurately for real time applications.

The torque developed can be normally expressed in terms of the change of coenergy with respect to rotor position. The $\Psi - i$ characteristics of the SRM for a given rotor position is shown in **Figure 6**. These characteristics can either be obtained by conducting an experiment on the SRM or by performing magnetic field analysis. The area representing stored field energy (W_f) and co-energy (W_c) are marked in **Figure 6(a)** for a given phase current. The area below the $\psi - i$, characteristics can be written as.

$$W_c = \int_0^i \psi di \quad (18)$$

Consider the movement of the rotor through an infinitesimal displacement $\Delta\theta$ when the current is held constant. The $\psi - i$ characteristics of SRM for the given rotor position is shown in **Figure 6(b)**. During the movement of the rotor, a definite amount of mechanical work is done by the motor. The electrical energy (ΔW_e) fed to the motor is partially used to produce mechanical motion (ΔW_m) and a part of the energy gets stored in the magnetic field (ΔW_f). From **Figure 6(b)**, the change in electrical energy input is,

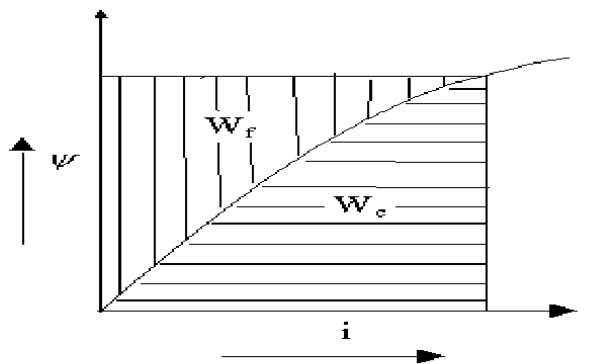
$$\Delta W_e = \text{area WXYZ} \quad (19)$$

and the change in stored field energy is

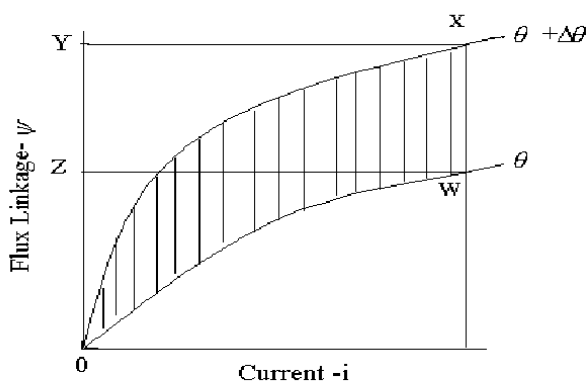
$$\Delta W_f = \text{area OXY} - \text{area OWZ} \quad (20)$$

and the mechanical work done is,

$$\begin{aligned} \Delta W_m &= \Delta W_e - \Delta W_f = T\Delta\theta = \text{Area WXYZ} - (\text{area OXY} - \text{area OWZ}) \\ &= \text{Area WXYZ} - \text{area OXY} - \text{area OWZ} = \text{Area OWX} \end{aligned} \quad (21)$$



(a)



(b)

Figure 6. Magnetic characteristics of SRM. (a) Electromechanical energy conversion. (b) $\psi - i$ characteristics for a given rotor position.

The area OWX represents the change in the co-energy (ΔW_c) and the torque can be calculated as.

$$T = \frac{\Delta W_c}{\Delta \theta} \quad (22)$$

It can be observed that only a part of the energy input into the motor is utilized for torque production. If the $\psi - i$ characteristics were highly non-linear in the aligned position and linear in the unaligned position, then, the magnitude of the torque developed would be higher compared with the situation when the $\psi - i$ characteristics are linear for both the positions.

3. Inductance modeling of SRM using multivariate nonlinear regression technique

Regression analysis uses many techniques for modeling and analyzing parameters. It is useful in accurate mapping of dependent and independent variables even under unknown physical process. In non-linear regression model, the observed data

are expressed as a nonlinear function of parameters and proved to be more accurate even for extrapolated data range. A nonlinear model is expressed as given in (23).

$$y = f(X, \beta) + \varepsilon \quad (23)$$

where

- y - Vector of the observed response variables ($n \times 1$).
- X - matrix determined by the predictor variables ($n \times p$).
- β - vector of unknown parameters to be estimated ($p \times 1$).
- f - function of X and β .
- ε - vector of independent, identically distributed random disturbances ($n \times 1$).

Multivariate analysis encompasses the observation and analysis of more than one outcome variable and gives an excellent solution for nonlinear problems. This approach executes well in high dimensional problems especially when the available data set is of very small size. In this section MVNLR model is used for estimating the inductance parameters. Coefficients of predictor variables are estimated using least square method. The inductance values between an unaligned and aligned position from the magnetization characteristics of [27] has been used in exploring the non-linear relationships between the phase inductance $L(i, \theta)$, phase current (I) and rotor position (θ) and is expressed in terms of least square polynomial approximation of third order and the MVNLR based inductance model of the three phase, 6/4 SRG is expressed by the Eq. (24).

$$\begin{aligned} \begin{bmatrix} L_1 \\ L_2 \\ L_3 \end{bmatrix} &= \begin{bmatrix} 2.605 \times 10^{-6} & -9.645 \times 10^{-5} & 9.933 \times 10^{-4} \\ 2.631 \times 10^{-6} & -9.741 \times 10^{-5} & 10.032 \times 10^{-4} \\ 2.579 \times 10^{-6} & -9.549 \times 10^{-5} & 9.834 \times 10^{-4} \end{bmatrix} \begin{bmatrix} I^3 \\ I^2 \\ I \end{bmatrix} + \\ &\begin{bmatrix} -5.518 \times 10^{-8} & 1.914 \times 10^{-7} & 3.752 \times 10^{-4} \\ -5.573 \times 10^{-8} & 1.933 \times 10^{-7} & 3.79 \times 10^{-4} \\ -5.463 \times 10^{-8} & 1.894 \times 10^{-7} & 3.714 \times 10^{-4} \end{bmatrix} \begin{bmatrix} \theta^3 \\ \theta^2 \\ \theta \end{bmatrix} + \\ &\begin{bmatrix} -5.825 \times 10^{-7} & 1.881 \times 10^{-7} - 2.745 \times 10^{-6} \\ -5.883 \times 10^{-7} & 1.91 \times 10^{-7} - 2.772 \times 10^{-6} \\ -5.767 \times 10^{-7} & 1.862 \times 10^{-7} - 2.718 \times 10^{-6} \end{bmatrix} \begin{bmatrix} I^2\theta \\ I\theta^2 \\ I\theta \end{bmatrix} + \\ &\begin{bmatrix} -1.095 \times 10^{-3} \\ -1.106 \times 10^{-3} \\ -1.084 \times 10^{-3} \end{bmatrix} \end{aligned} \quad (24)$$

Actual inductance Vs MVNLR inductance

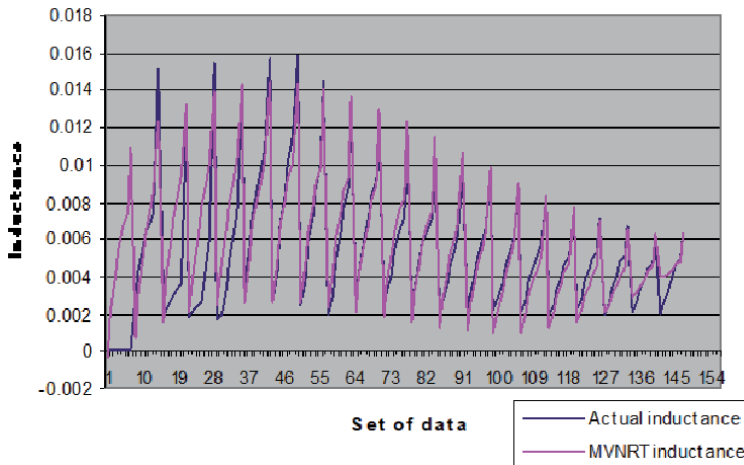


Figure 7.
 True data set vs MVNLR predicted data.

Comparison of true values Vs MVNLR estimated values is shown in **Figure 7**. From the analysis, it is clearly evident that the MVNLR predicted inductance values shows a strong agreement with the true data values used for developing the model.

4. Inductance modeling of SRG using adaptive neuro -fuzzy inference system

The ANFIS is an adaptive neuro - fuzzy inference system (Jyh-Shing et al., 1993) [28]. The fuzzy inference system (FIS) has been developed for the inductance estimation of SR machine. FIS has two inputs and single output. Phase current (I_{ph}) and rotor position (θ) are the input variables and phase inductance, $L(I,\theta)$ is the output variable. The input variables are fuzzified using 12 triangular membership functions. Fuzzy rule base has $12*12$ (144) if-then rules. The ANFIS architecture is shown in **Figure 8**. There are 5 layers in the ANFIS network.

Layer 1: Both the inputs are fuzzified with 12 triangular membership functions. The output of input membership function 1 is $O_{k1} = \mu A_k(i)$ and the output of input membership function 2 is, $O_{k2} = \mu B_k(\theta)$, i and θ are the input to nodes 1 and 2, respectively. A_k and B_k are the linguistic labels (mf1, mf2 ... mf12.) associated with the node functions.

The output of the input membership functions specifies the degree to which the given i and θ satisfies the quantifier A_k and B_k . Triangular shaped membership functions $\mu A_k(i)$ and $\mu B_k(\theta)$ are used with a maximum equal to 1 and a minimum equal to 0. The generalized triangular membership function of the current is given by

$$\mu A_k(i) = \begin{cases} 0 & i \leq a_k \\ \frac{i - a_k}{b_k - a_k} & a_k \leq i \leq b_k \\ \frac{c_k - i}{c_k - b_k} & b_k \leq i \leq c_k \\ 0 & c_k \leq i \end{cases} \quad (25)$$

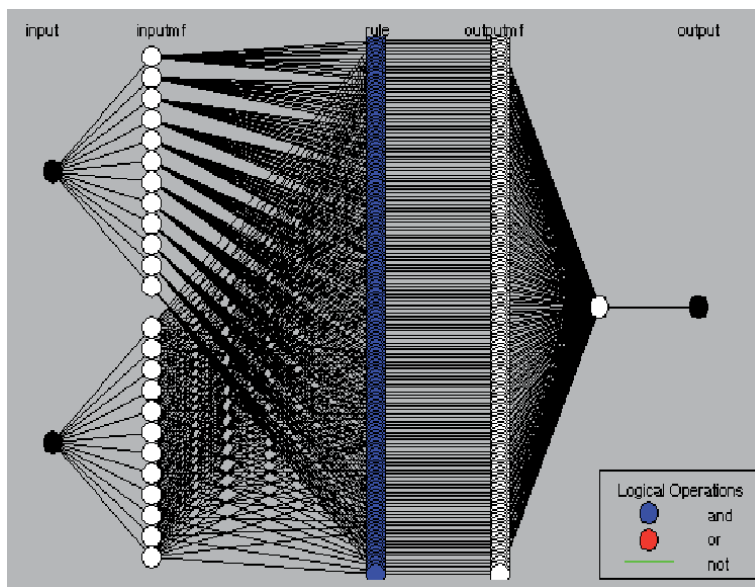


Figure 8.
ANFIS network structure.

Similarly, the generalized triangular shaped membership function of the rotor position is given by

$$\mu B_k(\theta) = \begin{cases} 0 & \theta \leq a_k \\ \frac{\theta - a_k}{b_k - a_k} & a_k \leq \theta \leq b_k \\ \frac{c_k - \theta}{c_k - b_k} & b_k \leq \theta \leq c_k \\ 0 & c_k \leq \theta \end{cases} \quad (26)$$

where a_k , b_k and c_k are the adaptable variables. The triangular shaped functions varies with the change in the parameter values.

Layer 2: Fuzzy AND operator is implemented in this layer.

$$W_k = \mu A_k(i) \times \mu B_k(\theta) \quad (27)$$

where $k = 1, 2 \dots 12$;

Layer 3: Scaling or normalizing of firing strengths takes place in this layer.

$$\bar{W}_k = O_{k4} = \bar{W}_k f_k = \bar{W}_k (m_k + n_k \theta + r_k) \quad (28)$$

Layer 4: The output of the fourth layer comprises a linear combination of the inputs multiplied by the normalized firing strength. Output of this layer is given by.

$$O_{k4} = \bar{W}_k f_k = \bar{W}_k (m_k i + n_k \theta + r_k) \quad (29)$$

Output of layer 3 is \bar{W}_k . The modifiable variables m_k , n_k and r_k are known as consequent parameters.

Layer 5: This layer is a simple summation of the outputs in the previous layer. The phase inductance $L(i,\theta)$ is obtained from the overall output.

$$O_{k5} = \sum \overline{W}_k f_k = \frac{\sum_k W_k f_k}{\sum_k W_k} \quad (30)$$

The magnetic parameter values are considered during the period of unaligned to aligned rotor position for developing the inductance model. The range of the current and rotor position during this period are $0 \leq I \leq 25$ A and $0 \leq \theta \leq 45$ deg.

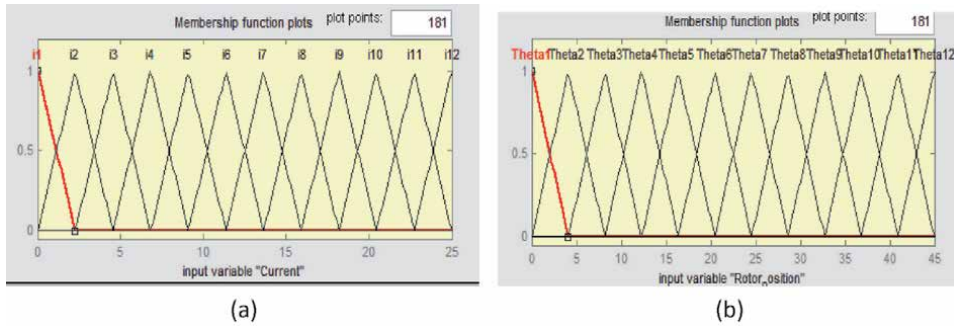


Figure 9. Fuzzy triangular membership functions for the input parameters. (a) Phase current. (b) Rotor position.

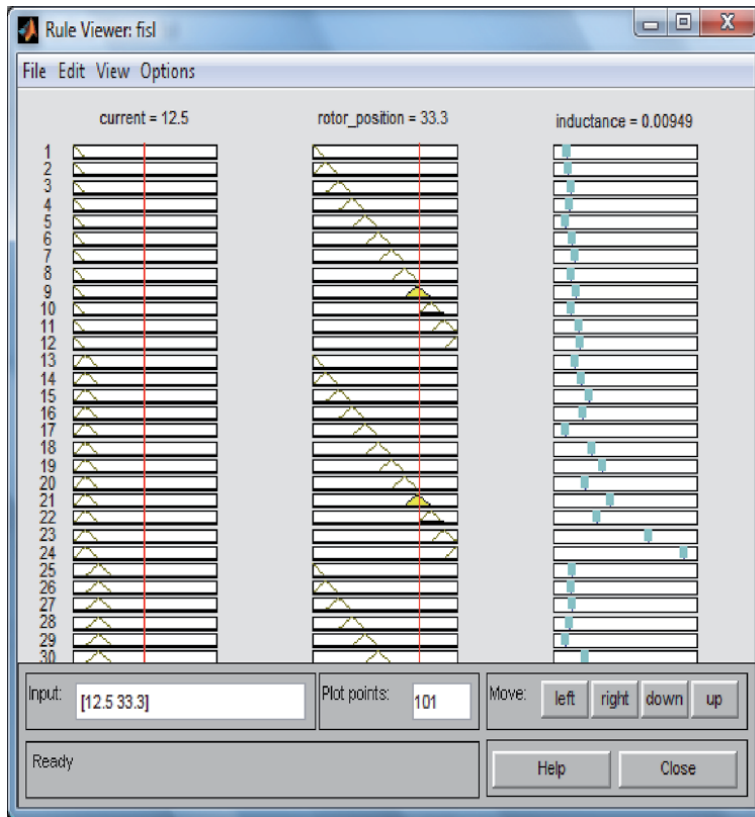


Figure 10. Rule viewer - ANFIS.

The ANFIS information are as follows.

Total number of parameters: 504; Number of nonlinear parameters: 72

Number of linear parameters: 432; Number of fuzzy rules: 144

Number of training data pairs: 182; Number of checking data pairs: 0

Number of nodes: 341.

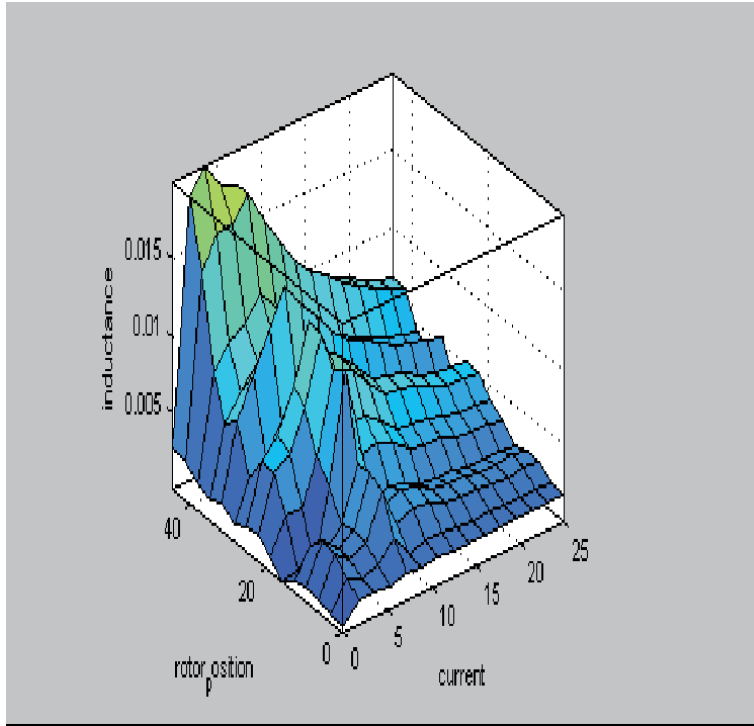


Figure 11.
Mapping surface of $L(i, \theta)$.

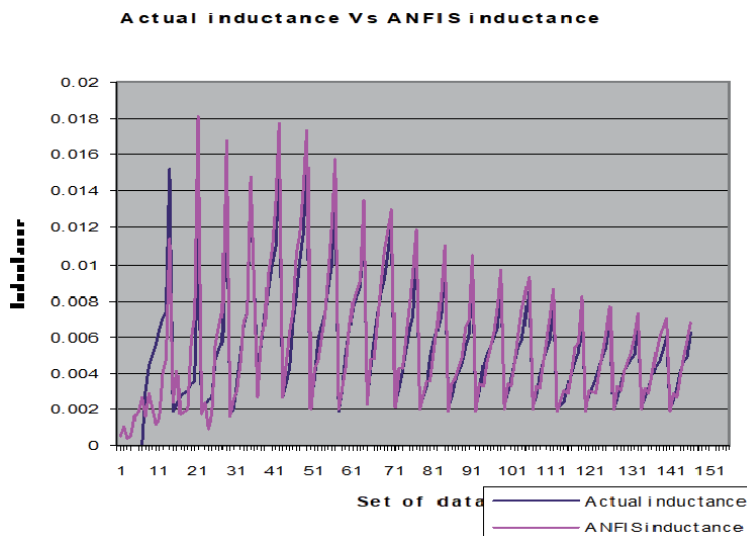


Figure 12.
True data vs ANFIS predicted data.

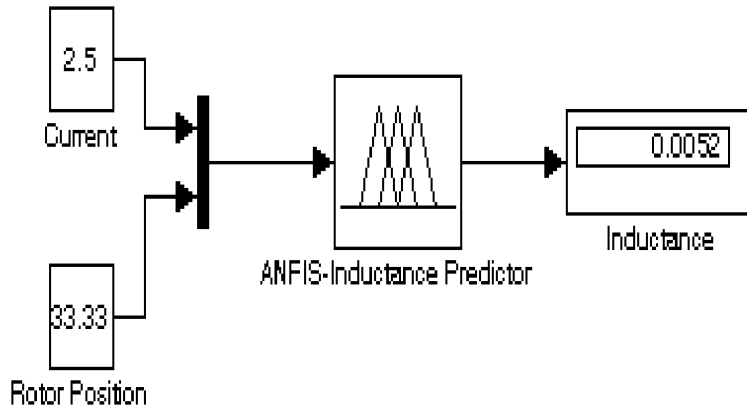


Figure 13.
 ANFIS inductance predictor from Simulink.

The triangular membership functions for the two inputs: current and rotor position are given in **Figure 9(a)** and **(b)** respectively.

The 144 rules framed in ANFIS is shown in **Figure 10**. The fuzzy inference process is interpreted from this rule viewer. The ANFIS surface mapping between input and output parameters is depicted in **Figure 11**. For low values of current, the variation in inductance is observed to be linear. After saturation, the variation is highly non linear. **Figure 12** shows the comparison of the original test data with the ANFIS predicted data. From this comparison, it is clear that the inductance estimation from ANFIS is in very good concurrence with the test values of inductance. **Figure 13** shows the MATLAB simulink model of ANFIS inductance predictor.

5. Comparison of MVNLRT and ANFIS based inductance models

Both the proposed inductance models based on MVNLRT and ANFIS uses the data from the magnetization characteristics of the machine. **Figure 14** shows the

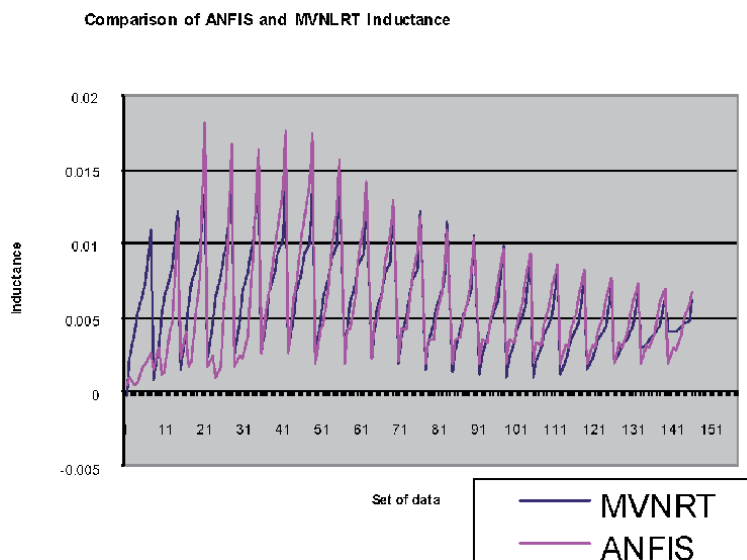


Figure 14.
 MVNLRT vs ANFIS models.

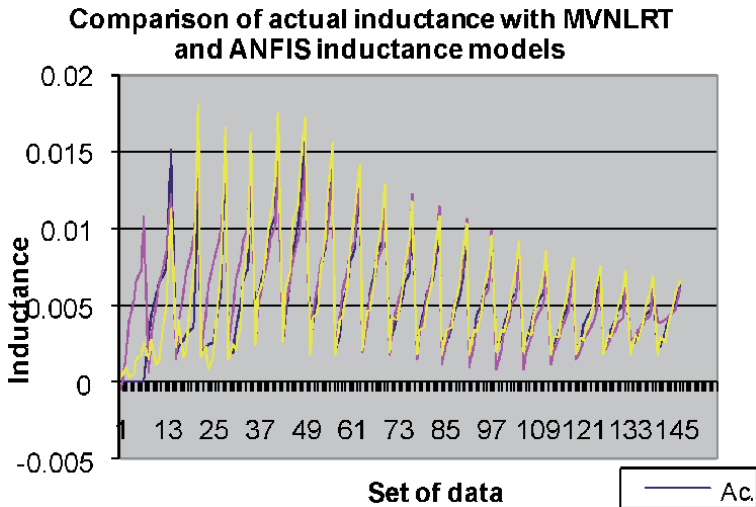


Figure 15. True vs MVNLR vs ANFIS data.

comparison chart of the inductance values obtained from the ANFIS and MVNLRT models and **Figure 15** illustrates the comparison of these two models along with the actual inductance values. For both the methods, the predicted and true values are compared at various phase current values and the same is shown in **Figure 16**. Root-mean-squared error (RMSE), Mean Absolute Error (MAE) and Maximum Absolute value Error (MAVE) for both the methods at different currents are given in **Table 1**. The RMSE for ANFIS and MVNLRT for full range of currents is shown in **Figure 17**. From the careful observation of comparison charts and error values, it is inferred

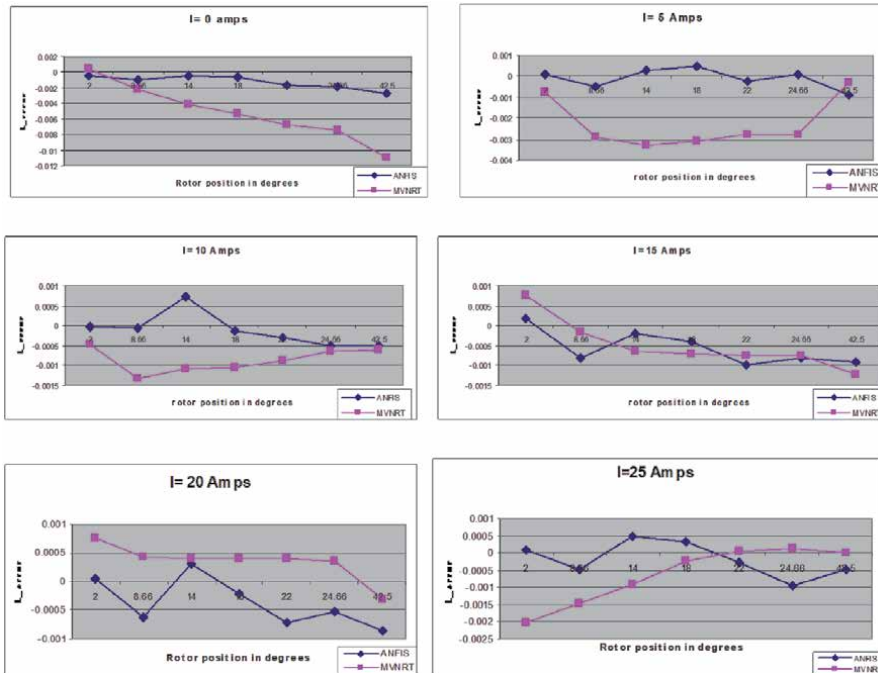


Figure 16. MVNLR VS ANFIS at various currents.

Current in amps	For θ varying from 0 to 45 degrees at each phase current					
	ANFIS Estimator(Error in Henry)			MVNRT Estimator(Error in Henry)		
	$L_{abs\ max}$	$L_{abs\ mean}$	L_{RMSE}	$L_{abs\ max}$	$L_{abs\ mean}$	L_{RMSE}
0	2.7E-03	3E-04	8E-04	1.1E-02	1.6E-03	4E-03
5	9E-04	6.5E-05	1.7E-04	3.3E-03	1.4E-04	3.6E-04
10	7.1E-04	1.6E-05	4.2E-05	1.3E-03	6.6E-05	1.7E-04
15	9.7E-04	1.6E-04	4.2E-04	1.2E-03	2.9E-04	7.6E-04
20	8.5E-04	1.3E-04	3.4E-04	7.5E-04	1.5E-04	4E-04
25	9.3E-04	8.1E-05	2.2E-04	2E-03	2.9E-04	7.7E-04

Table 1.
 RMSE, MAE and MAVE at different currents and rotor position.

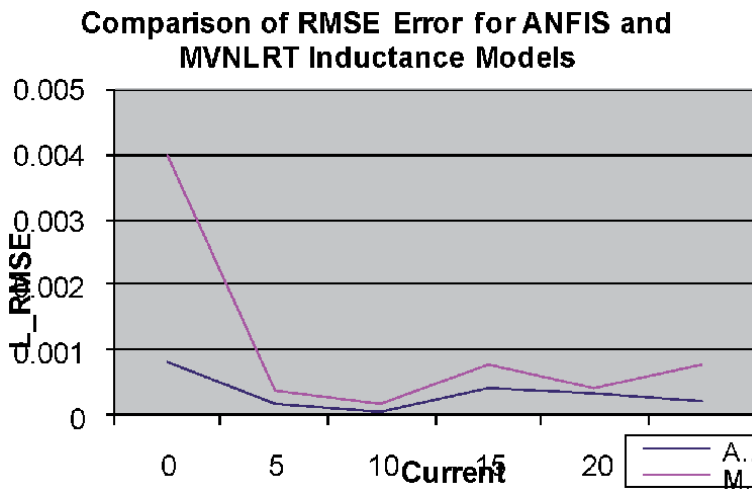


Figure 17.
 L_{RMSE} - ANFIS vs MVNLR.

that both ANFIS and MVNLR models produce accurate mapping between input and output parameters. Among these two methods, ANFIS model has proved to have developed the model with higher precision and with least errors.

6. Conclusion

This paper has presented two methods of computationally efficient modeling techniques for a 3 phase, 6/4 switched reluctance generator for obtaining the nonlinear inductance model by means of adaptive neuro fuzzy inference system and Multivariate nonlinear regression technique. The developed inductance profile based on both these methods is trained with the same set of true data. Both the estimated models depict the nonlinear relation between phase winding inductance at various operating currents and at various rotor positions at each current. MVNLR predicted model is in good concurrence with the true model. The ANFIS model shows an excellent concurrence with true data and reports only an insignificant error throughout the data range. From the observations and analysis of results

obtained, it is inferred that both the techniques are proficient in estimation of SRM inductance parameter within acceptable accuracy limits. The methods are highly certain in presenting a superior performance when applied to modeling, prediction and control. Both are very simple, easy to implement and are sure to replace any computationally intensive numerical model of SRM. Of the two methods proposed in this chapter, ANFIS has high computational speed, simple structure, least training least epoch, faster learning, good convergence and presents a superior performance. The computational accuracy and easiness of estimation validate that ANFIS is highly competent tool for real time control of SR machine.

Author details

Susitra Dhanarajulu

Department of Electrical and Electronics Engineering, Sathyabama Institute of Science and Technology, Chennai, Tamilnadu, India

*Address all correspondence to: susitradhanraj@gmail.com

IntechOpen

© 2021 The Author(s). Licensee IntechOpen. This chapter is distributed under the terms of the Creative Commons Attribution License (<http://creativecommons.org/licenses/by/3.0>), which permits unrestricted use, distribution, and reproduction in any medium, provided the original work is properly cited. 

References

- [1] Osamu Ichinokura, Tsukasa Kikuchi, Kanji Hackamore, Tadakki Watanabe and Hai-Jiao Guo, Dynamic simulation model of switched reluctance generator, *IEEE trans. Magnetics*, Vol. 39, No. 5, pp. 3253–3255, September 2003.
- [2] Loop, B. Essah, D. N. Sudhoff, S., A basis function approach to the nonlinear average value modelling of switched reluctance machines, *IEEE Transaction on energy conversion*, 2006, VOL 21; no 1, pages 60–68.
- [3] Radimov. N, Ben-Hail, N and Rabinovici. R, A Simple Model of Switched-Reluctance Machine Based Only on Aligned and Unaligned Position Data, *IEEE IEEE Transactions on Magnetics*, 2004, vol. 40, issue 3, pp. 1562–1572.
- [4] Loop. B.P, Sudhoff. S.D, Switched reluctance machine model using inverse inductance charecterization, *IEEE Transaction on industry applications*, June 2003, Vol.39, issue.3, pp.743–751.
- [5] Hongwei Gao, Farzad Rajaei salmasi and Ehsani Mehrdad, Inductance model-based sensorless control of the switched reluctance motor drive at low speed, *IEEE transactions on power electronics*, 2004, vol. 19, no 6, pp. 1568–1573.
- [6] Edrington, C.S. Fahimi, and B. Krishnamurthy. M, An autocalibrating inductance model for Switched reluctance motor drives, *IEEE Transaction on Industrial Electronics*, 2007, vol.54, pp.2165–2173.
- [7] Abelardo Martinez, Eduardo Laloya, Javier Vicuna, Francisco perez, Tomas Pollan, Bonifacio Martin, Beatriz Sanchez and Juan Llado, Simulation model of an AC autonomous Switched reluctance generator, EUROCON 2007 - The International Conference on Computer as a Tool (EUROCON 2007), vol.2
- [8] wen ding, deliang Liang, Fourier series and ANFIS based modelling and prediction for switched reluctance motor, International conference on electrical machines and systems, ICEMS 2008.
- [9] Hujjan Zhou, Wen Ding and Zhenmin Yu, A nonlinear model for the Switched reluctance motor, *Proc. of the 8th International conference on Electrical machines and systems*, ICEMS sep 2005, vol.1, pp.568–571.
- [10] Hoang Le-Huy and Patrice Brunelle, A versatile Nonlinear Switched reluctance Motor model in simulink using realistic and analytical magnetization characteristics.
- [11] Vladan Vujcic and Slobodan.N, A simple nonlinear model of the switched reluctance motor, *IEEE Transaction on energy conversion*, Dec 2000, vol.15, No.4.
- [12] Shoujan Song and Weiguo Liu, A novel method for nonlinear modeling and dynamic simulation of a four -phase switched reluctance generator system based on MATLAB SIMULINK, in *Proc. 2007 Second IEEE conference on Industrial Electronics and Applications*, pp. 1509–1514.
- [13] Ustun. O, Measurement and Real-Time Modeling of Inductance and Flux Linkage in Switched Reluctance Motors, *IEEE Transactions on Magnetics*, vol. 45, issue 12, pp. 5376–5382.
- [14] Wenzhe Lu, Ali Keyhani and Abbas Fardoun, Neural network based modelling and parameter identification of switched reluctance motors, *IEEE Transaction on energy conversion*, june 2003, vol.18, no.2
- [15] Zhengyu Lin, Doanld S. Reay, barry. W.Williams and Xiangning He, Online modelling for switched reluctance

- motors, IEEE Transactions on Industrial electronics, dec 2007, vol.54, no.6.
- [16] Xiao Wen-Ping and Ye Jia-wei, Improved PSO-BPNN algorithm for SRG modelling, International Conference on Industrial Mechatronics and Automation, 2009. ICIMA 2009. Volume, Issue, 15–16 May 2009 Page(s): 245–248.
- [17] Vejjan. R, Gobbi. R and Sahoo. N.C, Polynomial neural network based modeling of Switched reluctance motors, Power and energy society general meeting-Conversion and delivery of electrical energy in 21st century, July 2008, pp.1–4.
- [18] Elmas.C, sagiroglu.S, colak.I and Bal.G, Modeling of non-linear switched reluctance drive based on artificial neural networks, 5th international conference on Power electronics and variable speed drives, Oct 1994, pp.7–12.
- [19] Yan cai and Chao Gao, Non-linear modelling of switched reluctance drive based on BP neural networks, *Proc. of the 3rd International Conference on Natural Computation*, 2007, vol.01, pp.232–236.
- [20] Oguz Ustun, A nonlinear full model for switched reluctance motor with artificial neural networks, *Energy Conversion and Management*, Sep 2009, vol.50, pp.2413–2421.
- [21] Hexu Sun, yanqing Mi, Yan Dang, Yi Zheng and Yanzong Dong, The nonlinear modelling of switched reluctance motor with improved RBF network, second international conference on Intelligent networks and Intelligent systems, 2009.
- [22] Wen Ding Deliang Liang, Modeling of a 6/4 Switched Reluctance Motor using adaptive neural fuzzy inference system, *IEEE Transactions on Magnetics*, July 2008, vol.44, issue:7, pp-1796-1804.
- [23] Ferhat Daldaban, Nurettin Ustkoyuncu and Kerim Guney, Phase inductance estimation for switched reluctance motor using adaptive neuro-fuzzy inference system, July 2005, Science Direct.
- [24] Susitra, D., Paramasivam S. (2014), “Estimation of phase inductance profile in a three-phase 6/4 pole switched reluctance,” *International Journal of Power Electronics*, vol.6, no.3, pp. 257–274.
- [25] Susitra, D. and S. Paramasivam, “Artificial intelligence-based rotor position estimation for a 6/4 pole switched reluctance machine from phase inductance,” *International Journal of modelling, identification and control*, 22(1), pp. 68–79.
- [26] R.Krishnan. *Switched reluctance motor drives. Modeling, Simulation, Analysis, Design and Applications* Boca Raton FL: CRC. 2001.
- [27] Switched reluctance motor Design and Simulation software by Peter Omand Rasmussen.
- [28] J.S.R. Jang, ANFIS: Adaptive-Network-Based Fuzzy Inference System, *IEEE Trans. Systems, Man, Cybernetics*, 23(5/6):665–685, 1993.

*Edited by Ahmed F. Zobaa
and Shady H.E. Abdel Aleem*

This book is an introduction to the concepts and developments of emerging electric machines, including advances, perspectives, and selected applications. It is a helpful tool for practicing engineers concerned with emerging electric machines and their challenges and potential uses. Chapters cover such topics as electric machines with axial magnetic flux, asynchronous machines with dual power supply, new designs for electrical machines, and more.

Published in London, UK

© 2021 IntechOpen
© jef harris / iStock

IntechOpen

